Université de Lille

iemn
Institut d'Electronique, de Microélectronique et de Nanotechnologie
UMR CNRS 8520

Université de Lille, ED ENGSYS Ecole doctoral Sciences de l'Ingénierie et des Systèmes
IEMN Institut d'électronique de microélectronique et de nanotechnologie

Thèse soutenue par Kamila JANZAKOVA
Le 11 Mai, 2023
Pour obtenir le grade de Docteur de l'université de Lille
Spécialité Électronique, microélectronique, nanoélectronique et micro-ondes

Développement de dendrites polymères organiques en 3D comme dispositif neuromorphique

Development of 3D organic polymer dendrites as neuromorphic device

Composition du jury:

Rapporteur	Yoeri van de Burgt	Associate Professor. Université de technologie d'Eindhoven
Rapporteur	Mamatimin Abbas	Chargé de recherche, HdR. CNRS, IMS, l'Université de Bordeaux
Examinatrice	Jennifer Gerasimov	Ingénieur chercheur principal. Linköping University
Président du jury	Vincent Thomy	Professeur. Université de Lille
Examinateur	Stéphane Lenfant	Directeur de recherche,HdR. IEMN, CNRS
Directeur de thèse	Yannick Coffinier	Directeur de recherche,HdR. IEMN, CNRS, Université de Lille
Co-directeur de these (invite)	Fabien Alibart	Chargé de recherche, HdR. IEMN, CNRS, Université de Lille
Co-encadrant (invite)	Sébastien Pecqueur	Chargé de recherche. IEMN, CNRS, Université de Lille

University of Lille, ED ENGSYS Doctoral School of Engineering and Systems Sciences
IEMN Institute of Electronics, Microelectronics and Nanotechnology

PhD thesis
Submitted for the degree of Doctor of Philosophy from University of Lille
Specialty Electronics, microelectronics, nanoelectronics and microwaves

Presented by Kamila JANZAKOVA
May 11, 2023

Développement de dendrites polymères organiques en 3D comme dispositif neuromorphique

Development of 3D organic polymer dendrites as neuromorphic device

Composition of jury:

Reviewer	Yoeri van de Burgt	Associate Professor. Eindhoven university of Technology
Reviewer	Mamatimin Abbas	Researcher, HdR. CNRS, IMS, University of Bordeaux
Examiner	Jennifer Gerasimov	Principal Research Engineer. Linköping University
President of jury	Vincent Thomy	Professor. University of Lille
Examiner	Stéphane Lenfant	Research Director, HdR. IEMN, CNRS
Thesis director	Yannick Coffinier	Research Director, HdR. IEMN, CNRS, University of Lille
Thesis co-director (invited)	Fabien Alibart	Researcher, HdR. IEMN, CNRS, University of Lille
Co-supervisor (invited)	Sébastien Pecqueur	Researcher. IEMN, CNRS, University of Lille

Acknowledgments

This Ph.D. project has been quite a long, challenging, but at the same time intriguing and exciting journey with its ups and downs. I would like to express my appreciation to all those who have made this Ph.D project a reality and to those who have supported me throughout this time.

First and foremost, I would like to express my sincere gratitude to my thesis supervisors Dr. Fabien Alibart, Dr. Yannick Coffinier and to my co-supervisor Dr. Sébastien Pecqueur, who accepted me for this Ph.D. position, involved me in this interesting topic and allowed me to experience first-hand what research is all about. Due to their invaluable guidance, constant support and advice, it was possible to realize this work. Given the interdisciplinary nature of the project, I am deeply grateful for their invaluable expertise, knowledge and insights that have been imparted by each of them. Their invaluable contributions allowed me to define the trajectory of my PhD research and helped me to cope with the challenges of this period. They were always open to discussions and provided me with constructive feedback on the obtained results and findings. Furthermore, I am grateful to them for helping me understand various scientific techniques and tools, as well as their help with experiments when it was necessary. Their mentorship and constant encouragement have not only enhanced the quality of my work but also influenced my personal and professional development in the research field.

Moreover, I would also like to acknowledge the financial support for my thesis provided by the European Commission (ERC) in the framework of the IONOS project.

I want to express my appreciation to the jury members. Thanks to Prof. Yoeri van de Burgt and Dr. Mamatimin Abbas for reviewing my manuscript and for their positive recommendations regarding it. I also would like to acknowledge Dr. Jennifer Gerasimov, Dr. Stéphane Lenfant and Prof. Vincent Thomy for their thorough evaluation of my thesis and the rich and interesting discussion during my defense. The questions and valuable feedback I received from jury members allowed me to look at my project from a different angle and in a more detailed manner.

Many thanks to the administrative assistants Nora Benbahlouli and Andy Ledent, Emmanuelle Gillmann and Florence Senez for their help with paperwork and documents.

I would also like to thank all the members of the NCM team, especially Dr. Stéphane Lenfant for his help with administrative and organizational questions and Dr. David Guerin for his guidance in the laboratory of organic chemistry.

During this Ph.D. period, I have been fortunate to meet many interesting people with different backgrounds and career paths, especially those who are just starting their professional journey. In this regard, I am very grateful to my Ph.D. companions and colleagues, especially Cécile, Hugo, Corentin, Mahdi, Ankush, Anna, Milan, Anne-Sophie, Imen, Michel, Kiril, Paul, Giuseppe, Louis, Philippe, Yevheniia and Akash. Many thanks for their support, the good time spent together, the interesting and informative discussions and for creating a good atmosphere in the laboratory.

In addition, I am thankful to my friends. In particular, thanks to Natalia, Tamina, Anna for the heartfelt talks. Many thanks to Marina and Chakib for encouraging me and their help with rehearsing my presentation. Thanks a lot to Madina and Mykhailo for coming from far away to support me on the day of my thesis defense.

Finally, I am extremely grateful to my family (especially my mother, aunt and grandparents) for listening to my complaints, believing in me and supporting me always and in all my endeavours.

Abstract

In recent years, there has been a need for more advanced and energy-efficient computing. In turn, neuromorphic computing is a promising alternative to conventional one. Neuromorphic technologies aim to replicate attractive brain features such as high computational efficiency at low power consumption on a software and hardware level. At the moment, brain-inspired software implementations (such as ANN and SNN) have already shown their successful application for different types of tasks (image and speech recognition). However, to benefit more from the brain-like algorithms, one may combine them with appropriate hardware that would also rely on brain-like architecture and processes and thus complement them. Neuromorphic engineering has already shown the utilization of solid-state electronics (Complementary Metal Oxide Semiconductor (CMOS) circuits, memristor) for the development of brain-inspired devices. Nevertheless, these implementations are fabricated through top-down methods. In contrast, brain computing relies on bottom-up processes such as interconnectivity between cells and the formation of neural communication pathways.

In the light of mentioned above, this work reports on the development of programmable 3D organic neuromorphic devices, which, unlike most current neuromorphic technologies, can be created in a bottom-up manner. This allows bringing neuromorphic technologies closer to the level of brain programming, where necessary neural paths are established only on the need.

First, we found out that PEDOT:PSS based 3D interconnections can be formed by means of AC-bipolar electropolymerization and that they are capable of mimicking the growth of neural cells. By tuning individually the parameters of the waveform (peak amplitude voltage -V_P, frequency - *f*, duty cycle - dc and offset voltage - V_{off}), a wide range of dendrite-like structures was observed with various branching degrees, volumes, surface areas, asymmetry of formation, and even growth dynamics.

Next, it was discovered that dendritic morphologies obtained at various frequencies are conductive. Moreover, each structure exhibits an individual conductance value that can be interpreted as synaptic weight. More importantly, the ability of dendrites to function as OECT was revealed. Different dendrites exhibited different performances as OECT. Further, the ability of PEDOT:PSS dendrites to change their conductivity in response to gate voltage was used to mimic brain memory functions (short-term plasticity -STP and long-term plasticity - LTP). STP responses varied depending on the dendritic structure. Moreover, emulation of LTP was demonstrated not only by means of an Ag/AgCl gate wire but as well by means of a self- developed polymer dendritic gate.

Finally, structural plasticity was demonstrated through dendritic growth, where the weight of the final connection is governed according to Hebbian learning rules (spike- timing- dependent plasticity - STDP and spike-rate-dependent plasticity - SRDP). Using both approaches, a variety of dendritic topologies with programmable conductance states (i.e., synaptic weight) and various dynamics of growth have been observed. Eventually, using the same dendritic structural plasticity, more complex brain features such as associative learning and classification tasks were emulated.

Additionally, future perspectives of such technologies based on self-propagating polymer dendritic objects were discussed.

Résumé

Ces dernières années, le besoin d'une informatique plus avancée et plus économe en énergie s'est fait sentir. L'informatique neuromorphique est une alternative prometteuse à l'informatique conventionnelle. Les technologies neuromorphiques visent à reproduire les caractéristiques attrayantes du cerveau, telles qu'une grande efficacité et une faible consommation d'énergie, au niveau des logiciels et du matériel. À l'heure actuelle, les implémentations logicielles inspirées du cerveau (telles que ANN et SNN) ont déjà démontré leur efficacité dans différents types de tâches (reconnaissance d'images et de la parole). Toutefois, pour tirer un meilleur parti des algorithmes inspirés du cerveau, il est possible de les combiner avec une implémentation materielle appropriée qui s'appuierait également sur une architecture et des processus inspirés du cerveau. L'ingénierie neuromorphique s'est principalement appuyée sur les technologies conventionnelles (Complementary Metal Oxide Semiconductor (CMOS) circuits, memristor) pour le développement de circuits inspirés du cerveau. Néanmoins, ces implémentations sont fabriquées suivant une approche top-down. En revanche, l'informatique cérébrale repose sur des processus bottom-up tels que l'interconnectivité entre les cellules et la formation de voies de communication neuronales.

À la lumière de ce qui précède, ce travail de thèse porte sur le développement de dispositifs neuromorphiques organiques programmables en 3D qui, contrairement à la plupart des technologies neuromorphiques actuelles, peuvent être créés de manière bottom-up. Cela permet de rapprocher les technologies neuromorphiques du niveau de programmation du cerveau, où les chemins neuronaux nécessaires sont établis uniquement en fonction des besoins.

Tout d'abord, nous avons découvert que les interconnexions 3D à base de PEDOT:PSS peuvent être formées au moyen d'électropolymérisation bipolaire en courant alternatif, permettant d'imiter la croissance des cellules neuronales. En réglant individuellement les paramètres de la forme d'onde (tension d'amplitude de crête - V_P, fréquence - *f*, duty cycle- dc et tension de décalage - V_{off}), une large gamme de structures semblables à des dendrites a été observée avec différents degrés de ramification, volumes, surfaces, asymétries et dynamiques de croissance.

Ensuite, nous avons montré que les morphologies dendritiques obtenues à différentes fréquences sont conductrices. De plus, chaque structure présente une valeur de conductance qui peut être interprétée comme un poids synaptique. Plus important encore, la capacité des dendrites à fonctionner comme OECT a été révélée. Différentes morphologies de dendrites ont présenté des performances différentes en tant qu'OECT. De plus, la capacité des dendrites en PEDOT:PSS à modifier leur conductivité en réponse à la tension de grille a été utilisée pour imiter les fonctions de mémoire du cerveau (plasticité à court terme -STP et plasticité à long terme -LTP). Les réponses à la STP varient en fonction de la structure dendritique. En outre, l'émulation de la LTP a été démontrée non seulement au moyen d'un fil de grille Ag/AgCl, mais aussi au moyen d'une grille dendritique en polymère développée par électropolymérisation.

Enfin, la plasticité structurelle a été démontrée par la croissance dendritique, où le poids de la connexion finale est régi par les règles d'apprentissage de type Hebbien (plasticité dépendante du moment de l'impulsion - STDP et plasticité dépendante du rythme de l'impulsion - SRDP). En utilisant les deux approches, une variété de topologies dendritiques avec des états de conductance programmables (c'est-à-dire le poids synaptique) et diverses dynamiques de croissance ont été observées. Finalement, en utilisant la même plasticité structurelle

dendritique, des caractéristiques cérébrales plus complexes telles que l'apprentissage associatif et les tâches de classification ont été émulées.

En outre, les perspectives futures de ces technologies basées sur des objets dendritiques polymères ont été discutées.

Table of content

General introduction

Nowadays, modern digital technologies require new alternatives for advanced computing due to growing amount of data and tasks that must be processed efficiently with less energy ressources. This need is due to the following facts: the von Neumann architecture of modern computers, where data transfer is limited due to the physical separation of memory and processing units; the increase in the number of transistors on a chip, and the resulting problem of increasing the power required to operate such a chip. One of the possible solutions to overcome these challenges is the development of neuromorphic engineering, which is aimed at replicating attractive brain features such as parallel computing, high efficiency, low power consumption, and high functional and structural adaptability at the hardware level. So far, brain- inspired software technologies (such as ANN, SNN) have already shown successful implementations for various types of tasks, such as image and speech recognition, for instance. Nevertheless, one should run such brain-like algorithms on appropriate hardware that would complement them, which is one of the objectives of neuromorphic engineering. Currently, neuromorphic devices are designed to mimic the structure and function of biological neurons or their individual components (synapses, soma). Most of these implementations are realized with Complementary Metal Oxide Semiconductor (CMOS) circuits (brain-inspired chips) and emerging electronic devices (memristor and OECT, for example). These implementations are based on solid-state electronics manufactured through top-down methods, implying that fabricated electrical connections and network parameters are predefined. However, brain computing relies on bottom-up processes such as interconnectivity between cells and the formation of neural communication pathways. Therefore, devices that rely on the same bottom- up approach could benefit from biological concepts. One major advantage is that the formation of new connections within such devices will be possible at the same time as programming, without the need to manufacture multiple electrical connections beforehand. Hence, it may undoubtedly contribute to improving computing efficiency and power consumption in general.

Another important aspect of neuromorphic engineering is material choice. An interesting alternative to silicon-based technologies is organic materials, due to their versatile engineering platform within which one can implement bottom-up fabrication methods. Moreover, in organic materials, not only electronic species but also ionic species are used as mobile charge carriers. In such systems, the interaction of electronic and ionic species can be realized through numerous basic physical processes, such as electrostatic charge polarization and redox charge transfer. Thus, the use of organic materials provides more routes for the fabrication of neuromorphic devices as well as various leverages for their operation.

In light of the above, the aim of this manuscript is to develop organic-based neuromorphic devices capable of reproducing neural genesis and exhibiting neural-like functions.

Thus, throughout this study, the most suitable method for achieving this aim will be presented. As well, various brain-like functions will be implemented.

In the chapter 1 of my manuscript, I will present a brief overview of the neuromorphic engineering domain. The limitations of current computing technology will be described, as well as why brain-inspired computing is an attractive alternative to more advanced and powerful computing. Different neuromorphic devices based on different working principles, architectures, materials, and methods of fabrication will be reviewed. I will concentrate on organic materials' description and their features as an attractive tool for mimicking brain-like

functions, especially on organic mixed ionic electronic conductors (OMIEC). As well, I will describe why the utilization of organic material is an effective strategy for the development of bottom-up neuromorphic devices. To support this point, two electropolymerization approaches using direct current (DC) and alternating current (AC) will be considered. Finally, several well-known examples of using these electropolymerization methods to develop bottom-up controllable neuromorphic devices will be presented.

The chapter 2 will focus on how one can use the aforementioned AC electropolymerization method to create 3D polymer (PEDOT:PSS) structures that are capable of emulating the shape of biological neurons and their growth. This chapter will describe how, through modification of an applied AC signal, one can change the morphology of these structures, i.e., dendrites, and at the same time affect their growth dynamics.

Next, the chapter 3 will present how the obtained dendritic morphologies can function as organic electrochemical transistors (OECTs) and exhibit different performances. We will also demonstrate that dendritic OECTs can mimic synaptic plasticity, including short- and long-term plasticity.

In **Chapter 4**, I will show that PEDOT:PSS dendrites can exhibit not only synaptic plasticity but also structural plasticity governed by Hebbian learning rules. In this scenario, AC electropolymerization is not realized as in Chapter 2, but signals are applied from both wires and aimed at replicating spike-timing and spike-rate-dependent activity through different time periods of spikes overlap or spikes frequency, respectively. Furthermore, by means of dendritic structural plasticity, other brain features like the learning process (Pavlovian conditioning) as well as classification tasks will be demonstrated.

Finally, the main results and findings achieved during this thesis will be summarized in a conclusion section. Additionally, I will present some future perspectives on this topic.

Chapter 1. General concept and motivation

1. Need in new computing paradigm

Currently, one can observe an active development of modern digital technologies that are aiming to perform not only trivial tasks but also much more complicated programming. However, with an increasing amount of data that needs to be processed, the IT sphere has faced urgent demand for more enhanced computing development. The main reasons justifying this need are the following.

1. **Memory wall or so-called Von Neumann bottleneck**. The majority of modern computers are based on von Neumann architecture according to which the system consists of several main functional units **(Figure 1)**: memory units (MUs), central processing units (CPU)[1]. Respectively, data are stored in memory units and programs processing is carried out in central computing units (CPUs). These key elements are physically separated at different locations due to their incompatibilities in fabrication processes. Data transfer between them occurs via a communication path. For operations implementation, the data from memory units has to be fetched and transferred to CPUs with its following returning to memory after computing.

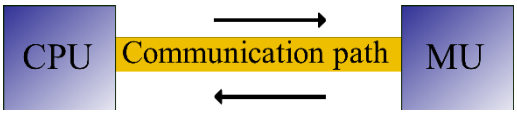

Figure 1. Schematic of Von Neumann architecture (memory wall).

However, the amount of information growing with time and the complexity of tasks revealed that data exchange in between two units increase power consumption and processing time. Thus, this connection path, or so-called "Von Neumann bottleneck", inevitably becomes the energetic and speed limitation for efficient computing[2].

To overcome this issue, numerous decisions for improving processor speeds and memory storage have been proposed. Recent achievements concerning MU have allowed storing more data on smaller chips, however the transfer rate has remained unaltered. Similarly, faster CPUs idle for a long period waiting for data to be received. As a result, the data transfer rate is still limited by the bottleneck, posing a problem for system efficiency[3,4].

2. **Moore's Law**. The law is mostly known under this name, but it derives from the work of R. Dennard, and it postulates that the number of transistors on a computer chip will double about every two years[3], highlighting the physical limitation of transistors' quantity that one can place on a chip **(Figure 2a)**. (Initially, Moore's law is an empirical formulation mainly related to the minimization of production costs while increasing the integration density of transistors. Nevertheless, the real scaling law for the transistors was theorized by R. Dennard, who confirmed a doubling of integration density and a 40% gain in frequency with decreasing transistor size[5].

Increasing the number of transistors is feasible through down-scaling. However, down-scaling devices to atomic, molecular, or nanocluster levels may lead to the loss of bulk material properties and thus fuzzy operations inside the system. These problems are typical for materials

used to fabricate electronic devices since semiconductor physics governs space charges in continuous media, which does not hold at scales where charge carriers are few and discrete. Aside from that, the growth of operations frequency directly affects an increase in power consumption[6]. To compensate for diminishing transistors' size, the operating frequency of a chip has to be increased for faster computation. However, frequency increase requires higher power density. At one point, the increase in the operating frequency will be restricted due to too excessive energy dissipation by heat that has to be managed by small chips to keep their temperature in their operational range. This is the so-called heat wall **(Figure 2b)**. Therefore, a significant boost in operating frequency as a consequence of size scaling will be impossible without damaging the chip.

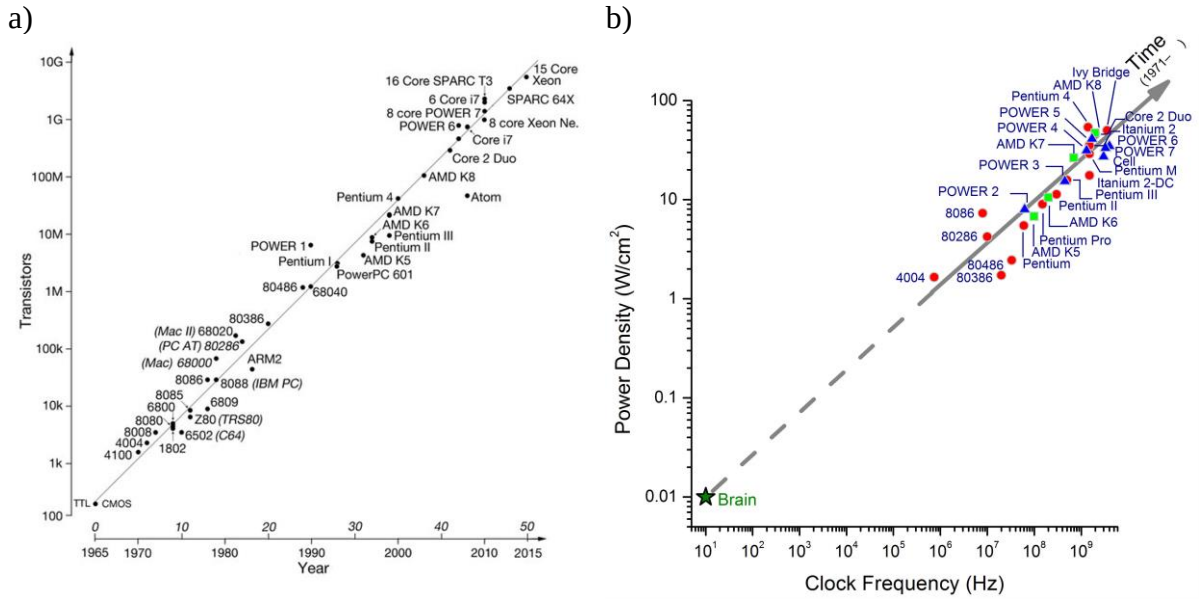

Figure 2. a) Moore's law[7]. b) Graphical representation of increasing power density trend as a function of processors' clock frequencies (heat wall)[6].

Therefore, in order to meet the requirements of modern ICT (Information & Communication Technologies) challenges, computing capability and power consumption in applied technologies needed to be balanced, which is, in fact, hardly achievable by exploiting the von Neumann architecture[3].

2. Biological neural network and synapses

Brain may serve as a possible inspiration for solving aforementioned challenges. The human brain is a complex system composed of 10^{11} neurons and 10^{15} synapses that fold into a highly interconnected neural network, where each neuron, on average, communicates with other 10^4 neurons[8]. Such structure allows carrying out storage and processing of data simultaneously at the same physical location and due to its high interconnectivity in a parallel manner. Moreover, it exhibits high performance in terms of speed with a power dissipation of ≈ 20 W only[9,10,11]. Additionally, the brain is capable of adapting to complex environments, self- programming, and complex processing.

The elementary building block of the biological neural network is the neuron. They are packed into highly dense, interconnected systems and capable of receiving, integrating and transmiting data via biochemical signals. Neurons interact with each other at junctions called synapses. Typical biological neurons' structure consists of the cell body (soma) housed by dendrites that receive signals (inputs); branching from the soma. Axon transfers signals to the dendrites of other neurons through the axon terminals.
Communication in the neural system occurs between neurons via specialized contacts known as synapses. Specifically, signals are sent from "pre-synaptic neurons" to a "post-synaptic neuron" that receives them (**Figure 3)**[12,13]. The "strength" of the transmitted signal from the pre-synaptic "sending" terminal to the post-synaptic "receiving" one is proportional to the strength of their interconnection, known as the synaptic weight (W). The summation of all the input signals is carried out by each neuron. When this summation exceeds a certain threshold, it transmits a fire signal to the next neurons[14].

Synapses play a significant role in the realization of learning, memory, and adaptability of the human brain[15]. The synaptic weight is regulated through the concentrations of ions (e.g., Ca^{2+}, Na^{+}, and K^{+}) during pre-synaptic action potentials (APs), which adjust the release of neurotransmitters.

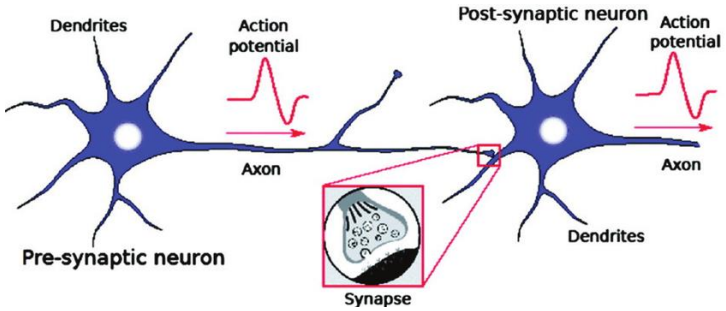

Figure 3. Communication between pre- and post-synaptic biological neurons[16].

The synaptic weight controls the coupling between interconnected neurons through electrical or chemical signals and influences the transmission of spikes/signals to neighboring neurons that results in a rise in neuronal connectivity and functions.
Following the Hebb's postulate, any modifications in synaptic strength (i.e., synaptic plasticity) are related to activity processes on both sides of a synapse. It is believed that memory in the human brain comes out as a result of two types of synaptic plasticity: short-term plasticity (STP) and long-term plasticity (LTP).
STP occurs after a one-time stimulation as a temporary enhancement of synaptic strength, which lasts for tens of milliseconds to a few minutes and then rapidly returns to its initial state. STP is required for short-term memory (STM) and enables the execution of important computational functions such as transmission, encoding, and filtering of neuronal signals. In contrast, LTP originates from repeated stimulations causing continuous changes in the synaptic strength and may last for hours or years[17].
LTP has been associated with long-term memory (LTM). It is responsible for storing processed information and is considered essential for memory and learning capabilities. STP can be transferred into LTP by regulating the rate and/or intensity of the spikes produced by pre- synaptic and post-synaptic neurons[18,19,20].

Other neural mechanisms underlying learning and memory are associated with Hebbian synaptic plasticity and represented by. two main paradigms: spike-timing-dependent plasticity (STDP) and spike-rate-dependent plasticity (SRDP)[21].
According to STDP, synaptic changes happen with respect to the activity time-correlation between pre- and post-synaptic neurons[22], while SRDP shows the influence of the activity frequency of pre-synaptic and post-synaptic signals on synaptic strength[23,24].

3. Artificial neural network

The idea of brain-inspired calculation paved the way for a new computing paradigm. The most famous form of bio-inspired information processing is machine learning, more precisely an artificial neural network (ANN)[25]. ANNs are a class of algorithms with a nodal and parallel structure originally inspired by the brain, aiming to solve machine-learning tasks[15].
Following the model of a layered ANN, such a topology contains input, hidden, and output layers with interconnected artificial neurons (nodes) to simulate the brain's neural connections **(Figure 4 c)**. Similar to biological mechanisms, signals are processed by nodes and transmitted to the next ones only if the cumulative signal exceeds the threshold **(Figure 4 a,b)**[26].

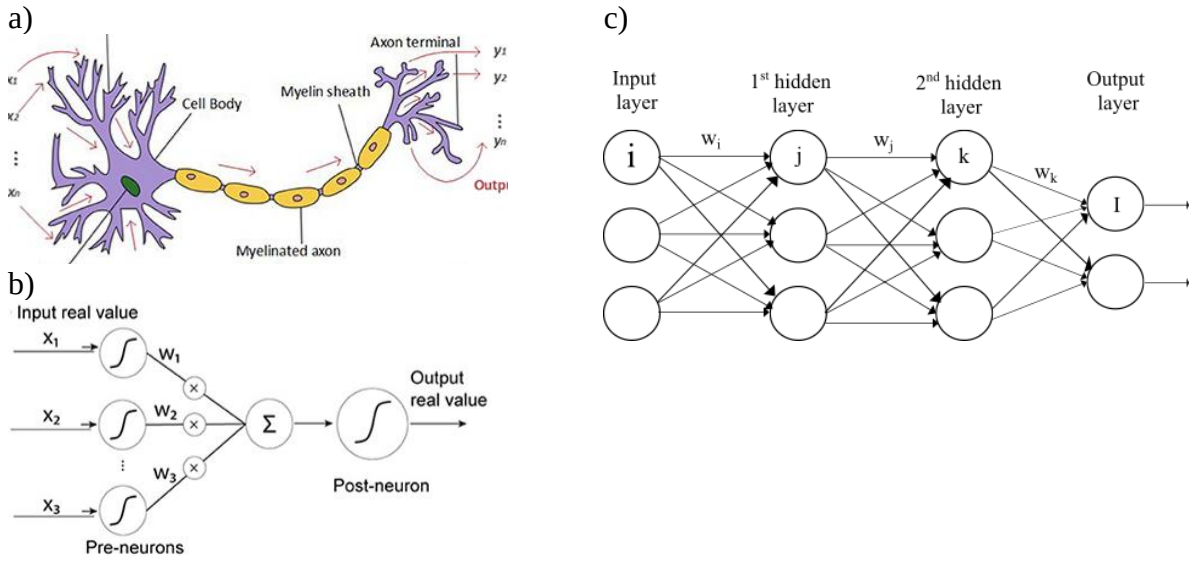

Figure 4. a) Schematic illustration of signal processing and transmission by a) biological neuron and b) artificial neuron as part of c) Artificial Neural Network[13].

To date, ANN software has already shown successful results in its applications for pattern, image, and text recognition. Thus, neuromorphic computing is viewed as a promising computing approach for contributing to big data analysis, the Internet of Things (IoT), artificial intelligence (AI), etc.[24]. However, they are still executing on conventional von Neumann machines.
Therefore, although ANNs results are satisfactory for pattern recognition, their performance and energetic requirements are incomparable to their biological counterparts, which limits their application in IoT, where huge compromises have to be made between time, size, weight and temperature[27]. Therefore, to benefit from the brain-like algorithms, one needs to run them on

brain-like machines to achieve outstanding energy efficiency for practical online multi-tasking mode.

4. Top-down manufactured neuromorphic hardware

The first prototype of an artificial neural machine, SNARC (Stochastic Neural-Analog Reinforcement Computer), appeared in the 1950s and was constructed from vacuum tubes to simulate a network of 40 neurons[28].

Since then, various emerging materials and hardware implementations have been discovered and addressed. Mostly, they are known either in the form of emerging electronic devices replicating neurons and their individual components (synapses, soma) or as circuits emulating much bigger brain neural networks.

One of the most well-known and widely used technologies is silicon-based CMOS (Complementary Metal Oxide Semiconductor transistors) integrated circuits. In the 1980s, Carver Mead first utilized metal-oxide–silicon (MOS) transistors for analog distributed- computing circuits (instead of using Boolean logic) to mimic neurons and synapses. Namely, the current–voltage characteristics of (MOS) transistors in the subthreshold regime were used to mimic exponential neuronal dynamics[29]. Furthermore, these technologies[30,31] were already capable of emulating event-driven and large-scale spiking neural networks. The latest works showed its application for the implementation of so-called “Brain on chip” technologies.

4.1 Brain-inspired chips

Brain-inspired chips are designed to simulate the way the brain functions, referring to human brain neuron structure through microelectronics technology. Brain-inspired chips adopt a new type of CMOS circuits architecture that emulates millions of neurons and synapses capable of rendering spike-based computations (**Figure 5**)[32]. In comparison with conventional chips, it provides superior advantages in terms of power consumption, learning capacity, and computing efficiency.

a) b)

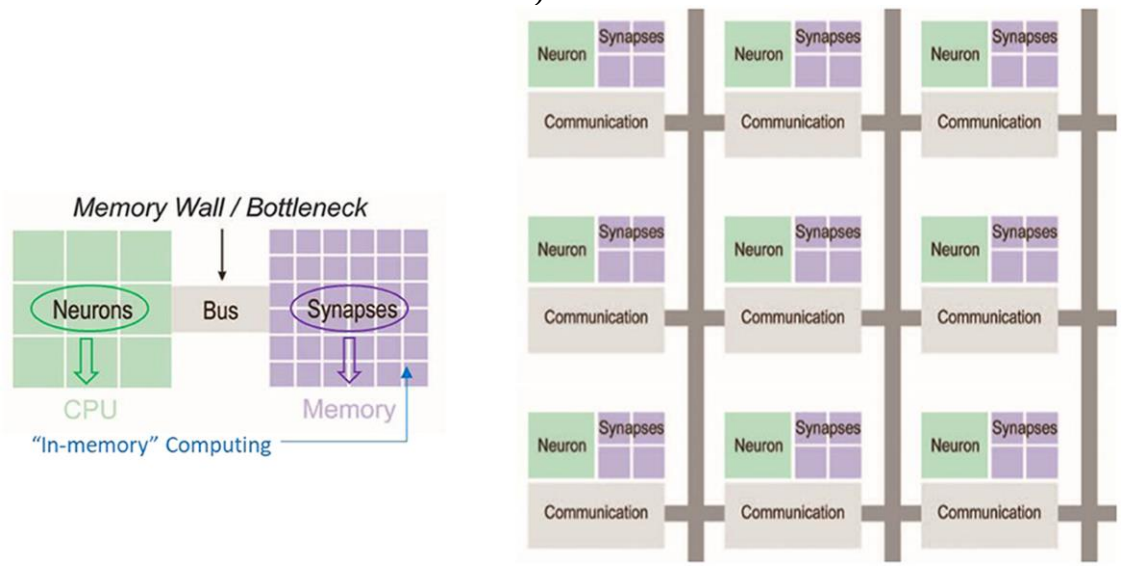

Figure 5. Comparison of a) the traditional Von-Neumann architecture and b) the new brain-inspired chip crossbar architecture[13,6].

For instance, one of the representatives of these chips is the TrueNorth chip from IBM (**Figure 6**), which includes 5.4 billion transistors to integrate 1 million programmable spiking neurons and 256 million adjustable synapses. TrueNorth has been demonstrated to be capable of multi-object identification and categorization tasks with a very low power consumption of 73 mW[6,13,32]. Another example reported in 2017 is Intel's Loihi chip, which includes 128 neuromorphic cores, each containing 1024 primitive spiking neural units arranged into tree-like structures to simulate, in total, around 131 thousand neurons and nearly 130 million synapses. In comparison with TrueNorth, the Loihi chip can execute not only identification and categorization tasks but also self-learning based on spike neural networks (SNNs)[33]. Other "Brain chip" implementations known at the moment are Neurogrid[34], BrainScaleS[35], and SpiNNaker[36].

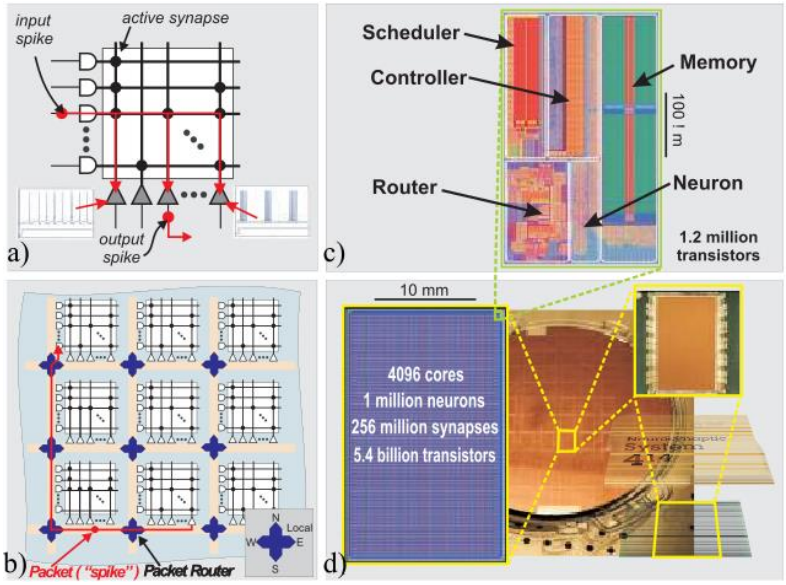

Figure 6. Representative of 'Big Brain' chips. TrueNorth architecture is shown at 4 structural levels. a) Functional illustration of a core crossbar unit in which horizontal lines play the role of axons, individually programmable synapses are cross-points, vertical lines are neuron inputs, and triangles are neurons. Information, as in biological counterparts, travels from axons to neurons through active synapses. Herein, neurons can be individually programmed. b) Functional chip architecture, where cores' units are packed in a two-dimensional array. In this architecture, sending spike events (packets) via a mesh routing network allows for carrying out long-distance connections for target axon activation. c) The physical organization of the core in 28 nm CMOS that fits in a 240 µm→390 µm footprint. d) Chip layout as 64×64 cores, wafer, and a chip package[6].

However, CMOS based technologies are facing crucial challenges:

1. It is inherently volatile, meaning that all the written data will be lost immediately after turning off the power supply or in the case of a power failure[37].
2. It utilizes a large silicon area that consequently requires intensive current and power consumption due to high transistor density.
3. Another challenge is the incompatibility with biological realism. In biology, processes refer to a broad variety of information transfer carriers such as ions and molecules[38,39]. On the contrary, electrons are the only information carriers in CMOS-based chips. As a result, sophisticated silicon circuitry is used to replicate each component of biology separately, and consequently, it may lead to the complexification of silicon circuits. Consequently, neuromorphic technology must strike a compromise between biological realism and hardware complexity, which might be a hindrance to neuromorphic engineering.
4. Poor scalability. Managing highly parallel and asynchronous system remains a challenge[32,40]. A complication of further scalability is especially crucial in terms of developing brain like 3D parallel computing[3,20,40]. Neural networks in biology exist in 3D massively parallel, densely interconnected, and self-organized structures. For instance, from the rough estimate, one pre-neuron may project its signal onto 1000 post-neurons. This gives biology an incredibly large amount of freedom to perform many tasks in parallel. It is worth noting that although biological neurons transmit signals slower in comparison with electrical circuits, brain can still execute operations more quickly than any traditional computer due to its 3D parallel network packaging[41]. However, with 2D technologies that are rapidly approaching interconnection's limits, achieving this level of parallelism remains difficult.

Therefore, the perspectives of 3D integration into neuromorphic chips can be summarized as follows:

1. Solving the 2D neuron routing congestion issue, increasing the network's interconnectivity and scalability while decreasing critical-path lengths;
2. Creating numerous 3D interconnections in between hardware layers that offer high device interconnection density and, as a consequence, low-power density;
3. Producing a high-complexity system that can handle parallel processing and computational tasks with significant demands.

Thus, the development of 3D devices based on different interconnectivity levels may contribute to reaching necessary parallel computing and achieving a new level of biomimicry.

4.2 Emerging nonvolatile memory technologies

Despite the impressive achievements of Brain chip technologies, they are still subject to Moore's Law. The enlarging scale will inevitably lead to an increase in power consumption. Concurrently, transistors can show flaws while mimicking the dynamic characteristics of neurons and synapses.

Additionally, brain-inspired CMOS chips mostly rely on volatile memory (VM). In VM, information is lost once the system is powered off. There are two main types of VM: Dynamic Random-Access Memory (DRAM) and Static Random-Access Memory (SRAM).

In contrast to VM, non-volatile memory (NVM) can keep the data stored in the device while the system is switched off. So, all the data will always be retained within the system and not be

lost. Thus, NVM technologies may serve as a key to improve memory functions in CMOS neuromorphic circuits.
However, in terms of data reading and writing speed, VMs have undeniable advantages because of their fast speed operation, whereas NVMs have a higher writing latency in general. One additional con of NVM is that after a certain number of writing cycles, the storage of data will fail because the memory storage will reach its limit. For an ideal memory, there should be a compromise in between NVM's characteristics like data remaining in the system, and VM's characteristics of high speed and no read and write restrictions within a certain range[13].
Taking all this into consideration, NVM technologies propose to utilize emerging memory devices that enable in-memory computing (data is processed in situ)[42] and can be divided into two groups: 2-terminal devices and 3-terminal devices. These technologies have different novel materials and storage mechanisms[43].
Usually, non-volatile memories complement CMOS circuits in the form of organized crossbar arrays[44], providing high integration density and high computational parallelism.

4.2.1 Emerging nonvolatile two-terminal devices

2-terminal devices are presented by memristors (memristive devices, resistive memories) designed as two terminal devices where dielectric material is sandwiched in between two metal electrodes. Memristors' key feature is the ability to switch resistance states of their dielectric material when different voltages are applied across it.
Upon different voltages applied across electrodes, the dielectric material can change its resistance state with further possibility to reverse the switching. Some memristive devices are capable of continuously functioning in this manner, but they have limitations in terms of variability in switching and endurances. Note that the written information will not fade even if the power is off.
Memristors can be composed of chalcogenide compounds, carbon-based materials, ferroelectrics, transition metal oxides, and ferromagnetic metals. Based on such an abundance of materials, various mechanisms such as phase transition, molecular restructuring, quantum mechanical phenomena, and ion reaction can be realized. This feature distinguishes the NVM switching mechanism from the traditional electronic processes in CMOS based memories. These mechanisms have been used to provide an analogy to the ion channels contained in the membranes of neurons and synapses in the brain[13].
In recent years, new storage devices have been represented as resistive random-access memory (RRAM), conducting bridge random-access memory (CBRAM), phase-change memory (PCM), ferroelectric random-access memory (FeRAM), and magnetic random-access memory (MRAM) technologies[45].
To date, two-terminal memristors have been successfully introduced as part of non-volatile memory arrays in the form of crossbars (**Figure 7**) that are aimed to mimic synapses. The arrays are formed from conductive rows (word lines) and columns (bit lines) perpendicular to each other, where memory elements are inserted at the intersection between them[46].
The working principle of memristive crossbar arrays for in-memory computing is based on the following: once pulses are applied to artificial synapses (or memory cells), the corresponding current is generated and further summed according to Ohm's law and Kirchhoff's current law. Next, this signal is transferred to the neuron to produce the final output current, which accomplishes the inference operation. During the training, after completing each inference operation, the weight of the memory cell could be updated.

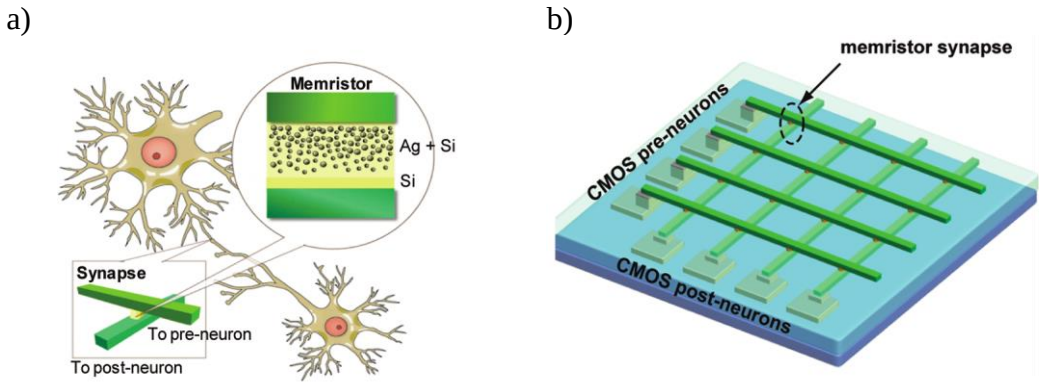

Figure 7. Schematic example of a crossbar hardware architecture where two-terminal memristor synapses form at each crosspoint and connect every single neuron in the "pre-neuron" layer of the crossbar configuration to every neuron in the "post-neuron" layer with unique synaptic weight. a) Schematic representation of memristors' geometry reproducing concept of synapses' between neurons. b) Illustration of a neuromorphic crossbar configuration with CMOS pre- and post- neurons and memristor synapses[47].

Such types of crossbar synapses network can be comparable to biological systems in terms of connectivity, function density, and operating principle. Their application has already been demonstrated for data processing and simple pattern recognition tasks at a relatively lower energy consumption[48,49]. However, crossbar technologies face limitations: issue of access from edges, issue of scalability due to wire resistance contribution and sneak path, issue of independent control of each crosspoint.

Apart from 2D crossbar structure to increase synaptic device density and implement parallel computing, memristors were also introduced in a 3D manner by integrating successive layers of memory arrays (**Figure 8**)[2]. Nevertheless, all these devices still rely on predefined CMOS technologies that impose strong constraints on the fabrication process (*i.e.*, thermal budget, multiple masks design).

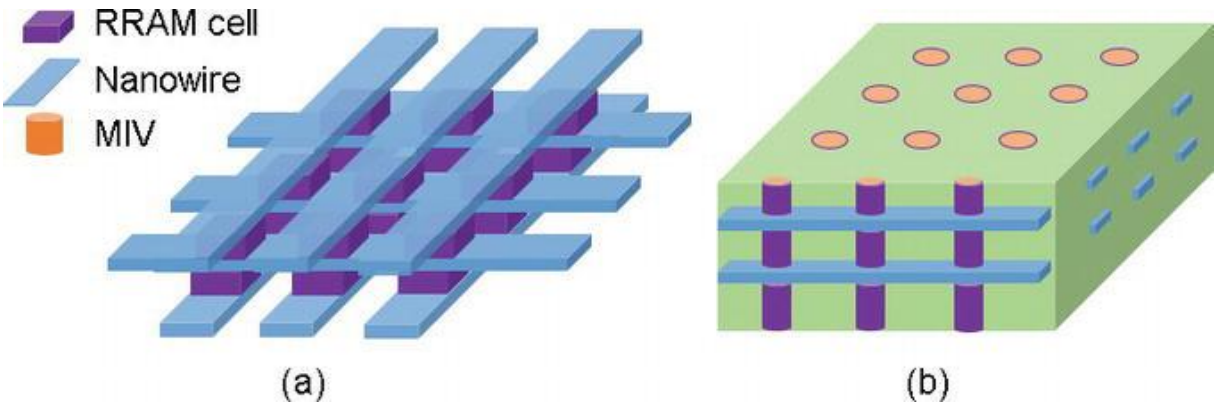

Figure 8. 3D RRAM architecture: (a) horizontal 3D structure and (b) vertical 3D structure[2].

In general, controllable conductance in two-terminal resistive memories has been shown to encode different types of synaptic-like behaviors, including short- and long-term memory (STM/LTM), paired-pulse facilitation (PPF) and depression (PPD), spike-timing-dependent plasticity (STDP), spike-rate-dependent plasticity (SRDP) and metaplasticity[50].

4.2.2 Emerging nonvolatile multi-terminal devices

Nevertheless, two-terminal architecture is capable of emulating mostly homosynaptic plasticity (Hebbian-type learning rules like STDP)[51], in which specific changes occur exclusively at synapses that were directly involved in the activation of a cell during the induction (pre-synaptic activation). Another important form of plasticity is heterosynaptic one. Heterosynaptic plasticity refers to generating changes at synapses that were not initially active during the induction[52].

Thus, in order to increase devices' performance and benefit from complementary computational properties, heterosynaptic plasticity was addressed in neuromorphic systems involving multi- or three-terminal devices.

The structure of such devices is similar to two-terminal memristors but includes a supplementary terminal that is usually presented by a gate. Therefore, the device consists of three terminals (gate/source/drain electrodes), switching material as channel, and electrolyte laying in between the gate and the channel (**Figure 9, 10**).

The gate electrode governs the electric field across the active material through the application of voltage signals[53]. Namely, the gate's signals drive mobile ions from the electrolyte into the channel or *vice versa*. The injected or extracted mobile ions affect the doping level of the switching material, and cause changes in channel conductance.

Such a type of interaction is closer to the heterosynaptic plasticity principle and can be used to reach multi-level conductance states, which are essential for the emulation of potentiation and depression characteristics[20].

Compared to two-terminal devices, the presence of an additional terminal provides more precise control of the device conductance and, consequently, synaptic weight. It as well allows splitting the "read" and "write" (programming) processes, which is unachievable by 2-terminal technologies. Additionally, employing supplemental electrodes gives an opportunity to introduce not only a single synaptic junction, but also several artificial synapses[51], where both of the aforementioned possibilities (adjusting the synaptic weight and separating the "write" and "read" processes) can be achieved.

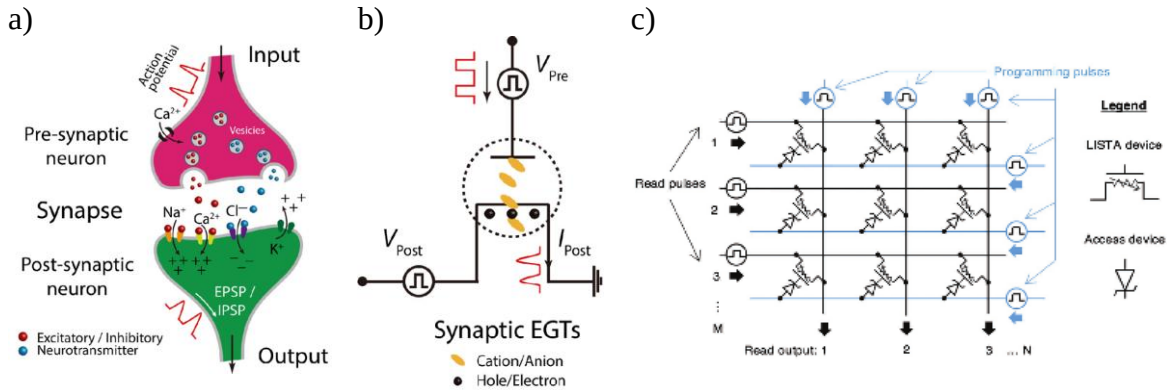

Figure 9. Representation of a) a biological synapse and signal transmission in it; b) example of electrolyte-gated transistors (EGT) as an artificial synapse[24]. c). A voltage programmed crossbar array using the 3-terminal device (LISTA)[54].

To date, three-terminal devices such as electrochemical, ferroelectric, and charge-trapping transistors have already been demonstrated to function as artificial synapses[54,55,56].

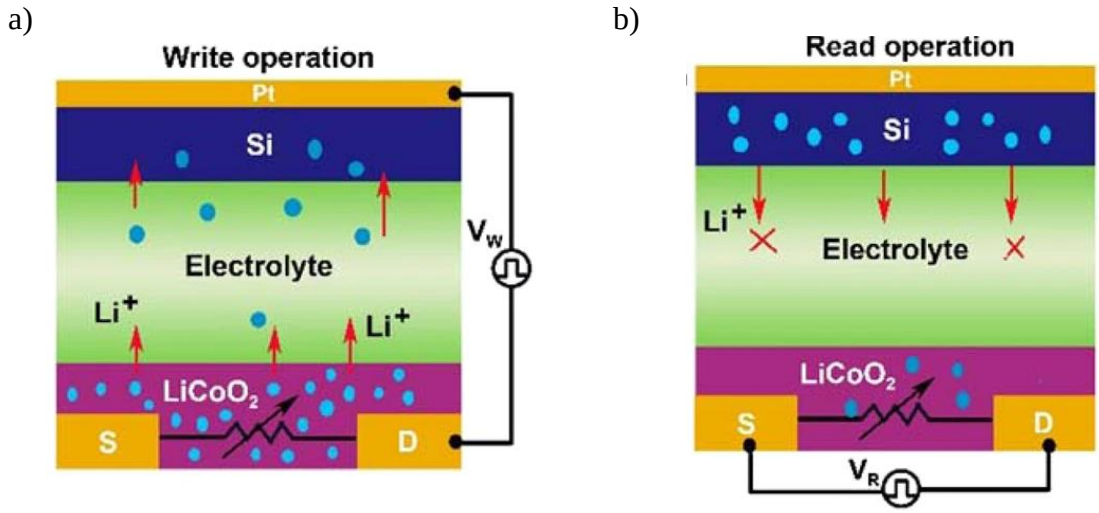

Figure 10. Example of a three-terminal device consisting of Source, Drain and Pt gate in the form of the inorganic electrochemical transistor with a $Li_3POxSex$ electrolyte. a) "Write" operation's representation as extraction/injection process of Li^+ ions from/to $LiCoO_2$ channel leading to conductivity modification. b) Schematic representation of "read" operation carried out once extraction/injection of Li^+ ions is accomplished. The readout is executed by applying an insignificant voltage between the source and the drain terminals[20].

In 3-terminal technologies, both inorganic and organic materials are used as channels. Organic electrochemical transistors (OECTs) are of particular interest for emulating neuromorphic features due to the versatility of material properties and the flexibility of their engineering[55,57,58] . Typical OECT structure resembles inorganic counterparts but with an organic semiconductor channel located in between source and drain[59]. As an organic channel, organic mixed ionic electronic conductors (OMIEC) are used. The operating principle is based on ions' insertion from the electrolyte into the bulk of organic material, which results in doping or dedoping state changes and further facilitation or decreasing the conductivity of the channel[59,60]. Similar to inorganic transistors, OECT have shown their capability to act as artificial synapses too[20,58].

5. Bottom-up manufactured neuromorphic hardware

Most of all the above-mentioned devices are developed with the help of top-down methods, resulting in production of all possible electrical connections and units, which are aimed to mimic input and output neurons. In such top-down fabricated devices, location of electrical connections and network parameters are determined in advance upon device fabrication. Nevertheless, brain computing largely refers to different self-assembly processes such as interconnectivity between cells and the formation of neural communication pathways with respect to brain needs. Thus, to profit more from biological concepts and be able to establish only specific connections upon programming, one needs to address such devices with similar bottom-up approaches as in the brain.

5.1 Nanocell

Along with top-down techniques, the construction of circuits can also be achieved in a bottom- up manner, for instance, through the chemical assembly of molecules. The idea behind molecular self-assembly circuits is that randomly organized devices (transistors, diodes or switch) can be utilized for building complex functions even if the single device operation is not guaranteed.

On the other hand, the disadvantage of such systems is that assembled circuits may not possess all the desirable characteristics. Fortunately, some molecules have already shown high intrinsic conductive properties[61,62] and have been addressed as consolidated programmable devices[63] to behave analogously to logical gates. Such a bottom-up approach was named "programmable nanocell" or simply the nanocell. The nanocell concept suggests replacing current semiconductor silicon materials in electronic devices with molecular ones[64].

Among Nanocell approaches, Tour *et al*. were the first to demonstrate production of memory circuits (through self-assembly approach) out of disordered systems without employing pre- requested painstaking as in the case with CMOS circuits[65].

The device was presented by pairs of gold electrodes onto a silicon dioxide substrate with a set of discontinuous gold islands vapor-deposited in between electrodes (**Figure 11**). By immersing the substrate into a solution containing Au nanowires encapsulated with the organic compound- oligo(phenylene ethynylene), this study shows how one can interlink deposited Au islands and Au nanowires via an oligo(phenylene ethynylene) (OPE). Thus, through continuous steps of chemical reactions, Nanocell study showed the way to establish conductive links on the 2D device through the self-assembly method. Additionally, Nanocell exhibited replicable switching behavior and two types of memory effects (destructive read and nondestructive read) that were stable for over a week.

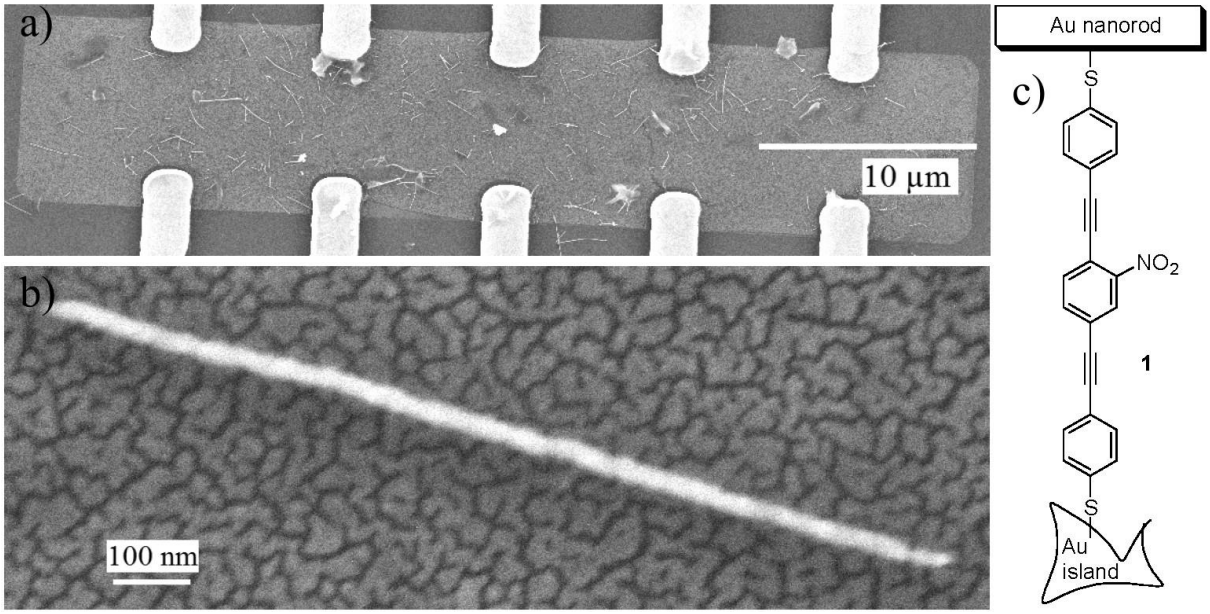

Figure 11. a) NanoCell's SEM image representing fabricated Au electrodes and assemblies of the Au nanowires and OPE. b) Magnified image of the NanoCell's central portion showing attached Au nanowire the disordered discontinuous Au film. c) Schematic illustration of the Au nanorods and Au islands link through OPE-dithiol[65].

5.2 Bottom-up organic devices

As well, another attractive tool for the development of neuromorphic devices is organic electronic materials (OEMs), as it was shown in the case with OECT. On top of this, the utilization of such types of materials provides with much more paths for devices' fabrication, including bottom-up options thanks to the versatility of chemical synthesis, soft fabrication, and additive processes.
Following the purpose of this thesis, we would like to focus on the description of organic electronics in this section. It will allow for a better understanding of the neuromorphic device that will be presented in the next chapter. We will consider the origin of electronic properties; the most commonly used organic electronic material for neuromorphic technologies and methods of its production in bottom-up way.

5.2.1 Organic electronics

OEM are presented by carbon-based small molecules (oligomers), π-conjugated conducting polymers; carbon allotropes (fullerenes, nanotubes, graphene); molecular ensembles of them and hybrid/composite materials that are capable to exhibit electronic transport and thus conduct electricity.
One of the attractive features of organic materials is their potential to structure mechanically flexible, stretchable, low-cost manufacturing devices that cannot be implemented with silicon or any other inorganic based technologies. Another big advantage is the ability to tune necessary properties (for example, conductivity or morphology) by tuning the molecular structure of organic materials through chemical modifications during the synthesis step or further exploitation (doping/dedoping). Additionally, OEMs have the perspectives to interface with the biological system and thus find its application in bioelectronic engineering. All these attractive features have already been implemented in various fields: optoelectronics (organic photovoltaics/organic solar cells, organic light-emitting diodes); transistor technology; electro- chemo-mechanical devices (sensors, actuators).
Recently, OEM has become a promising tool for neuromorphic devices development due to the possibility to control and program needed properties and the diversity of charge carriers, gathering both electronic and ionic mobile species.

Charge transport in organic electronic materials

Electrons in atoms are located at energy levels. In turn, each energy level is subdivided into subshells containing atomic orbitals (s, p, d, f), or regions where the probability of finding electrons of a certain energy is most likely. According to the theory of molecular orbitals, bonds in molecules are formed as a result of hybridization and overlap of these atomic orbitals. Based on the molecular orbital theory, the origin of the electronic properties of the OEM is explained. More precisely, the structure of the carbon atom contains six electrons arranged in electron configuration $1s^2 2s^2 2p^2$, where four electrons are located at the outer electronic orbital. During interaction with other atoms like (Hydrogen, Oxygen, Carbon, etc.) s and p orbitals of the outer shell in carbon combine and hybridized either into sp, sp^2 or sp^3 orbitals.
In oligomers and polymers, the structure is mostly composed of sp^2 hybridized carbon atoms that allow the formation of conjugated double bonds along the skeleton of the molecule. Both single and double bonds contain a localized σ-bond, which provides a strong chemical

connection between atoms. Double bonds as well include a localized π-bond, which is weaker than the σ-bond. Since all carbons in π-conjugated systems are sp^2 hybridized, unhybridized p_z orbitals of adjacent carbon atoms overlap that consequently allowing to spread electron density over a broader area and so to create electron delocalization along the backbone of the whole molecule as shown in (**Figure 12)**. Therefore, this electronic delocalization forms a continuous π-σ- π delocalized system across which electrons (or positive charges) can transfer throughout the molecular chain and finally result in electrical conductivity[66].

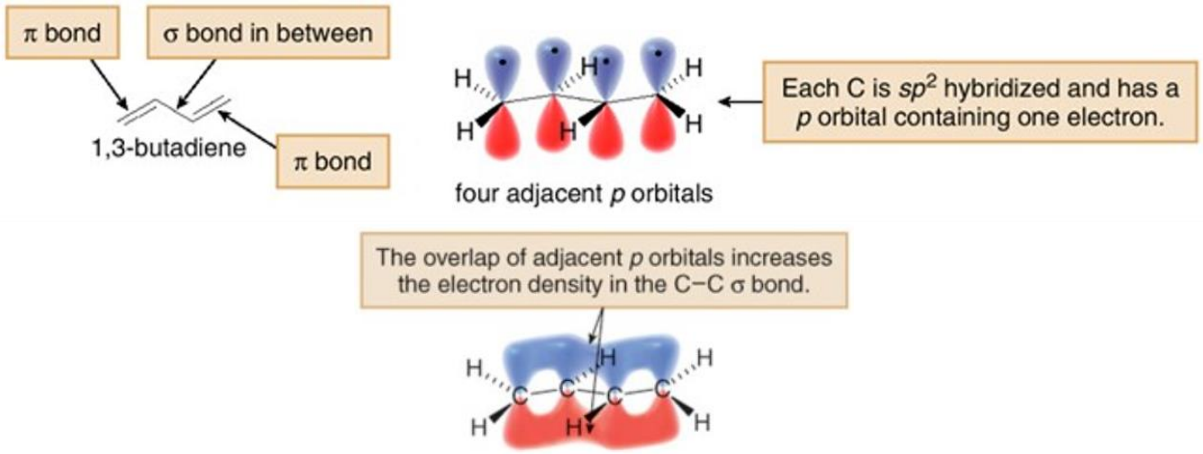

Figure 12. Example of 1,3-butadiene electronic structure[67].

Another important point is that in conjugated organic systems, parallel p_z orbitals, depending on their wave functions, can generate π bonding (during in-phase overlap) and π* antibonding (during out of phase overlap) molecular orbitals. The bonding orbitals obtain a lower energy level and contain Highest Occupied Molecular Orbital (HOMO) while antibonding orbitals have a higher energy state and contain Lowest Unoccupied Molecular Orbital (LUMO) (**Figure 13**).

To break or form the bonds inside the organic compounds and have a chemical reaction, a certain amount of energy should be provided to the molecule. This power is usually related to the energy difference between the HOMO and LUMO levels, or the so-called HOMO-LUMO gap. By giving the external energy equivalent to the energy gap, the electron goes from bonding to anti-bonding orbitals, resulting in an unstable state, namely breaking or forming a chemical bond and occurring a chemical reaction.

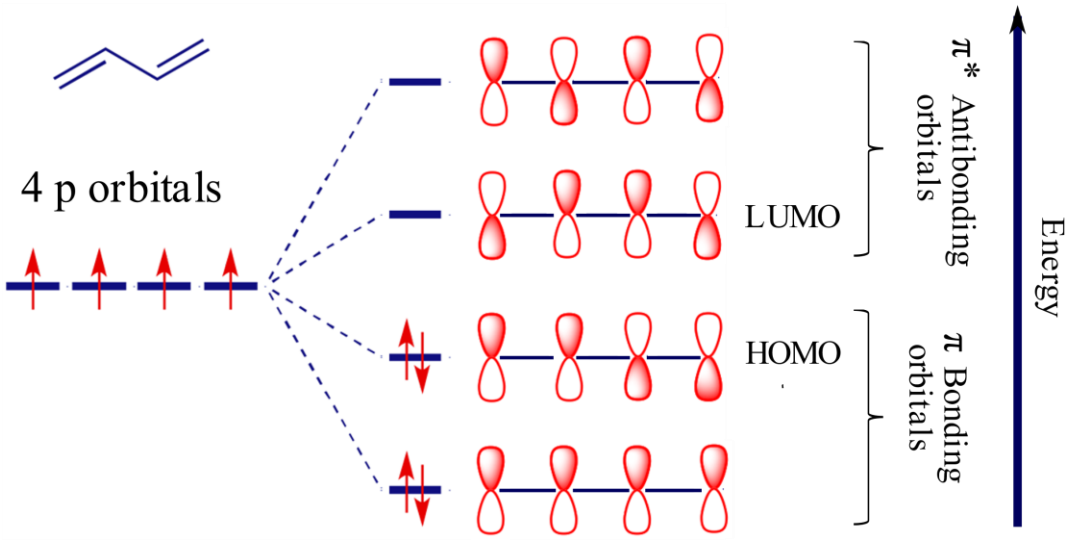

Figure 13. Formation of π bonding and a π* antibonding orbital of 1,3-butadiene. The lower energy state is created due to the in-phase overlap of 4 orbitals with similar lobs. The next energy level is represented by two orbitals' pairs with two different in-phase lobs overlaps known as HOMO. The lowest energy level within antibonding orbitals contains only one pair of in-phase orbitals and two out-of-phase orbitals acting for LUMO. The highest energy level gathered from orbitals all overlapped out of phase (adapted from [68]).

Using molecular orbital theory, such discrete states for electron energy in organic conjugated systems can be comparable to the energy bands in inorganic semiconductors.
According to this analogy, the valence electrons of inorganic semiconductors crystals populate the valence shell, which represents the energy level (valence band). Once excess energy is supplied to the electron, it can escape the valence shell, become a free electron, and exist in the so-called conduction band.
The energy difference between the valence band and the conduction band is known as band gap (E_g). Once the electron has switched to conductance band, it is capable of moving all over the material without being tied to a particular atom. Based on the size of this energy gap in terms of conduction, materials can be divided into conductors, insulators, and semiconductors. In conductors, the valence band overlaps with the conduction band, so the valence electrons are capable of moving and propagating in the conduction band without activation energy. For charge-transfer insulators, the band gap is too large for electrons to pass through, therefore they are unable to conduct electricity. Semiconductors have small energy gaps that electrons can overcome upon excitation and leave a hole behind them (that will be discussed further).
Therefore, concerning this theory in organic molecules, the Highest Occupied Molecular Orbital (HOMO) is equivalent to the valence band while the Lowest Unoccupied Molecular Orbital (LUMO) corresponds to the conduction band. The HOMO-LUMO energy difference is the band gap. Given the small size of the HOMO-LUMO gap, organic conjugated materials can be classified as semiconductors.
Moreover, repeating monomer units is leading to increasing number of bonding and antibonding orbitals that consequently can bring the HOMO and LUMO energies closer to each other, and thus reduce the bandgap as it can be seen in **Figure 14**.

Nevertheless, the level of charge carrier mobility in organic semiconductors is significantly lower than in inorganic crystalline semiconductors due to weak intermolecular interactions carried out due to van der Waals forces and π–π interactions.

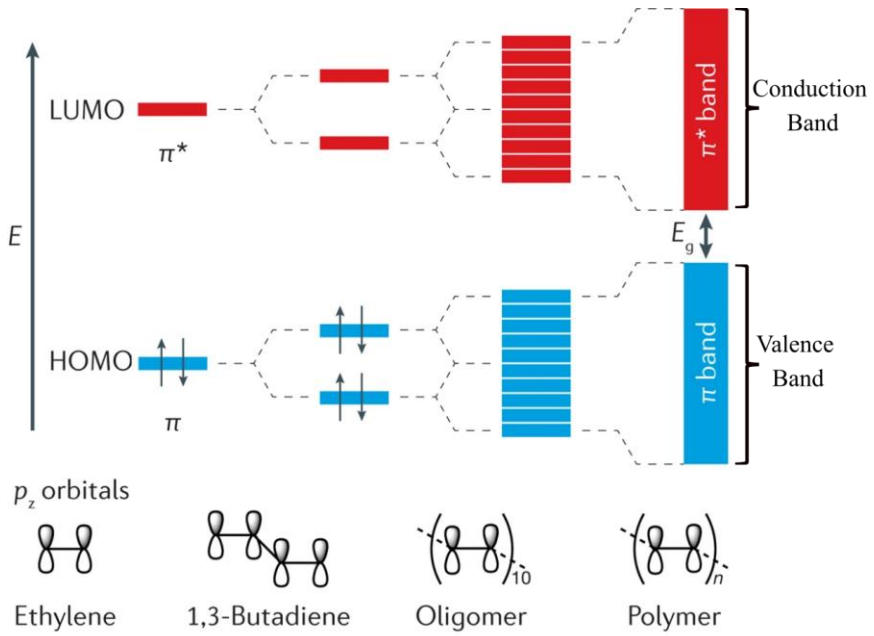

Figure 14. Representation of HOMO-LUMO energy levels and correlation between the bandgap size and the quantity of overlapping p_z orbitals[69].

Doping

The conductivity of undoped pristine polymers (acting as insulators) or polymers with low conductivity can be facilitated through doping. This process is carried out through oxidation or reduction reactions of a polymer with a dopant to create additional charge carriers (electrons or holes) within the material structure[66].
There are two types of doping: p-type and n-type. In the case of p-type doping, the polymer is undergoing an oxidation reaction that causes a break in a double bond. Furthermore, the removed electron transfers from the HOMO of the polymer to the dopant's LUMO. The parent molecule is left with a positive charge (hole or vacancy), and therefore a radical cation is formed inside the molecular chain. This hole generates a lack of electrons in the molecular chain. Electrons from neighboring double bond move to the hole's place to fill it, and so on, producing a flow of positive charges in the opposite direction as shown in **Figure 15a**.
Contrariwise in the case of n-type doping, reduction of the polymer occurs. The electrons from the dopant's HOMO transfers to the polymer's LUMO and therefore additional electrons contribute to electron density increasing and formation of a radical anion (**Figure 15b**).

From a chemical point of view, the radical cations or anions formed during oxidation/reduction processes are called positive and negative polarons, respectively. Further ejection or adoption of electrons leads to the formation of dication or dianion, which are called bipolarons.
The motion of these positive and negative charge carriers along conjugated organic systems generates conduction. Hence, doping can boost the density of charge carriers in the material.
In general, doping can be induced through chemical reactions via interaction with oxidizing and reducing agents. Additionally, electrochemical reactions of cathodic reduction (n-doped) and

anodic oxidation (p-doped) can be utilized for enhancing conductivity. As well, doping can be carried out through a photo-induced reaction when the organic semiconductor is affected by high-energy radiation that forces the electron to jump from the valence band (HOMO) to the conductance band (LUMO).

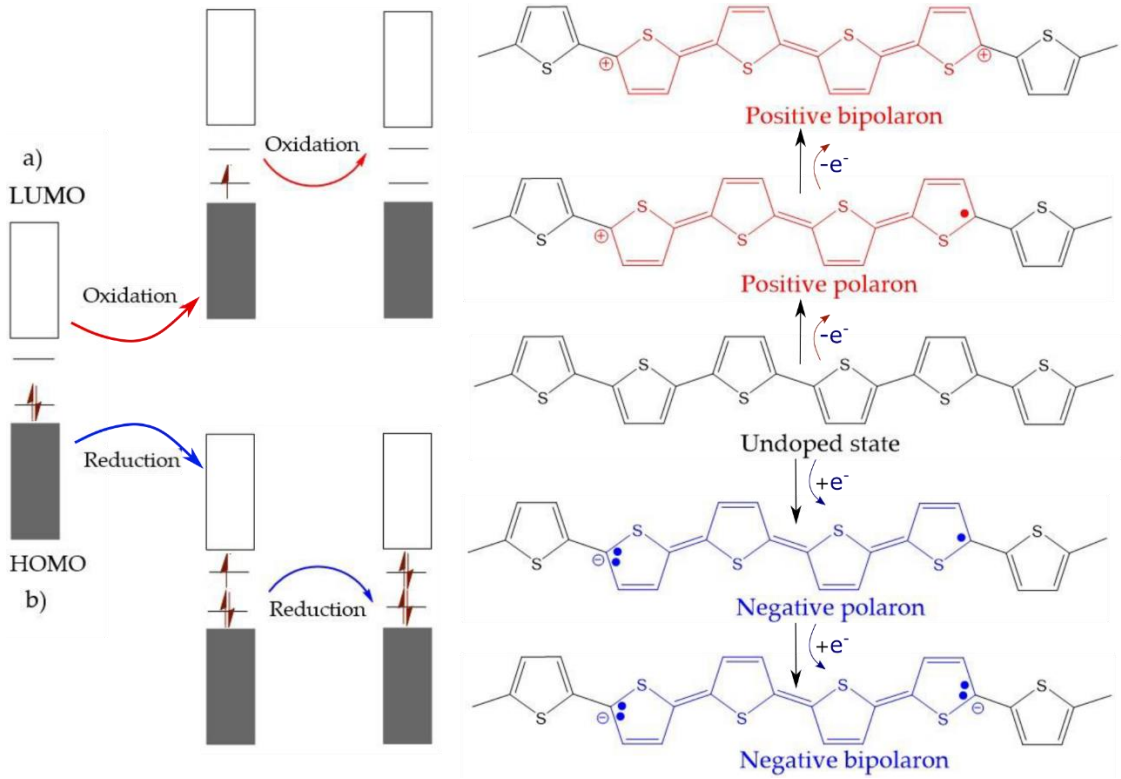

Figure 15. Schematic illustration of the electronic band and polythiophene (PT) chemical structures during **(a)** p-type doping (oxidation process shown in red arrows) and **(b)** n-type doping (reduction process shown in blue arrows). Oxidation/reduction provokes a loss/addition of π-electron from/to the undoped state (neutral PT chain) causing a local structural alteration from the benzenoid structure to a quinoid and formation of a polaron (bipolaron) consequently. Adapted from [70].

In addition to the doping level, charge transport as well highly depends on the temperature, the crystallinity of the material, in particular on the order of chains, and the presence of structural defects[71].

5.2.2 Organic Mixed Ionic Electronic Conductors

Except for electrons/holes transport, conductivity of OEM may derive from ionic species. Usually, such types of materials are achieved by blends of π-conjugated polymers that conduct electrons/holes and a polymer electrolyte that conducts ions similar to ion exchange membranes. These are so-called organic mixed ionic electronic conductors (OMIECs) that may as well include radical polymers and conjugated small molecule systems[72].
Therefore, because of this mixed structure, physical processes like electronic transport, ionic transport, and ionic–electronic coupling can be carried out inside the system and used further to control the efficiency of OMIEC-based devices[72].

PEDOT:PSS

The most ubiquitous representative of OMIEC is hole transport-based poly(3,4- ethylenedioxythiophene):poly(styrenesulfonate) (PEDOT:PSS) known for its relatively high thermal stability, immense mechanical flexibility, electrical conductivity, optical transmittance properties and low cost fabrication[73].

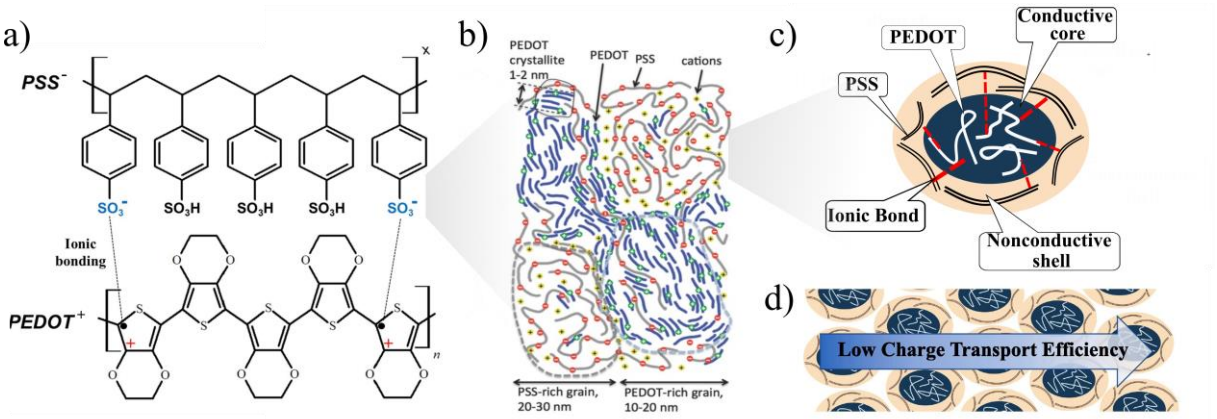

Figure 16. (a) p-type PEDOT:PSS chemical structures, b) Schematic illustration of polymer morphology exhibiting conductive PEDOT-rich grains and insulating PSS-rich domains.
(c) the core-shell structure of PEDOT:PSS particle, and (d) PEDOT:PSS particles distribution in a thin film (adapted from [73,74])

PEDOT:PSS is a mixed composition of conductive PEDOT (positively-charged ionic polymer) and insulator-like PSS (negatively-charged ionic polymer). In the completely oxidized PEDOT structure, an integral charge carrier corresponds to a three-monomer unit[75].
Acting as counter-ion, PSS allows counterbalancing the positive charges of PEDOT and enables cation mobility. Moreover, it serves as a soluble template that upgrades the solubility and chemical stability of PEDOT in aqueous solutions.
Positively charged short PEDOT and negatively charged long PSS chains are electrostatically bound through the Coulombic interactions. At the material level, these linked chains form ternary structured colloids where tangled hydrophobic PEDOT-rich domains are embedded in a hydrophilic PSS-rich amorphous shell matrix[76,77,78]. In other words, the PEDOT:PSS structure represents an intermolecular compounded solid surrounded by a liquid phase constituted by channel of electrolytes.
In PEDOT:PSS, metal-like properties derive from the fact of free charge carriers transport within conjugated PEDOT structure and the PSS chains are responsible for cationic conductivity[74].
The key attractive feature of PEDOT:PSS is capability of PSS matrix to soak water and solvated ions, once the material is immersed in an aqueous electrolyte solution[74,79,80]. This phenomenon is serving as a key operating mechanism for OMIEC based devices, in particular for OECT.
As it was described before, the mechanism of OECT is based on doping/ dedoping processes of the channel material. More precisely, upon positive gate bias, the injection of cations into the PSS part of the polymer blend takes place. The main role of positive cations is compensation of PSS sulfonic acid groups. Eventually, PEDOT:PSS layer becomes charge neutral, which leads to a decrease in the number of holes in the polymer. This process can be compared with

electrochemical dedoping upon which PEDOT switches from the oxidized ("ON") to the neutral ("OFF") state. It is described by the following reaction[24].

$$Pedot^{+}:Pss^{-}+Cat^{+}+e^{-}\rightarrow Pedot^{0}+Pss^{-}:Cat^{+} \quad (1),$$

where Cat^{+} are the cations injected in the polymeric blend[81].

Most commonly this specific polymer is obtained through oxidative chemical or electrochemical polymerization technique of 3,4-ethylenedioxythiophene (EDOT) monomers in the presence of a PSS- with various ratios of PEDOT and PSS inside the polymer matrix[82]. The ratio of PEDOT to PSS affects significantly the conductivity since it yields the density of charge transporting PEDOT sites.
Conductivity of the blend polymer can be eased not only via doping but as well through other various strategies: using different cosolvents, pH alteration, and annealing (heating for a long time) to allow the electron to reach an energetically favorite state[80].

In general, because of the aforementioned properties, OMIECs, especially PEDOT:PSS, have been actively used for a wide range of technologies: spans actuators[83], chemical sensors[84], light- emitting electrochemical cells[85], ion pumps[86], organic electrochemical transistors and circuits for sensing, and neuromorphic hardware[55,59].
OMIEC in this sense is especially attractive for neuromorphic implementation because of following advantages. Due to a variety of engineering approaches dedicated to fabrication of organic materials, a broad diversity of electronic properties relevant to brain-inspired engineering (conductance states) and generally to brain processes can be introduced and emulated.
Additionally, due to different nature of conductance deriving from charge carriers transport and ionic flux, OMIEC-based devices are closer in terms of functioning to biological realism. For instance, signal transfer within neurons is carried out through neuronal action potentials that result from ions, cations (K^{+}, Na^{+}, Ca^{2+}) and anions (Cl^{-}, HCO_3^{-}), flowing in and out of the neuron body.
This duality of properties in OMIEC allows electronic and ionic processes to be mixed and introduced via numerous basic physical interactions, such as electrostatic charge polarization or redox charge transfer[87]. Moreover, it is widening the range of resistance states and different ways to control them, which in turn is one of the main requirements for neuromorphic hardware[53]. It undoubtedly gives organic based chips advantages over conventional CMOS based technology to introduce more biomimicry.

5.3 Electropolymerization as bottom-up approach

As it was already mentioned, most of neuromorphic devices are built with the help of top-down methods. Nonetheless, examples of employing electropolymerization as the bottom-up approach have been reported.

5.3.1 DC electropolymerization method.

To date, most of the reports have demonstrated DC electropolymerization as an interesting technique for ameliorating the devices' electrochromic properties[88], optimizing dye-synthesized solar cells[89], improving sensing[90,91,92] and bioelectronics[93,94,95].
In addition, this method was also applied as self-assembly technique for OECT development for neuromorphic computing. One of the first works known in this direction demonstrated the *in situ* formation of organic polymer channels on a cluster of OECTs where the short-term memory effect was successfully implemented. Additionally, implementation of reservoir computing for pattern recognition was achieved due to different transient responses of produced OECTs[96].
Further, this method was applied to reproduce long-term potentiation with the help of electropolymerization and, therefore, to create, between pre-patterned electrodes, programmable transistor channels capable to exhibit a diversity of biomimetic functionalities[97,98].

5.3.2 AC bipolar electropolymerization method.

Apart from DC electropolymerization resulting in polymer film formation, recent studies have discovered the possibility to obtain organic conductive polymer in another unconventional forms. Namely, with the help of Alternating Current (AC) bipolar technique, it was shown how one may synthesize trees like PEDOT fibers as a result of EDOT oxidation[99,100,101,102,103,104]. These studies showed that conductive polymer dendrites can be fabricated without utilizing any supplementary templates defining growth patterns and that branches' propagation is mostly driven by an electric field.
One of the first studies on this topic (**Figure 17a**) showed the possibility to obtain PEDOT fibers at the terminus of wireless Au electrodes (bipolar electrodes (BPE)) that were immersed into acetonitrile (ACN) solution containing EDOT and located in between a pair of Pt driving electrodes that were not physically in contact with BPEs. AC voltage signal was applied to both Pt electrodes, which in turn provoked unconventional electropolymerization. Anodic and cathodic reactions were performed simultaneously on both poles of wireless electrodes. An important ingredient in this particular work was the presence of the sacrificial reagent- benzoquinone (BQ). The reduction of BQ to hydroquinone (HQ) occurring at cathodic part of the wire was serving to counterbalance EDOT oxidation at the opposite anodic part through consuming an excess of formed protons[99].
As an alternative to simplify the system and provide charges directly to EDOT from a metallic conductor, Eickenscheidt *et al*. exhibited growth of PEDOT dendrites in ACN solution without addition of BQ *via* pulsed electropolymerization on the free-standing electrode directly connected to the voltage source (**Figure 17b**)[104].

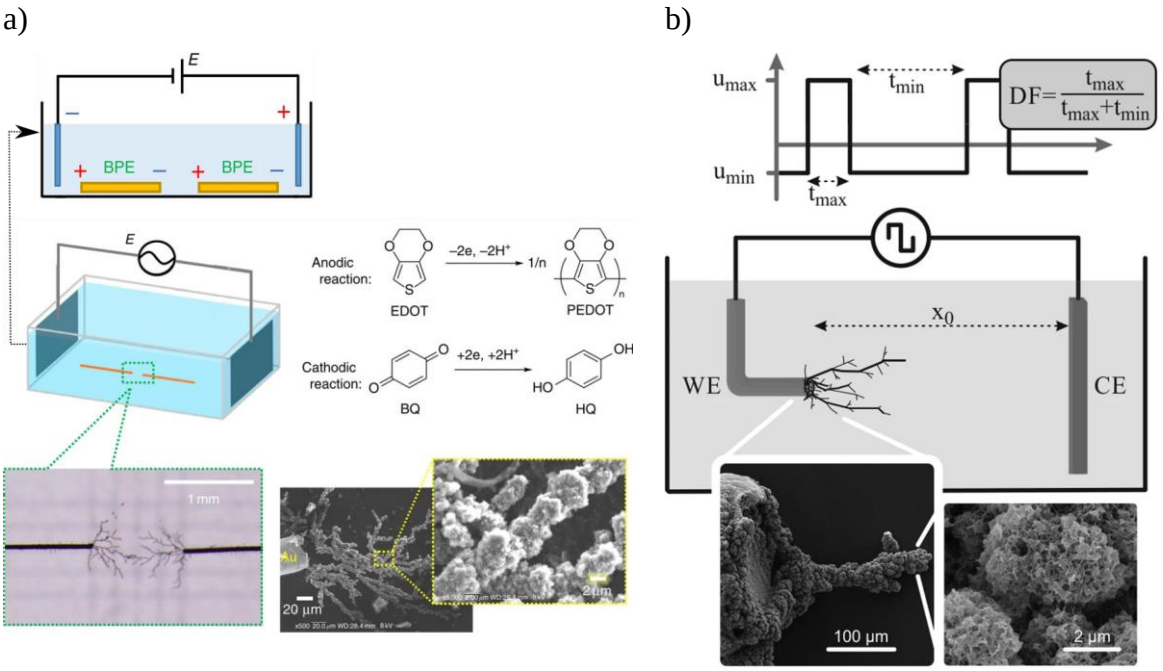

Figure 17. Examples of electrochemical setups for AC bipolar electropolymerization in cases when: a) dendrites' formation takes place at the tips of wireless bipolar electrodes (BPE) placed in between two Pt driving electrodes[99] and b) growth of PEDOT branches occurs on a free-standing working electrode (WE) in a 3D manner[104].

Moreover, it was shown that significant changes in dendritic structure morphology can be achieved by varying parameters of applied rectangular signals. For instance, Eickenscheidt *et al.* showed the effect of voltage amplitude and duty factor (DF) at a fixed frequency of 5 Hz on growth velocity, the degree of branching, and the general influence on final length, thickness, and branching complexity. With the duty factor, the duration of anodic phase during which the oxidation of EDOT occurred was modified. There was observed that a high degree of branching can be reached at DF of 25% and small cathodic voltages ($u_{\min} = -2 \ldots 0\ V$) while increasing DF resulted in a short-lasting cathodic phase and a diminishing number of branches (**Figure 18a**)[104].

In terms of BPEs, number of branches as well as PEDOT morphology can be modified by controlling frequency, type and concentration of utilized reagents (**Figure 18b**), solvent and supporting electrolyte (**Figure 18c**)[99,100].

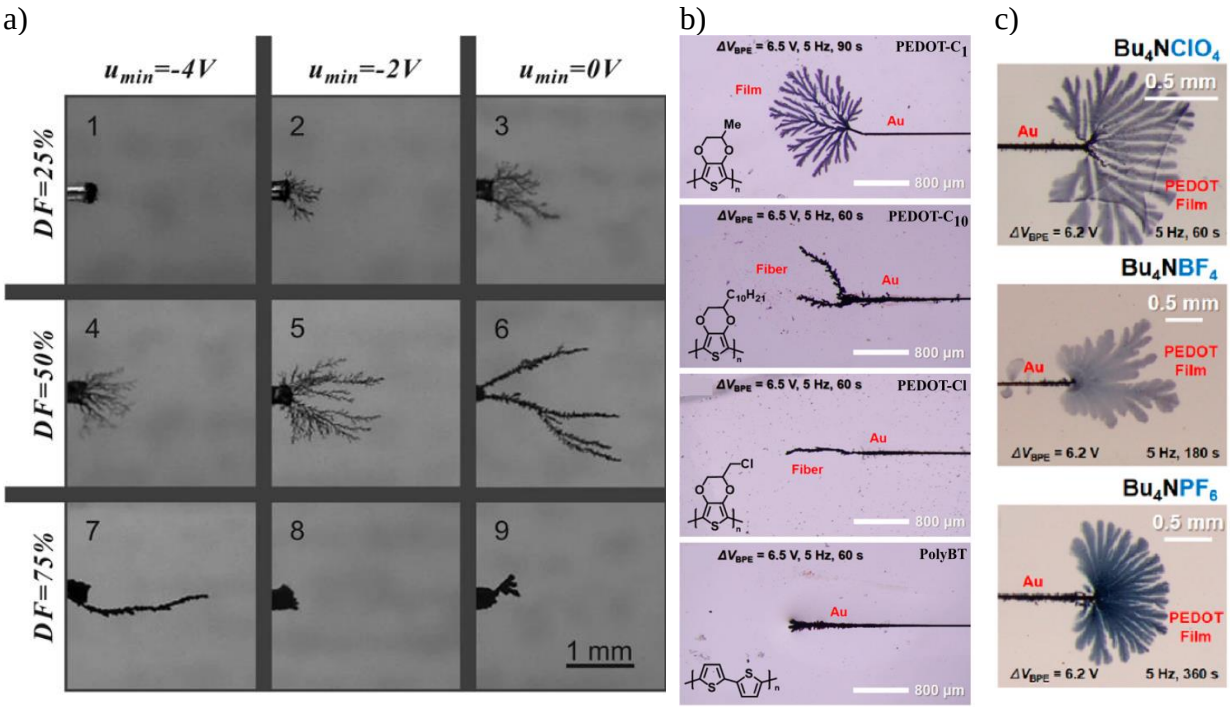

Figure 18. a) Growth behavior on the free-standing electrode after 120 s of electropolymerization upon signals with varying duty factors and negative potentials u_{min} values (positive amplitude value was constant)[104]. b) Optical microscopy images of dendritic structures grown at fixed conditions on BPEs using a) diverse EDOT derivatives as monomers (EDOT-C_1, EDOT-C_{10}, chloromethyl-substituted EDOT (EDOT-Cl), bithiophene (BT)) and c) various supporting electrolytes (ionic liquid tetrabutylammonium (Bu_4N^+) with either perchlorate (ClO_4^-), tetrafluoroborate (BF_4^-) orhexafluorophosphate (PF_6^-) as counterions)[100].

Therefore, the method of AC bipolar electropolymerization showed itself as a versatile approach to build organic conductive objects while modifying different constituents of a system: electrical parameters, types of electrodes, chemical content of the solution, and nature of monomers. Later on, this method of AC bipolar electropolymerization has been discovered as a useful tool for developing controllable bottom-up neuromorphic devices.

Organic neuromorphic devices developed through AC electropolymerization.

In 2014, Dang Nguyen Tuan *et al*. first introduced possibility to form polymer Polypyrrole (PPy) and PEDOT connections *in situ* upon bipolar voltage signals application on 2D prefabricated electrodes and proposed to utilize wire resistance as synaptic weight changes in machine learning algorithm[105]. Later, this concept was broadened by Megumi Akai- Kasaya *et al*. who demonstrated a variety of 2D wires growth rates, morphology dependency on applied electrical parameters and its correlation with dendrites resistance. Specifically, the relationship between diameter of electropolymerized wires and frequency of the applied waveform, effect of applied voltage amplitude on the density of grown wires were established. This opportunity to tune and control material electrical property was used as resistive change memory and addressed for supervised and unsupervised machine learning[106]. Further, Hagiwara *et al*. showed how one can replicate synaptic strength modifications (long- term potentiation and short-term potentiation) by applying continuous pulses with varied

frequency and amplitude voltage, thereby facilitating conductance changes in PEDOT:PSS fibers and consequently reflecting in different learning efficiency and retention time[107].
Recently, along with a demonstration of neuromorphic memory functions such as (STP, LTP), 2D dendrites were used to introduce the Hebbian learning rule (STDP), pattern recognition, and reservoir computing[108,109,110,111].
Additionally, by means of AC electrodeposition, PEDOT:PSS films were synthesized in between pre patterned pairs of Au pads and demonstrated to function as organic electrochemical transistors (OECTs) with tunable performance depending on the signal parameters settings[112,113].

Thanks to the diversity of bottom-up produced brain like technologies, Nanocell concept first showed that one may introduce a device with self-structured connections. However, this approach has a lack of control, so all the connections are established randomly. To contrast, when it comes to the electropolymerization approach, this method may provide much more control over the establishment of connections within the system. In this light, AC bipolar electropolymerization may be more attractive in comparison with DC electropolymerization due to the span of parameters that one can use to modify the final shape and properties of synthesized polymer and eventually induce a variety of conductance state and biomimetic functionalities.
Thus, electrochemistry can serve as a physical mechanism for the development of self-evolving neuromorphic networks that will possess brain-like computing functions and can allow reinventing computing devices from a new perspective.
Therefore, given the attractive features of bipolar AC electropolymerization as a fabrication method, in the framework of this dissertation, I will be studying self-evolving organic neuromorphic devices that can be created using this bottom-up method.

Literature

(1) Schuller, I. K.; Stevens, R.; Pino, R.; Pechan, M. *Neuromorphic Computing – From Materials Research to Systems Architecture Roundtable*; USDOE Office of Science (SC) (United States), 2015. https://doi.org/10.2172/1283147.

(2) An, H.; Bai, K.; Yi, Y. The Roadmap to Realize Memristive Three-Dimensional Neuromorphic Computing System. *Adv. Memristor Neural Netw. - Model. Appl.* **2018**. https://doi.org/10.5772/intechopen.78986.

(3) Tang, J.; Yuan, F.; Shen, X.; Wang, Z.; Rao, M.; He, Y.; Sun, Y.; Li, X.; Zhang, W.; Li, Y.; Gao, B.; Qian, H.; Bi, G.; Song, S.; Yang, J. J.; Wu, H. Bridging Biological and Artificial Neural Networks with Emerging Neuromorphic Devices: Fundamentals, Progress, and Challenges. *Adv. Mater.* **2019**, *31* (49), 1902761. https://doi.org/10.1002/adma.201902761.

(4) J. von Neumann in The Collected Works for John von Neumann, (Ed: A. H. Taub), Pergamon Press, Oxford, UK 1963.

(5) *L'éditorial par Emmanuel Dubois – IEMN*. https://www.iemn.fr/newsletter/52073.html (accessed 2023-03-22).

(6) Merolla, P. A.; Arthur, J. V.; Alvarez-Icaza, R.; Cassidy, A. S.; Sawada, J.; Akopyan, F.; Jackson, B. L.; Imam, N.; Guo, C.; Nakamura, Y.; Brezzo, B.; Vo, I.; Esser, S. K.; Appuswamy, R.; Taba, B.; Amir, A.; Flickner, M. D.; Risk, W. P.; Manohar, R.; Modha, D. S. Artificial Brains. A Million Spiking-Neuron Integrated Circuit with a Scalable Communication Network and Interface. *Science* **2014**, *345* (6197), 668–673. https://doi.org/10.1126/science.1254642.

(7) *Gherman, L., Moşoiu, O., & Bucinschi, V. (n.d.). INFORMATION RESOURCES MANAGEMENT BASED ON FEEDBACK THEORY IN A MILITARY ORGANIZATION. 8.*

(8) Morris, R. Book Review: Foundations of Cellular Neurophysiology, D Johnston and S M-S Wu, MIT Press. *Neuromuscul. Disord.* **1995**, *6*.

(9) Kandel, E. R.; Schwartz, J. H.; Jessell, T. M. *Principles of Neural Science*, 4th ed.; McGraw-Hill, Health Professions Division: New York, 2000.

(10) Backus, J. Can Programming Be Liberated from the von Neumann Style?: A Functional Style and Its Algebra of Programs. *Commun. ACM* **1978**, *21* (8), 613–641. https://doi.org/10.1145/359576.359579.

(11) Wright, C. D.; Hosseini, P.; Diosdado, J. A. V. Beyond Von-Neumann Computing with Nanoscale Phase-Change Memory Devices. *Adv. Funct. Mater.* **2013**, *23* (18), 2248–2254. https://doi.org/10.1002/adfm.201202383.

(12) Thomas, A. Memristor-Based Neural Networks. *J. Phys. Appl. Phys.* **2013**, *46* (9), 093001. https://doi.org/10.1088/0022-3727/46/9/093001.

(13) Lv, Y.; Chen, H.; Wang, Q.; Li, X.; Xie, C.; Song, Z. Post-Silicon Nano-Electronic Device and Its Application in Brain-Inspired Chips. *Front. Neurorobotics* **2022**, *16*, 948386. https://doi.org/10.3389/fnbot.2022.948386.

(14) Islam, R.; Li, H.; Chen, P.-Y.; Wan, W.; Chen, H.-Y.; Gao, B.; Wu, H.; Yu, S.; Saraswat, K.; Philip Wong, H.-S. Device and Materials Requirements for Neuromorphic Computing. *J. Phys. Appl. Phys.* **2019**, *52* (11), 113001. https://doi.org/10.1088/1361-6463/aaf784.

(15) Bian, J.; Cao, Z.; Zhou, P. Neuromorphic Computing: Devices, Hardware, and System Application Facilitated by Two-Dimensional Materials. *Appl. Phys. Rev.* **2021**, *8* (4), 041313. https://doi.org/10.1063/5.0067352.

(16) Huang, A.; Zhang, X.; Li, R.; Chi, Y. Memristor Neural Network Design. In *Memristor and Memristive Neural Networks*; James, A. P., Ed.; InTech, 2018. https://doi.org/10.5772/intechopen.69929.

(17) Ohno, T.; Hasegawa, T.; Tsuruoka, T.; Terabe, K.; Gimzewski, J. K.; Aono, M. Short-Term Plasticity and Long-Term Potentiation Mimicked in Single Inorganic Synapses. *Nat. Mater.* **2011**, *10* (8), 591–595. https://doi.org/10.1038/nmat3054.
(18) Mansuy, I. M.; Mayford, M.; Jacob, B.; Kandel, E. R.; Bach, M. E. Restricted and Regulated Overexpression Reveals Calcineurin as a Key Component in the Transition from Short-Term to Long-Term Memory. *Cell* **1998**, *92* (1), 39–49. https://doi.org/10.1016/S0092-8674(00)80897-1.
(19) James, C.; Morand, S.; Barcellona-Lehmann, S.; Michel, C. M.; Schnider, A. Neural Transition from Short- to Long-Term Memory and the Medial Temporal Lobe: A Human Evoked-Potential Study. *Hippocampus* **2009**, *19* (4), 371–378. https://doi.org/10.1002/hipo.20526.
(20) Kim, M.-K.; Park, Y.; Kim, I.-J.; Lee, J.-S. Emerging Materials for Neuromorphic Devices and Systems. *iScience* **2020**, *23* (12), 101846. https://doi.org/10.1016/j.isci.2020.101846.
(21) Bear, M. F.; Cooper, L. N.; Ebner, F. F. A Physiological Basis for a Theory of Synapse Modification. *Science* **1987**, *237* (4810), 42–48. https://doi.org/10.1126/science.3037696.
(22) Caporale, N.; Dan, Y. Spike Timing–Dependent Plasticity: A Hebbian Learning Rule. *Annu. Rev. Neurosci.* **2008**, *31* (1), 25–46. https://doi.org/10.1146/annurev.neuro.31.060407.125639.
(23) Rachmuth, G.; Shouval, H. Z.; Bear, M. F.; Poon, C.-S. A Biophysically-Based Neuromorphic Model of Spike Rate- and Timing-Dependent Plasticity. *Proc. Natl. Acad. Sci.* **2011**, *108* (49), E1266–E1274. https://doi.org/10.1073/pnas.1106161108.
(24) Ling, H.; Koutsouras, D. A.; Kazemzadeh, S.; van de Burgt, Y.; Yan, F.; Gkoupidenis, P. Electrolyte-Gated Transistors for Synaptic Electronics, Neuromorphic Computing, and Adaptable Biointerfacing. *Appl. Phys. Rev.* **2020**, *7* (1), 011307. https://doi.org/10.1063/1.5122249.
(25) Hopfield, J. J. Neural Networks and Physical Systems with Emergent Collective Computational Abilities. *Proc. Natl. Acad. Sci.* **1982**, *79* (8), 2554–2558. https://doi.org/10.1073/pnas.79.8.2554.
(26) Mohseni-Dargah, M.; Falahati, Z.; Dabirmanesh, B.; Nasrollahi, P.; Khajeh, K. Chapter 12 - Machine Learning in Surface Plasmon Resonance for Environmental Monitoring. In *Artificial Intelligence and Data Science in Environmental Sensing*; Asadnia, M., Razmjou, A., Beheshti, A., Eds.; Cognitive Data Science in Sustainable Computing; Academic Press, 2022; pp 269–298. https://doi.org/10.1016/B978-0-323-90508-4.00012-5.
(27) Chakma, G.; Adnan, M. M.; Wyer, A. R.; Weiss, R.; Schuman, C. D.; Rose, G. S. Memristive Mixed-Signal Neuromorphic Systems: Energy-Efficient Learning at the Circuit-Level. *IEEE J. Emerg. Sel. Top. Circuits Syst.* **2018**, *8* (1), 125–136. https://doi.org/10.1109/JETCAS.2017.2777181.
(28) Minsky, M. L. *"Neural Nets and the Brain Model Problem " Ph.D. Dissertation, Princeton Univ., Princeton, N. J., 1954. (University Microfilms, Ann Arbor.)*.
(29) Maher, M. A. C.; Deweerth, S. P.; Mahowald, M. A.; Mead, C. A. Implementing Neural Architectures Using Analog VLSI Circuits. *IEEE Trans. Circuits Syst.* **1989**, *36* (5), 643–652. https://doi.org/10.1109/31.31311.
(30) Indiveri, G.; Chicca, E.; Douglas, R. A VLSI Array of Low-Power Spiking Neurons and Bistable Synapses with Spike-Timing Dependent Plasticity. *IEEE Trans. Neural Netw.* **2006**, *17* (1), 211–221. https://doi.org/10.1109/TNN.2005.860850.
(31) Chicca, E.; Badoni, D.; Dante, V.; D'Andreagiovanni, M.; Salina, G.; Carota, L.; Fusi, S.; Del Giudice, P. A VLSI Recurrent Network of Integrate-and-Fire Neurons Connected by Plastic Synapses with Long-Term Memory. *IEEE Trans. Neural Netw.* **2003**, *14* (5), 1297–1307. https://doi.org/10.1109/TNN.2003.816367.

(32) Roy, K.; Jaiswal, A.; Panda, P. Towards Spike-Based Machine Intelligence with Neuromorphic Computing. *Nature* **2019**, *575* (7784), 607–617. https://doi.org/10.1038/s41586-019-1677-2.
(33) Davies, M.; Srinivasa, N.; Lin, T.-H.; Chinya, G.; Joshi, P.; Lines, A.; Wild, A.; Wang, H.; Mathaikutty, D. Loihi: A Neuromorphic Manycore Processor with On-Chip Learning. *IEEE Micro* **2018**, *PP*, 1–1. https://doi.org/10.1109/MM.2018.112130359.
(34) Benjamin, B. V.; Gao, P.; McQuinn, E.; Choudhary, S.; Chandrasekaran, A. R.; Bussat, J.-M.; Alvarez-Icaza, R.; Arthur, J. V.; Merolla, P. A.; Boahen, K. Neurogrid: A Mixed-Analog-Digital Multichip System for Large-Scale Neural Simulations. *Proc. IEEE* **2014**, *102* (5), 699–716. https://doi.org/10.1109/JPROC.2014.2313565.
(35) Schmitt, S.; Klähn, J.; Bellec, G.; Grübl, A.; Güttler, M.; Hartel, A.; Hartmann, S.; Husmann, D.; Husmann, K.; Jeltsch, S.; Karasenko, V.; Kleider, M.; Koke, C.; Kononov, A.; Mauch, C.; Müller, E.; Müller, P.; Partzsch, J.; Petrovici, M. A.; Schiefer, S.; Scholze, S.; Thanasoulis, V.; Vogginger, B.; Legenstein, R.; Maass, W.; Mayr, C.; Schüffny, R.; Schemmel, J.; Meier, K. Neuromorphic Hardware in the Loop: Training a Deep Spiking Network on the BrainScaleS Wafer-Scale System. In *2017 International Joint Conference on Neural Networks (IJCNN)*; 2017; pp 2227–2234. https://doi.org/10.1109/IJCNN.2017.7966125.
(36) Khan, M. M.; Lester, D.; Plana, L.; Rast, A. D.; Jin, X.; Painkras, E.; Furber, S. SpiNNaker: Mapping Neural Networks onto a Massively-Parallel Chip Multiprocessor. *2008 IEEE Int. Jt. Conf. Neural Netw. IEEE World Congr. Comput. Intell.* **2008**. https://doi.org/10.1109/IJCNN.2008.4634199.
(37) Pedretti, G.; Milo, V.; Ambrogio, S.; Carboni, R.; Bianchi, S.; Calderoni, A.; Ramaswamy, N.; Spinelli, A. S.; Ielmini, D. Memristive Neural Network for On-Line Learning and Tracking with Brain-Inspired Spike Timing Dependent Plasticity. *Sci. Rep.* **2017**, *7* (1), 5288. https://doi.org/10.1038/s41598-017-05480-0.
(38) Voglis, G.; Tavernarakis, N. The Role of Synaptic Ion Channels in Synaptic Plasticity. *EMBO Rep.* **2006**, *7* (11), 1104–1110. https://doi.org/10.1038/sj.embor.7400830.
(39) Perea, G.; Navarrete, M.; Araque, A. Tripartite Synapses: Astrocytes Process and Control Synaptic Information. *Trends Neurosci.* **2009**, *32* (8), 421–431. https://doi.org/10.1016/j.tins.2009.05.001.
(40) Poon, C.-S.; Zhou, K. Neuromorphic Silicon Neurons and Large-Scale Neural Networks: Challenges and Opportunities. *Front. Neurosci.* **2011**, *5*, 108. https://doi.org/10.3389/fnins.2011.00108.
(41) Roosta, S. H. *Parallel Processing and Parallel Algorithms: Theory and Computation*; Springer Science & Business Media, 2012.
(42) Ielmini, D.; Wong, H.-S. P. In-Memory Computing with Resistive Switching Devices. *Nat. Electron.* **2018**, *1* (6), 333–343. https://doi.org/10.1038/s41928-018-0092-2.
(43) Ielmini, D.; Ambrogio, S. Emerging Neuromorphic Devices. *Nanotechnology* **2019**, *31* (9), 092001. https://doi.org/10.1088/1361-6528/ab554b.
(44) Burr, G. W.; Shelby, R. M.; di Nolfo, C.; Jang, J. W.; Shenoy, R. S.; Narayanan, P.; Virwani, K.; Giacometti, E. U.; Kurdi, B.; Hwang, H. Experimental Demonstration and Tolerancing of a Large-Scale Neural Network (165,000 Synapses), Using Phase-Change Memory as the Synaptic Weight Element. In *2014 IEEE International Electron Devices Meeting*; 2014; p 29.5.1-29.5.4. https://doi.org/10.1109/IEDM.2014.7047135.
(45) Wang, Z.; Wang, L.; Nagai, M.; Xie, L.; Yi, M.; Huang, W. Nanoionics-Enabled Memristive Devices: Strategies and Materials for Neuromorphic Applications. *Adv. Electron. Mater.* **2017**, *3* (7), 1600510. https://doi.org/10.1002/aelm.201600510.

(46) Ielmini, D. Resistive Switching Memories Based on Metal Oxides: Mechanisms, Reliability and Scaling. *Semicond. Sci. Technol.* **2016**, *31*, 063002. https://doi.org/10.1088/0268-1242/31/6/063002.
(47) Jo, S. H.; Chang, T.; Ebong, I.; Bhadviya, B. B.; Mazumder, P.; Lu, W. Nanoscale Memristor Device as Synapse in Neuromorphic Systems. *Nano Lett.* **2010**, *10* (4), 1297–1301. https://doi.org/10.1021/nl904092h.
(48) Prezioso, M.; Merrikh-Bayat, F.; Hoskins, B. D.; Adam, G. C.; Likharev, K. K.; Strukov, D. B. Training and Operation of an Integrated Neuromorphic Network Based on Metal-Oxide Memristors. *Nature* **2015**, *521* (7550), 61–64. https://doi.org/10.1038/nature14441.
(49) Alibart, F.; Zamanidoost, E.; Strukov, D. B. Pattern Classification by Memristive Crossbar Circuits Using Ex Situ and in Situ Training. *Nat. Commun.* **2013**, *4* (1), 2072. https://doi.org/10.1038/ncomms3072.
(50) Zhu, J.; Zhang, T.; Yang, Y.; Huang, R. A Comprehensive Review on Emerging Artificial Neuromorphic Devices. *Appl. Phys. Rev.* **2020**, *7* (1), 011312. https://doi.org/10.1063/1.5118217.
(51) Beilliard, Y.; Alibart, F. Multi-Terminal Memristive Devices Enabling Tunable Synaptic Plasticity in Neuromorphic Hardware: A Mini-Review. *Front. Nanotechnol.* **2021**, *3*.
(52) Chistiakova, M.; Bannon, N. M.; Bazhenov, M.; Volgushev, M. Heterosynaptic Plasticity: Multiple Mechanisms and Multiple Roles. *Neurosci. Rev. J. Bringing Neurobiol. Neurol. Psychiatry* **2014**, *20* (5), 483–498. https://doi.org/10.1177/1073858414529829.
(53) van de Burgt, Y.; Melianas, A.; Keene, S. T.; Malliaras, G.; Salleo, A. Organic Electronics for Neuromorphic Computing. *Nat. Electron.* **2018**, *1* (7), 386–397. https://doi.org/10.1038/s41928-018-0103-3.
(54) Fuller, E. J.; Gabaly, F. E.; Léonard, F.; Agarwal, S.; Plimpton, S. J.; Jacobs-Gedrim, R. B.; James, C. D.; Marinella, M. J.; Talin, A. A. Li-Ion Synaptic Transistor for Low Power Analog Computing. *Adv. Mater.* **2017**, *29* (4), 1604310. https://doi.org/10.1002/adma.201604310.
(55) van de Burgt, Y.; Lubberman, E.; Fuller, E. J.; Keene, S. T.; Faria, G. C.; Agarwal, S.; Marinella, M. J.; Alec Talin, A.; Salleo, A. A Non-Volatile Organic Electrochemical Device as a Low-Voltage Artificial Synapse for Neuromorphic Computing. *Nat. Mater.* **2017**, *16* (4), 414–418. https://doi.org/10.1038/nmat4856.
(56) Jerry, M.; Dutta, S.; Kazemi, A.; Ni, K.; Zhang, J.; Chen, P.-Y.; Sharma, P.; Yu, S.; Hu, X. S.; Niemier, M.; Datta, S. A Ferroelectric Field Effect Transistor Based Synaptic Weight Cell. *J. Phys. Appl. Phys.* **2018**, *51* (43), 434001. https://doi.org/10.1088/1361-6463/aad6f8.
(57) Gkoupidenis, P.; Schaefer, N.; Garlan, B.; Malliaras, G. G. Neuromorphic Functions in PEDOT:PSS Organic Electrochemical Transistors. *Adv. Mater.* **2015**, *27* (44), 7176–7180. https://doi.org/10.1002/adma.201503674.
(58) Fu, Y.; Kong, L.-A.; Chen, Y.; Wang, J.; Qian, C.; Yuan, Y.; Sun, J.; Gao, Y.; Wan, Q. Flexible Neuromorphic Architectures Based on Self-Supported Multiterminal Organic Transistors. *ACS Appl. Mater. Interfaces* **2018**, *10* (31), 26443–26450. https://doi.org/10.1021/acsami.8b07443.
(59) Rivnay, J.; Inal, S.; Salleo, A.; Owens, R. M.; Berggren, M.; Malliaras, G. G. Organic Electrochemical Transistors. *Nat. Rev. Mater.* **2018**, *3* (2), 1–14. https://doi.org/10.1038/natrevmats.2017.86.
(60) Bernards, D. A.; Malliaras, G. G. Steady-State and Transient Behavior of Organic Electrochemical Transistors. *Adv. Funct. Mater.* **2007**, *17* (17), 3538–3544. https://doi.org/10.1002/adfm.200601239.

(61) Seminario, J. M.; Cordova, L. E. Toward Multiple-Valued Configurable Random Molecular Logic Units. In *Proceedings of the 2001 1st IEEE Conference on Nanotechnology. IEEE-NANO 2001 (Cat. No.01EX516)*; 2001; pp 146–150. https://doi.org/10.1109/NANO.2001.966409.
(62) Seminario, J. M.; Zacarias, A. G.; Derosa, P. A. Analysis of a Dinitro-Based Molecular Device. *J. Chem. Phys.* **2002**, *116* (4), 1671–1683. https://doi.org/10.1063/1.1429236.
(63) Seminario, J. M.; Cordova, L. E.; Derosa, P. A. An Ab Initio Approach to the Calculation of Current-Voltage Characteristics of Programmable Molecular Devices. *Proc. IEEE* **2003**, *91* (11), 1958–1975. https://doi.org/10.1109/JPROC.2003.818328.
(64) Seminario, J. M.; Ma, Y.; Tarigopula, V. The Nanocell: A Chemically Assembled Molecular Electronic Circuit. *IEEE Sens. J.* **2006**, *6* (6), 1614–1626. https://doi.org/10.1109/JSEN.2006.884163.
(65) Tour, J. M.; Cheng, L.; Nackashi, D. P.; Yao, Y.; Flatt, A. K.; St. Angelo, S. K.; Mallouk, T. E.; Franzon, P. D. NanoCell Electronic Memories. *J. Am. Chem. Soc.* **2003**, *125* (43), 13279–13283. https://doi.org/10.1021/ja036369g.
(66) Mishra, R.; Sharma, A.; Tandon, P. *Conducting Polymers—Modern Semiconductors: A Theoretical Overview*; 2011.
(67) 1 Chapter 16 Conjugation, Resonance, and Dienes. 2 Conjugation occurs whenever p orbitals can overlap on three or more adjacent atoms Conjugation. - ppt download. https://slideplayer.com/slide/7880533/ (accessed 2022-09-06).
(68) *Pericyclic reactions*. https://www.stereoelectronics.org/webPR/PR_01.html (accessed 2022-09-06).
(69) Li, G.; Chang, W.-H.; Yang, Y. Low-Bandgap Conjugated Polymers Enabling Solution-Processable Tandem Solar Cells. *Nat. Rev. Mater.* **2017**, *2* (8), 1–13. https://doi.org/10.1038/natrevmats.2017.43.
(70) Le, T.-H.; Kim, Y.; Yoon, H. Electrical and Electrochemical Properties of Conducting Polymers. *Polymers* **2017**, *9* (4), 150. https://doi.org/10.3390/polym9040150.
(71) Brédas, J. L.; Calbert, J. P.; da Silva Filho, D. A.; Cornil, J. Organic Semiconductors: A Theoretical Characterization of the Basic Parameters Governing Charge Transport. *Proc. Natl. Acad. Sci.* **2002**, *99* (9), 5804–5809. https://doi.org/10.1073/pnas.092143399.
(72) Paulsen, B.; Tybrandt, K.; Stavrinidou, E.; Rivnay, J. Organic Mixed Ionic–Electronic Conductors. *Nat. Mater.* **2019**, *19*, 1–14. https://doi.org/10.1038/s41563-019-0435-z.
(73) Song, I.; Yeon Park, N.; Seung Jeong, G.; Hwan Kang, J.; Hwa Seo, J.; Choi, J.-Y. Conductive Channel Formation for Enhanced Electrical Conductivity of PEDOT:PSS with High Work-Function. *Appl. Surf. Sci.* **2020**, *529*, 147176. https://doi.org/10.1016/j.apsusc.2020.147176.
(74) Volkov, A. V.; Wijeratne, K.; Mitraka, E.; Ail, U.; Zhao, D.; Tybrandt, K.; Andreasen, J. W.; Berggren, M.; Crispin, X.; Zozoulenko, I. V. Understanding the Capacitance of PEDOT:PSS. *Adv. Funct. Mater.* **2017**, *27* (28), 1700329. https://doi.org/10.1002/adfm.201700329.
(75) Bubnova, O.; Khan, Z. U.; Wang, H.; Braun, S.; Evans, D. R.; Fabretto, M.; Hojati-Talemi, P.; Dagnelund, D.; Arlin, J.-B.; Geerts, Y. H.; Desbief, S.; Breiby, D. W.; Andreasen, J. W.; Lazzaroni, R.; Chen, W. M.; Zozoulenko, I.; Fahlman, M.; Murphy, P. J.; Berggren, M.; Crispin, X. Semi-Metallic Polymers. *Nat. Mater.* **2014**, *13* (2), 190–194. https://doi.org/10.1038/nmat3824.
(76) Nardes, A. M.; Kemerink, M.; Janssen, R. A. J. Anisotropic Hopping Conduction in Spin-Coated PEDOT:PSS Thin Films. *Phys. Rev. B* **2007**, *76* (8), 085208. https://doi.org/10.1103/PhysRevB.76.085208.

(77) Lang, U.; Müller, E.; Naujoks, N.; Dual, J. Microscopical Investigations of PEDOT:PSS Thin Films. *Adv. Funct. Mater.* **2009**, *19* (8), 1215–1220. https://doi.org/10.1002/adfm.200801258.
(78) Lee, Y.-Y.; Choi, G. M.; Lim, S.-M.; Cho, J.-Y.; Choi, I.-S.; Nam, K. T.; Joo, Y.-C. Growth Mechanism of Strain-Dependent Morphological Change in PEDOT:PSS Films. *Sci. Rep.* **2016**, *6* (1), 25332. https://doi.org/10.1038/srep25332.
(79) Romele, P.; Ghittorelli, M.; Kovács-Vajna, Z. M.; Torricelli, F. Ion Buffering and Interface Charge Enable High Performance Electronics with Organic Electrochemical Transistors. *Nat. Commun.* **2019**, *10* (1), 3044. https://doi.org/10.1038/s41467-019-11073-4.
(80) Rebetez, G.; Bardagot, O.; Affolter, J.; Réhault, J.; Banerji, N. What Drives the Kinetics and Doping Level in the Electrochemical Reactions of PEDOT:PSS? *Adv. Funct. Mater.* **2022**, *32* (5), 2105821. https://doi.org/10.1002/adfm.202105821.
(81) Decataldo, F.; Gualandi, I.; Tessarolo, M.; Scavetta, E.; Fraboni, B. Transient-Doped Organic Electrochemical Transistors Working in Current-Enhancing Mode as Sensing Devices for Low Concentration of Oxygen Dissolved in Solution. *APL Mater.* **2020**, *8* (9), 091103. https://doi.org/10.1063/5.0015232.
(82) Zhang, X.; Yang, W.; Zhang, H.; Xie, M.; Duan, X. PEDOT:PSS: From Conductive Polymers to Sensors. *Nanotechnol. Precis. Eng.* **2021**, *4* (4), 045004. https://doi.org/10.1063/10.0006866.
(83) Smela, E. Conjugated Polymer Actuators for Biomedical Applications. *Adv. Mater.* **2003**, *15* (6), 481–494. https://doi.org/10.1002/adma.200390113.
(84) Jang, J.; Ha, J.; Cho, J. Fabrication of Water-Dispersible Polyaniline-Poly(4- Styrenesulfonate) Nanoparticles For Inkjet-Printed Chemical-Sensor Applications. *Adv. Mater.* **2007**, *19* (13), 1772–1775. https://doi.org/10.1002/adma.200602127.
(85) Pei, Q.; Yu, G.; Zhang, C.; Yang, Y.; Heeger, A. J. Polymer Light-Emitting Electrochemical Cells. *Science* **1995**, *269* (5227), 1086–1088. https://doi.org/10.1126/science.269.5227.1086.
(86) Isaksson, J.; Kjäll, P.; Nilsson, D.; Robinson, N.; Berggren, M.; Richter-Dahlfors, A. Electronic Control of Ca2+ Signalling in Neuronal Cells Using an Organic Electronic Ion Pump. *Nat. Mater.* **2007**, *6* (9), 673–679. https://doi.org/10.1038/nmat1963.
(87) Pecqueur, S.; Vuillaume, D.; Alibart, F. Perspective: Organic Electronic Materials and Devices for Neuromorphic Engineering. *J. Appl. Phys.* **2018**, *124* (15), 151902. https://doi.org/10.1063/1.5042419.
(88) Jiang, H.; Wu, W.; Chang, Z.; Zeng, H.; Liang, R.; Zhang, W.; Zhang, W.; Wu, G.; Li, Z.; Wang, H. In Situ Polymerization of PEDOT:PSS Films Based on EMI-TFSI and the Analysis of Electrochromic Performance. *E-Polym.* **2021**, *21* (1), 722–733. https://doi.org/10.1515/epoly-2021-0073.
(89) Yuan, C.; Guo, S.; Wang, S.; Liu, L.; Chen, W.; Wang, E. Electropolymerization Polyoxometalate (POM)-Doped PEDOT Film Electrodes with Mastoid Microstructure and Its Application in Dye-Sensitized Solar Cells (DSSCs). *Ind. Eng. Chem. Res.* **2013**, *52* (20), 6694–6703. https://doi.org/10.1021/ie302845z.
(90) Benoudjit, A.; Bader, M. M.; Wan Salim, W. W. A. Study of Electropolymerized PEDOT:PSS Transducers for Application as Electrochemical Sensors in Aqueous Media. *Sens. Bio-Sens. Res.* **2018**, *17*, 18–24. https://doi.org/10.1016/j.sbsr.2018.01.001.
(91) Ghazal, M.; Daher Mansour, M.; Scholaert, C.; Dargent, T.; Coffinier, Y.; Pecqueur, S.; Alibart, F. Bio-Inspired Adaptive Sensing through Electropolymerization of Organic Electrochemical Transistors. *Adv. Electron. Mater.* **2022**, *8* (3), 2100891. https://doi.org/10.1002/aelm.202100891.

(92) Wustoni, S.; Hidalgo, T. C.; Hama, A.; Ohayon, D.; Savva, A.; Wei, N.; Wehbe, N.; Inal, S. In Situ Electrochemical Synthesis of a Conducting Polymer Composite for Multimetabolite Sensing. *Adv. Mater. Technol.* **2020**, *5* (3), 1900943. https://doi.org/10.1002/admt.201900943.
(93) Murbach, J. M.; Currlin, S.; Widener, A.; Tong, Y.; Chhatre, S.; Subramanian, V.; Martin, D. C.; Johnson, B. N.; Otto, K. J. In Situ Electrochemical Polymerization of Poly(3,4-Ethylenedioxythiophene) (PEDOT) for Peripheral Nerve Interfaces. *MRS Commun.* **2018**, *8* (3), 1043–1049. https://doi.org/10.1557/mrc.2018.138.
(94) Sessolo, M.; Khodagholy, D.; Rivnay, J.; Maddalena, F.; Gleyzes, M.; Steidl, E.; Buisson, B.; Malliaras, G. G. Easy-to-Fabricate Conducting Polymer Microelectrode Arrays. *Adv. Mater.* **2013**, *25* (15), 2135–2139. https://doi.org/10.1002/adma.201204322.
(95) Ciccone, G.; Cucchi, M.; Gao, Y.; Kumar, A.; Seifert, L. M.; Weissbach, A.; Tseng, H.; Kleemann, H.; Alibart, F.; Leo, K. Growth and Design Strategies of Organic Dendritic Networks. *Discov. Mater.* **2022**, *2* (1), 7. https://doi.org/10.1007/s43939-022-00028-0.
(96) Pecqueur, S.; Mastropasqua Talamo, M.; Guérin, D.; Blanchard, P.; Roncali, J.; Vuillaume, D.; Alibart, F. Neuromorphic Time-Dependent Pattern Classification with Organic Electrochemical Transistor Arrays. *Adv. Electron. Mater.* **2018**, *4* (9), 1800166. https://doi.org/10.1002/aelm.201800166.
(97) Gerasimov, J. Y.; Gabrielsson, R.; Forchheimer, R.; Stavrinidou, E.; Simon, D. T.; Berggren, M.; Fabiano, S. An Evolvable Organic Electrochemical Transistor for Neuromorphic Applications. *Adv. Sci.* **2019**, *6* (7), 1801339. https://doi.org/10.1002/advs.201801339.
(98) Gerasimov, J. Y.; Zhao, D.; Sultana, A.; Abrahamsson, T.; Han, S.; Bliman, D.; Tu, D.; Simon, D. T.; Olsson, R.; Crispin, X.; Berggren, M.; Fabiano, S. A Biomimetic Evolvable Organic Electrochemical Transistor. *Adv. Electron. Mater.* **2021**, *7* (11), 2001126. https://doi.org/10.1002/aelm.202001126.
(99) Koizumi, Y.; Shida, N.; Ohira, M.; Nishiyama, H.; Tomita, I.; Inagi, S. Electropolymerization on Wireless Electrodes towards Conducting Polymer Microfibre Networks. *Nat. Commun.* **2016**, *7* (1), 10404. https://doi.org/10.1038/ncomms10404.
(100) Watanabe, T.; Ohira, M.; Koizumi, Y.; Nishiyama, H.; Tomita, I.; Inagi, S. In-Plane Growth of Poly(3,4-Ethylenedioxythiophene) Films on a Substrate Surface by Bipolar Electropolymerization. *ACS Macro Lett.* **2018**, *7* (5), 551–555. https://doi.org/10.1021/acsmacrolett.8b00170.
(101) Ohira, M.; Koizumi, Y.; Nishiyama, H.; Tomita, I.; Inagi, S. Synthesis of Linear PEDOT Fibers by AC-Bipolar Electropolymerization in a Micro-Space. *Polym. J.* **2017**, *49* (1), 163–167. https://doi.org/10.1038/pj.2016.100.
(102) Koizumi, Y.; Ohira, M.; Watanabe, T.; Nishiyama, H.; Tomita, I.; Inagi, S. Synthesis of Poly(3,4-Ethylenedioxythiophene)–Platinum and Poly(3,4-Ethylenedioxythiophene)–Poly(Styrenesulfonate) Hybrid Fibers by Alternating Current Bipolar Electropolymerization. *Langmuir* **2018**, *34* (26), 7598–7603. https://doi.org/10.1021/acs.langmuir.8b00408.
(103) Inagi, S. Site-Selective Anisotropic Modification of Conductive Objects by Bipolar Electropolymerization. *Polym. J.* **2019**, *51* (10), 975–981. https://doi.org/10.1038/s41428-019-0223-2.
(104) Eickenscheidt, M.; Singler, E.; Stieglitz, T. Pulsed Electropolymerization of PEDOT Enabling Controlled Branching. *Polym. J.* **2019**, *51* (10), 1029–1036. https://doi.org/10.1038/s41428-019-0213-4.
(105) Dang, N. T. Study on Electro-Polymerization Wiring System Imitating Axonal Growth of Artificial Neurons towards Machine Learning; the 75th JSAP Autumn meeting, 2014, Japan.

(106) Akai-Kasaya, M.; Hagiwara, N.; Hikita, W.; Okada, M.; Sugito, Y.; Kuwahara, Y.; Asai, T. Evolving Conductive Polymer Neural Networks on Wetware. *Jpn. J. Appl. Phys.* **2020**, *59* (6), 060601. https://doi.org/10.35848/1347-4065/ab8e06.

(107) Hagiwara, N.; Sekizaki, S.; Kuwahara, Y.; Asai, T.; Akai-Kasaya, M. Long- and Short-Term Conductance Control of Artificial Polymer Wire Synapses. *Polymers* **2021**, *13* (2), 312. https://doi.org/10.3390/polym13020312.

(108) Cucchi, M.; Gruener, C.; Petrauskas, L.; Steiner, P.; Tseng, H.; Fischer, A.; Penkovsky, B.; Matthus, C.; Birkholz, P.; Kleemann, H.; Leo, K. Reservoir Computing with Biocompatible Organic Electrochemical Networks for Brain-Inspired Biosignal Classification. *Sci. Adv.* **2021**, *7* (34), eabh0693. https://doi.org/10.1126/sciadv.abh0693.

(109) Cucchi, M.; Kleemann, H.; Tseng, H.; Lee, A.; Leo, K. Structural Evolution and On-Demand Growth of Artificial Synapses via Field-Directed Polymerization. arXiv June 11, 2021. https://doi.org/10.48550/arXiv.2106.06191.

(110) Petrauskas, L.; Cucchi, M.; Grüner, C.; Ellinger, F.; Leo, K.; Matthus, C.; Kleemann, H. Nonlinear Behavior of Dendritic Polymer Networks for Reservoir Computing. *Adv. Electron. Mater.* **2022**, *8* (3), 2100330. https://doi.org/10.1002/aelm.202100330.

(111) Cucchi, M.; Kleemann, H.; Tseng, H.; Ciccone, G.; Lee, A.; Pohl, D.; Leo, K. Directed Growth of Dendritic Polymer Networks for Organic Electrochemical Transistors and Artificial Synapses. *Adv. Electron. Mater.* **2021**, *7* (10), 2100586. https://doi.org/10.1002/aelm.202100586.

(112) Ji, J.; Zhu, X.; Han, D.; Li, M.; Zhang, Q.; Shu, Y.; Cheng, Z.; Zhang, W.; Hua, E.; Sang, S. AC Electrodeposition of PEDOT Films in Protic Ionic Liquids for Long-Term Stable Organic Electrochemical Transistors. *Molecules* **2019**, *24* (22), 4105. https://doi.org/10.3390/molecules24224105.

(113) Ji, J.; Fu, Y.; Wang, J.; Chen, P.-Y.; Han, D.; Zhang, Q.; Zhang, W.; Sang, S.; Yang, X.; Cheng, Z. Bipolar Electrodeposition of Organic Electrochemical Transistor Arrays. *J. Mater. Chem. C* **2020**, *8* (33), 11499–11507. https://doi.org/10.1039/D0TC00436G.

Chapter 2. Investigation of artificial dendritic morphologies

Introduction

In this chapter, I will discuss objects that are aimed to mimic biological dendrites growth and morphology in neurons. These objects are realized as organic 3D polymer structures capable of replicating the shape of biological neurons. First, I will discuss the process of this artificial 3D polymer dendrites formation through method of AC-bipolar electropolymerization, the employed setup and conditions for the synthesis. Bearing in mind the possibility of changing the shape of the applied voltage pulse signal, the possibility of tuning the polymer morphology by changing the electrical parameters of the signal will be disclosed. For every single parameter variation, image and video analysis were carried out in order to better understand the dependency of applied electrical conditions on geometry of the obtained morphologies.

1. Context

As mentioned in the previous chapter, the human brain is a unique computing system where processes can be carried out in parallel at low power consumption. One of the features of this biological system is its bottom-up engineering, achieved through neurogenesis, which creates physical connections, determining optimal computing topologies or network self-healing. In particular, brain dendritic morphogenesis occurs on every neuron throughout the life of the learning system, and controls the growth of each neuron as the full functionality for the brain's long-term memory[1].
The diversity of dendritic forms in the brain can be classified into thirteen families of three groups of dendritic fields[2], where each family of dendritic arbors differs in the number of branches, number of segmentations per dendrites, and length and volume of different branches and segments[3]. Since dendrites' morphology contributes to the electrophysiological features that enable their signaling[4], the control of dendritic versatility is important to alter signal propagation, which in turn is related to the temporal characteristics of their memory properties. Therefore, to create a neuromorphic device capable of mimicking neurogenesis, this study is focused on investigating the possibility to generate neuron-like objects and modify their shape.

Earlier studies showed that by means of Alternating Current (AC)-bipolar electropolymerization, one can create such types of neuro-like objects in a bottom-up manner that replicate the shape of neural dendritic branches. Namely, this process was carried out through oxidation of 3,4-ethylenedioxythiophene (EDOT) into millimeter-scaled PEDOT dendritic forms in the presence of 1,4-benzoquinone (BQ) (as a supportive reagent)[5,6,7,8,9.]
Such conductive bridging of polarizable nodes in a common electrolyte is an attractive approach for bottom-up generated devices because of: local activation (individual programming), dependency on electric field's direction (layer-to-layer interconnection parallelism), on field's magnitude (spatial convolution), and voltage non-linearity for electro- activated polymerizations (neural rectification).

Inspired by these aforementioned works, this strategy of AC electropolymerization was also applied in this study to generate evolvable dendritic polymer structures. Nevertheless, unlike in previous works, not bipolar electrodes were employed, but the technique was examined on free- standing gold wires electrically polarized in a water-based electrolyte environment. This configuration gives an opportunity to mature polymer fibers in 3D way as tree-like branches without utilizing any substrate with predefined patterns, which eventually leads to fibers propagation in an arbitrary manner controlled mainly by electric field distribution.

2. Setup representation

Setup for dendrites generation was realized with two gold (Au) wires, which served as electrodes and were immersed in a drop of aqueous electrolyte of 20 µL volume. They were lifted up at one height from the substrate (one full turn of the upper probe's wheel) and placed at a distance of L=240 µm from each other (**Figure 1**). The aqueous electrolyte for electropolymerization contained 10 mM of EDOT monomer, 1 mM of NaPSS as a supporting salt, and 10 mM of BQ as a sacrificial reagent. The presence of BQ is necessary to stabilize the pH of the electrolyte by consuming all the protons (hydrogen) formed during EDOT oxidation. Each time one EDOT molecule oxidizes, one BQ molecule reduces into hydroquinone (HQ) to support the electrolyte balance by generating two electrons and consuming both protons produced during oxidation of one EDOT molecule. In the experiments carried out for this thesis, EDOT and BQ were always introduced equimolarly in the aqueous electrolyte solution. NaPSS was chosen both as a supporting electrolyte and a doping counter- anion to support PEDOT dendrite in a highly doped state (charged PEDOT is stable in air in standard conditions and can reach conductivity up to 1 kS/cm)[10]. Polymer growth was performed by applying bipolar voltage pulses to a signal electrode while the counter one was set as ground. Due to utilization of a pulsed waveform, one can modify the shape of applied pulses by changing at least one electrical parameter, such as peak to peak voltage (V_{pp}), frequency (f), duty cycle (dc) and offset voltage (V_{off},). V_{pp} is described as the difference between the highest and the lowest voltage values in a waveform. Peak voltage (V_p) is the highest voltage value compared to zero volts. In the context of AC applications, the peak- to- peak value (V_{pp}) will be twice as high as the peak value (V_p). The duty cycle (dc) represents the ratio of pulse width (dc*T) over the whole period duration (T) in percentage, and voltage offset (V_{off}) represents the mean amplitude displacement of a signal from the zero line (here the ground).

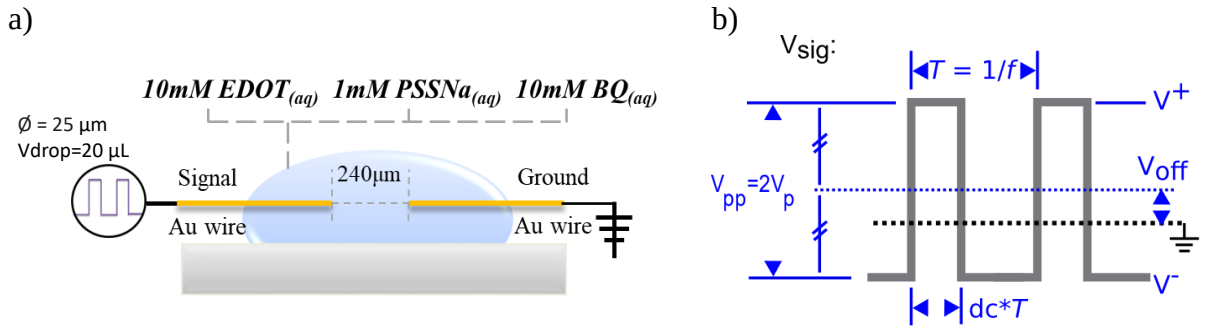

Figure 1. a) Experimental setup for PEDOT:PSS dendrites' growth consisting of two free-standing gold (Au) wires of 25 µm diameter, immersed into a drop of electrolyte (V_{drop} = 20 µL) and placed at the same height and at a distance of L = 240 µm from each other. Polarization occurred under square waveform voltage on the signal wire, while the other wire was grounded. The electrolyte solution included 10 mM of EDOT, 10 mM of BQ and 1 mM of NaPSS. b) Applied square waveform signals with controllable voltage amplitude (V_{pp}), frequency (f), duty cycle (dc) and offset voltage (V_{off}) [11].

Figure 1b depicts bipolar square pulses utilized in this study, in which positive (V^+) and negative (V^-) polarities are presented. The magnitude of V^+ and V^- is defined not only by V_p (or V_{pp}) value but can also be modified through V_{off} variation: $V^+ = V_{off} + V_p$, $V^- = V_{off} - V_p$. V^+ defines the signal's anodic polarization that occurs for each period $T = 1/f$ in the time frame between 0 (start of the cycle) and dc*T (where dc is the duty cycle). V^-, the signal's cathodic polarization, takes place as well each period T but in the temporal frame between dc*T and T (the end of the period).
Utilizing the possibility to modify the shape of the applied square waveform, the main goal in this section of the thesis is to determine the impact of each electrical parameter on tuning the polymer geometry.

3. Mechanism of electropolymerization.

The setup in this work does not involve a potentiostat that aims to keep the potential of a working electrode at a constant level with respect to a third reference electrode[12]. Hence, the voltage drop in the system is not potentiostated at one particular wire. Namely, the voltage drops from the applied voltage on one wire's bulk (V_{sig}) to its surface V'_{sig} in the electrolyte, drops through the electrolyte according to its resistivity to V'_{gnd} at the grounded- electrode/electrolyte interface, which electrode's bulk is grounded ($V_{gnd} = 0 \neq V'_{gnd}$), as shown in orange and purple in **Figure 3.** Considering the presence of Faradaic processes at both wire/electrolyte interfaces of both electrodes, the dynamics of electropolymerization will obey an idealized equivalent circuit shown in **Figure 2** (it is performed under the condition of no mass transfer limiting the electrochemical impedance)[13]. According to this model, the electrolytic conductance $G_{Na+PSS-}$ takes into account drift currents created by both Na^+ and PSS^- ions. Both types of ions accumulate at electrodes' interfaces of the opposite polarity and form a double-layer consisting of PSS^- at the cathode (from which C_{PSS-} capacitance is originated) and Na^+ double-layer at the anode (resulting into C_{Na+} capacitance). Permeability of both double layers for neutral solutes depends on their packing that is eventually modulating the Faradaic processes of EDOT oxidation (resistance R_{ox}) and BQ reduction (R_{red}). Periodically, these processes are switched between both signal and grounded electrodes. Associating ionic charge/discharge with ohmic resistors/dielectric capacitors relaxations, surface potentials' dynamics at signal (V'_{sig}) and ground electrode (V'_{gnd}) can be depicted as in **Figure 3**.

Therefore during growth time, the electric field between two wires will change according to: $E = (V'_{sig} - V'_{gnd})/d$ (where L=240µm and $d < L$ is shortest distance between two dendrites).

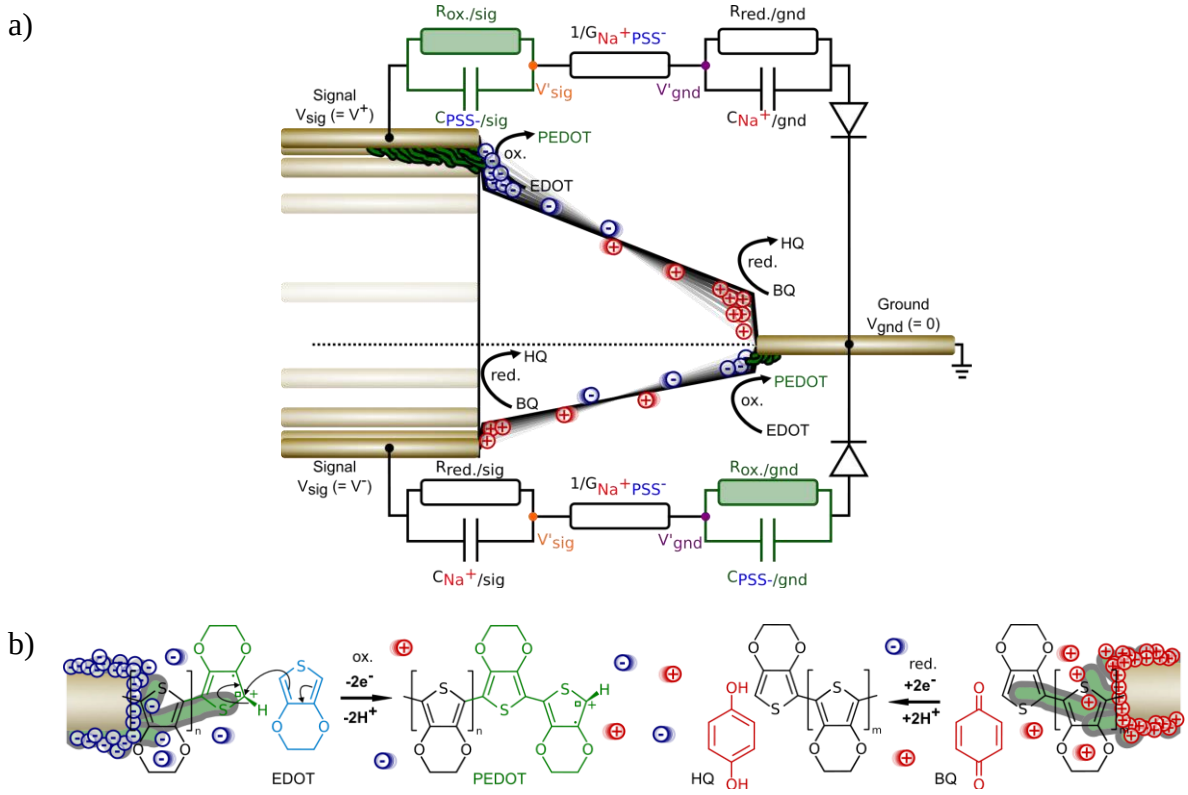

Figure 2. a) Generic equivalent circuit of the electrochemical system, depicting the dynamics of the bias voltage across the gold wires, that yields to various potential dependent kinetics for the ion drifts thanks to the different RC circuit elements involved in the electrochemical system. *G* electrolytic conductance, capacitance of double layer created either by Na^+ or by PSS^-. b) Faradaic (redox) and Non-Faradaic (capacitive) processes occurring at both anodic and cathodic dendritic electrodes upon V_{sig} polarization[11].

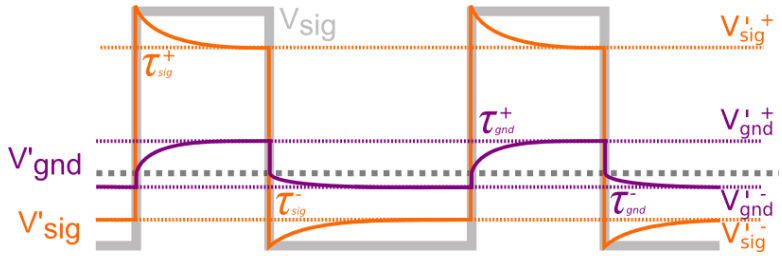

Figure 3. Voltage diagram displaying the ion dynamics, inducing a time-dependent voltage-drop across the electrolyte that results in different growth modes for the electropolymerized PEDOT dendrites[11].

According to the results of Cyclic Voltammetry (CV) performed individually for every single component of the electrolytic system (E_{ox} = 0.816 V for EDOT and E_{red} = 0.105 V vs Ag/AgCl in 1 M $KCl_{(aq)}$), the minimum ΔV_{min} required to electropolymerize EDOT in the presence of BQ under quasi-steady conditions is 0.921 V (**Figure 4**- 50 mV/s). Additionally, CV exhibits that

NaPSS is not electrochemically active, implying exclusive participation of BQ reduction as the counter-reaction for dendritic electropolymerization, without any redox-active contribution of PSS^- ions. Nevertheless, PSS presence may affect the redox products' stability as both a surfactant and a doping-supporting anion.

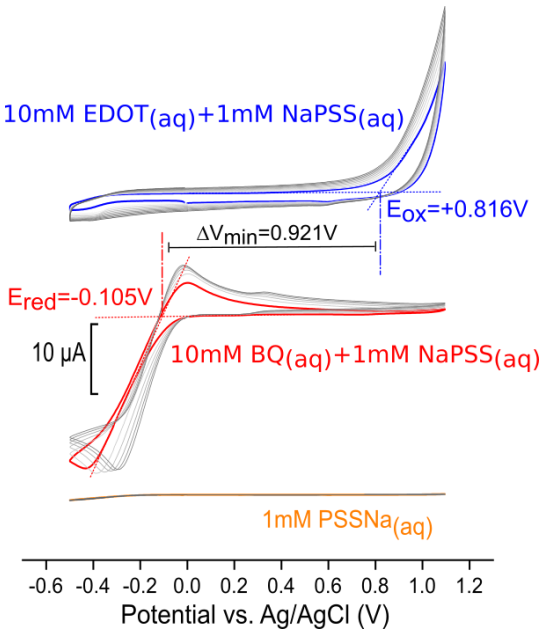

Figure 4. Cyclic Voltammetry curves conducted on a two Au wire electrochemical setup separately for EDOT (blue line), BQ (red line) aqueous solutions in the presence of PSSNa and individually for PSSNa (orange line) [11].

4. Morphological influence with the peak voltage amplitude.

To verify the influence of the voltage amplitude, experiments were carried out by varying V_p values at fixed frequency, offset, and duty cycle parameters (f = 80 Hz, V_{off} = 0 V, dc = 50%). Dendritic growth was carried out in the amplitude range indicated below, where voltage was applied with a step of 0.5 V. In the range of verified voltage values the electropolymerization occurred in the amplitude window from 3.5 V to 6.5 V. At these conditions, V_p values lower or equal to 3.0 V did not lead to any visible polymer maturing on the edges of electrodes, whereas V_p higher or equal to 7.0 V resulted in bubbling caused by water electrolysis.

Experiments showed that nucleation starts on the tip of both electrodes and appears in the form of PEDOT protuberances with a spatial periodicity that is not related to the signal's periodicity (**Figure 5**). The polymer branches from both electrodes were directed toward each other and grew in a nearly similar morphology and size (**Figure 6a**. V_p = 4.5 V, 5.5 V, 6.5 V cases). As the dendrites grew toward each other, their periphery were expanding in diameter. Eventually, a merging of the structures from both sides occurred at equidistance between wires. It can be explained by the symmetry of the applied waveforms around 0 V baseline (dc = 50%, V_{off} = 0 V) that consequently lead to equable material agglomeration on both wires.

The only exception out of this observation was the lower-voltage case at V_p = 3.5 V, in which electropolymerization from one electrode happened intensively and faster than from another one, promoting non-symmetrical protuberances generation (**Figure 5a**). One can associate it to

the fact that, at such a low voltage limit, the growth symmetry can be highly sensitive to the wire cutting.

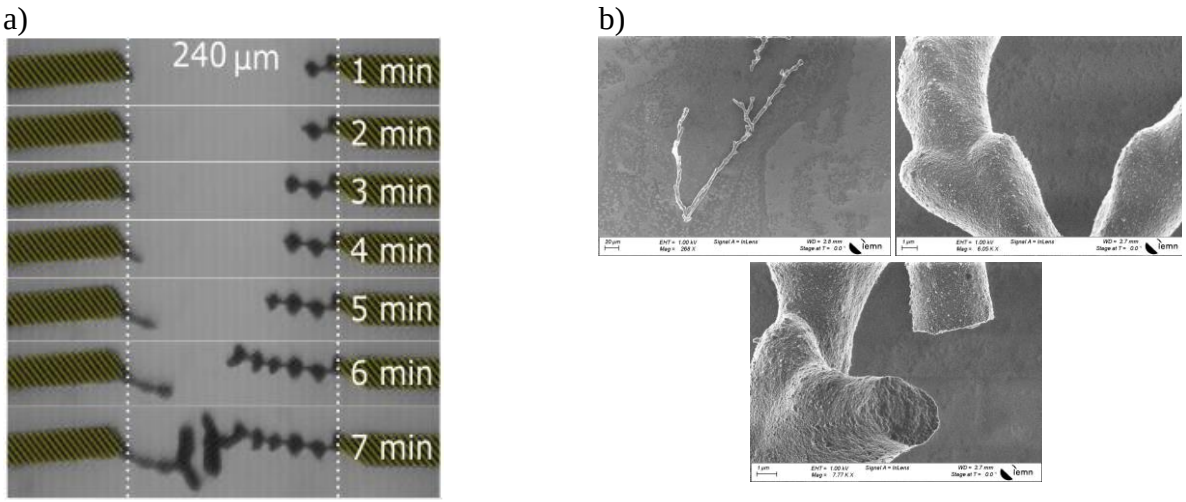

Figure 5. a) Microscope pictures of polymer dendrite propagation at different periods during electropolymerization (V_p= 3.5 V, V_{off} = 0 V, f = 80 Hz, dc = 50%). The yellow colored regions identify the position of Au wires. b) Scanning electron microscope images of PEDOT:PSS dendritic branches after their extraction from their "mother" electrolyte[11].

Obtained PEDOT structures are mechanically fragile and could hardly be removed from the electrolyte without damaging them. Scanning electron microscopy (SEM) images confirm it. In **Figure 5b,** one can observe structures' brittleness with sharp-edged cut, suggesting non- plastic properties for the polymer. Additionally, SEM shows multi-scale morphological richness by apparent branchy structures at the 10–100 µm range and sub-µm rough texturing (**Figure 5b**).

Morphology

For every single V_p value experiment, the evolution of PEDOT dendrites was captured until dendrites interconnected and further image and video processing was conducted.
It was found out that voltage amplitude has a direct influence on the shape of formed structures, namely on branching degree, volume, and surface (**Figure 6a**). By image analysis, characteristics such as Number of Brunches, 2D fractal Number as well as Projected area were extracted. Low V_p values led to objects with a degree of branching close to one (for instance, a wire-like dendrite at V_p = 3.5 V), while higher V_p promoted appearance of bulkier and branchier structure with up to five branching degree (defined as the average number of parallel branches on all longitudinal positions between the gold wires). Along with branches quantity, projected area (2D-image of the 3D object) value as well raised with increasing V_p. Interestingly, the branching factor and fractal dimension increase for dendrites electropolymerized from V_p = 3.5 V to 5 V and decrease afterward.

a)

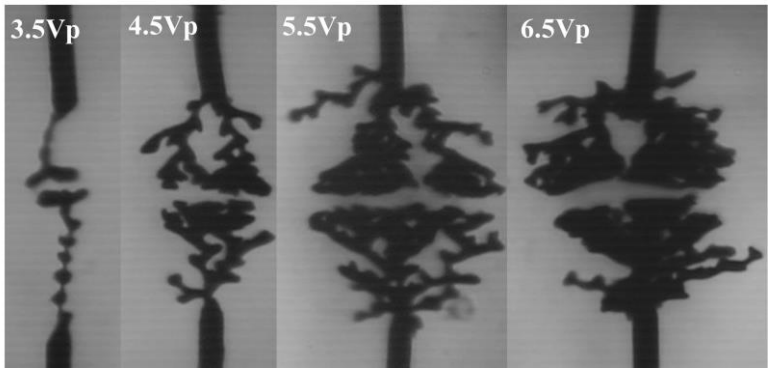

b)

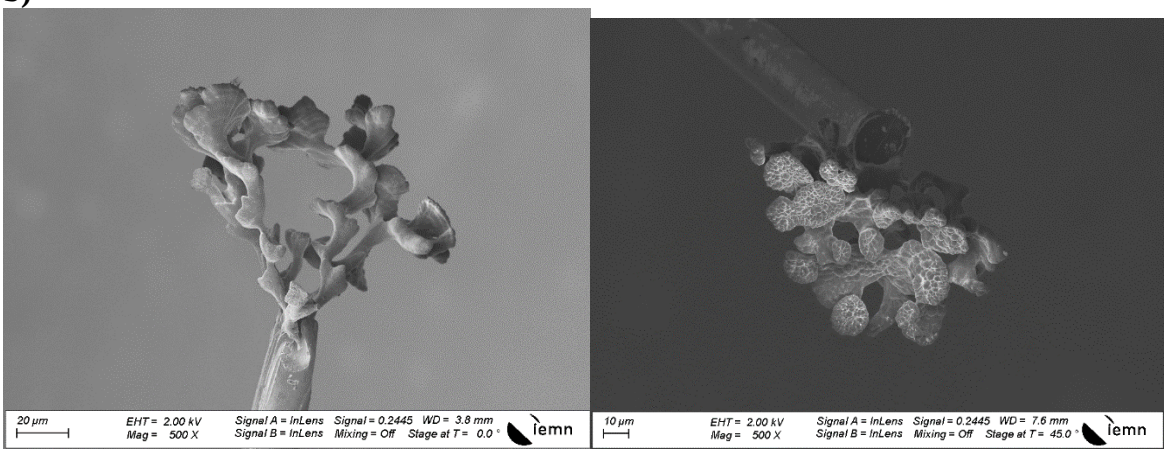

Figure 6. a) Microscope pictures of different dendritic objects before their completion, grown at different V_p [11]. b) Scanning electron microscope images of PEDOT dendritic structure on a wire (developed at V_p = 5 V) extracted from the electrolyte before its completion with the opposite dendrite.

Growth rate

Aside from morphological aspects, V_p modulation allows the control of the growth dynamics. The time needed for both electrodes' branches to merge together, i.e., completion time, was also extracted from the recorded videos of the dendritic growths[14]. The rise of V_p resulted in a more intense and faster generation of PEDOT dendrites, which corresponds to the lowering of completion time with the increase of V_p (**Figure 7**).

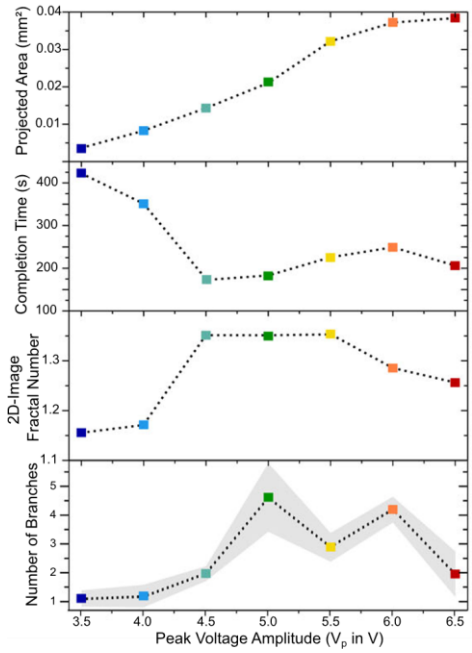

Figure 7. Projected area, completion time and branching degree over V_p for dendrites grown up until contact[11].

From color-coding images, one can also differentiate how fast the growths occur. Encoding reflects the color depending on the growth phase. Parts of the structure colored in black represent earlier formation, while brighter colors represent later formation (**Figure 8**).

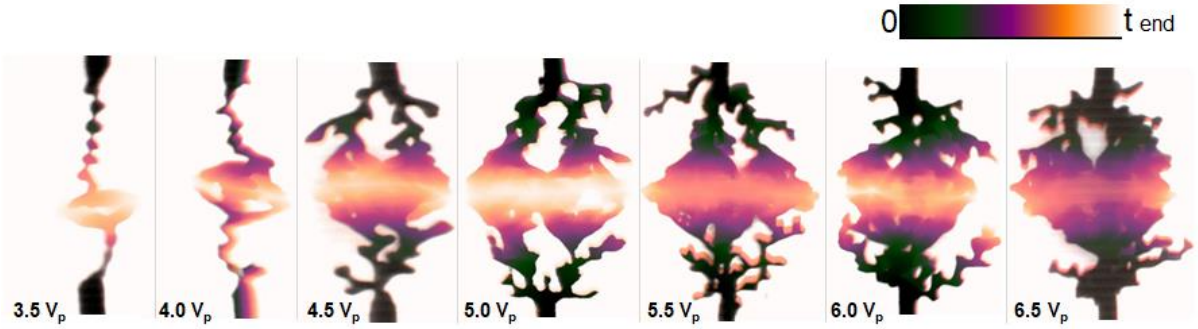

Figure 8. Color-encoded images of dendrites' evolution with time from 0 to t_{end} (the moment of branches completion). The inset is a linear color scale over time.

Through time-lapse frame processing of recorded microscope videos, it was noticed that the projected area changes not only between different V_p electropolymerization cases but also during the maturation of one certain structure with time. The slowest growth was exhibited by dendrites developed at V_p = 3.5 V. Further increase of V_P value showed a faster and more intense accumulation of material, i.e enlarging of projected area *(*as 2D projection of the 3D object*)* (**Figure 7**). At V_p = 5 V, growth saturation with a rate of 150 $\mu m^2/s$ was observed (**Figure 9**). This saturation indicates reaching an upper limit of charge-transfer rate for either

oxidation or reduction reactions, which in turn produces relatively comparable growths for $V_P \geq 5$ V under these conditions.

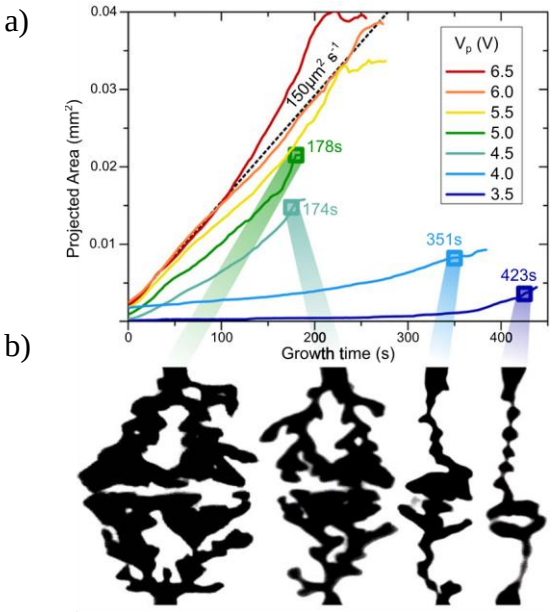

Figure 9. a) Projected area over time for dendritic structures grown at various V_p (at constant V_{off} = 0 V, f = 80 Hz, dc = 50%). b) Contrasted microscope images of four different dendrites, grown at different V_p (V_{off} = 0 V, f = 80 Hz, dc = 50%)[11].

For all experiments with varying V_p, new PEDOT nuclei had a tendency to accumulate on the periphery of already-grown dendritic material rather than on the sides of the gold wires. It is mainly related to two main phenomena: electric field activation of the process (for every single V_p case, dendritic growth appears along the longitudinal wire-to-wire axis) and the lower EDOT oxidation rate at the gold/electrolyte interface than the PEDOT/electrolyte one (implying low resistance of gold/PEDOT contacts and good conductivity of PEDOT material). In this system, field-effect sensitivity originates from the influence of the anode-to-cathode distance that controls the ionic transport resistance 1/G, which in turn governs the voltage drop at both anode/electrolyte and cathode/electrolyte interfaces.

5. Morphological influence with frequency

Analogously, to understand the frequency (f) influence, a range of frequency values from 10 Hz till 1 kHz was examined, while all other parameters were fixed (V_p = 5 V, V_{off} = 0 V, dc = 50%). At a frequency below 10 Hz, bubbling occurred due to water electrolysis and prevented the formation of dendrites. This behavior indicates the effect of the applied voltage lasting for a long time that consequently leads to water electrolysis. As in the case of V_p, experiments with frequency variations have shown that dendrites grew equally from both Au wires along one direction toward each other.

a)

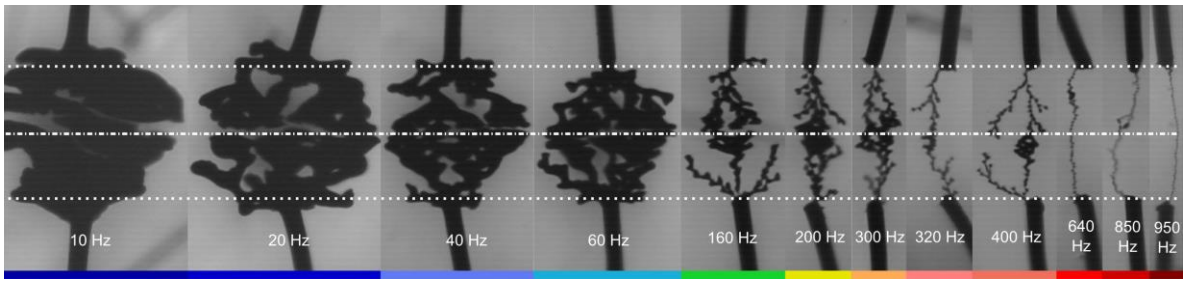

b)

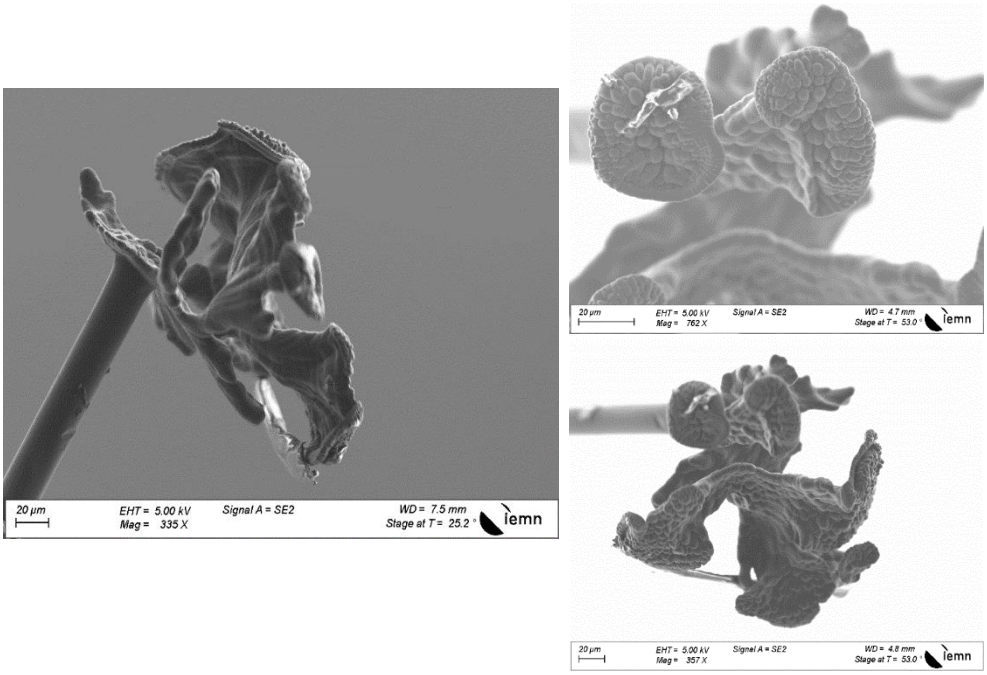

Figure 10. a) Microscope pictures of PEDOT dendritic morphologies (signal wire: top, ground wire: bottom) at their completion time grown at different frequencies from 10 to 950 Hz (V_p = 5 V, V_{off} = 0 V, dc = 50%)[11]. b) Scanning electron microscopy images of a PEDOT dendritic structure developed at 20 Hz after its extraction from the electrolyte

Figure 10a shows similarities between V_p and frequency modulation. Both can alter the morphology of obtained PEDOT branches. Microscope images show that decrease of frequency lead to an enlarging of final PEDOT form with higher branching degree, while increase of frequency oppositely causes lowering the number of branches and appearing of much thinner wire-like structure. More precisely, this observation was confirmed by the results of time-lapse processing of recorded videos (**Figure 11**), according to which branching degree gradually diminishes with increasing *f* value.

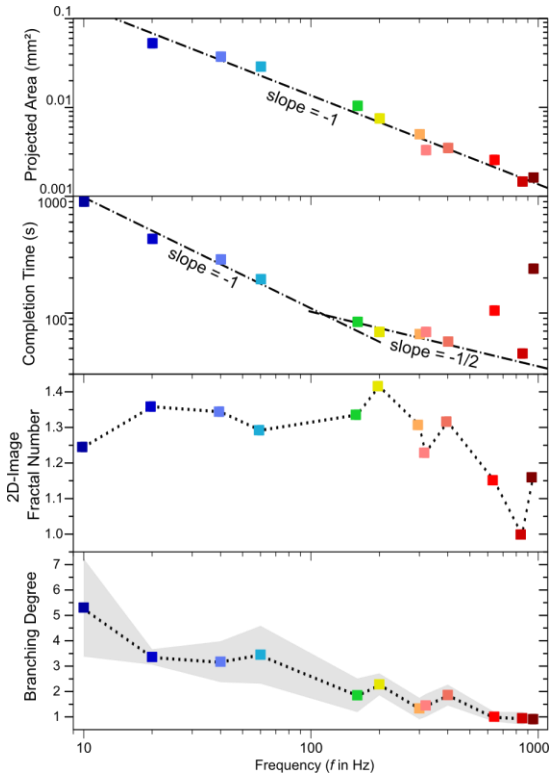

Figure 11. Projected area, completion time, branching degree over *f* for dendrites grown up until contact[11].

Along with the change in the number of branches, the diameters of the polymer wires have also been altered. The variation in projected area supports this statement. Taking into account the elementary cylinder approximation that will be discussed further in Chapter 3 (at least for the highest frequency cases where dendrites appear as linear cables), one can conclude that the projected area parameter is directly proportional to the dendrite's branches diameter. The dependence of projected area on the frequency appeared inversely proportional, implying that projected area is linear with the waveform's period (as shown on **Figure 11** by the -1 slope in double log scale).

Video analysis did not show significant changes for the structures obtained at $f < 300$ Hz in terms of 2D fractal number. Above 300 Hz, a decrease in the 2D fractal number was noticed, which is generally correlated with a decrease in dendrite size and branches number.

In terms of dynamics, employing low frequency lead to a longer time for dendrites generation and their completion, while increasing the number of pulses per second resulted into faster bridging of both electrodes by PEDOT wires. However, two distinct regimes of growth dynamics can be seen on the graph. In the frequency range below 200 Hz, a quicker interconnection occurs with *f* rising, which is displayed by a linear relationship between completion time and frequency as a -1 slope in double log scale.

At *f* above 200 Hz, dendritic growth appeared in a slower manner, which is exhibited by a $-1/2$ slope on the double log plot in **Figure 11**. Nevertheless, a deviation from this trend for $f > 200$ Hz was found out. Precisely, the substantially much thinner dendritic structure obtained at 950 Hz showed much slower interconnection, which was out of the tendency described by the -1/2 slope. Further frequency increment above 1 kHz caused minor nucleation at the micrometer scale that did not lead to an accomplished polymer connection at these

conditions, due to a too long completion time, not compatible with preserving the electrolytic drop from substantial evaporation.
The morphological influence of various *f* can be related to the fact that at low *f*, monomer particles will have more time to aggregate at the electrode, which will lead to more sites of nucleation. Consequently, it will result in the appearance of more fluffy structures. On the contrary, at high *f* due to the short duration of polarization, the time for EDOT particles to seed around the electrode and to be oxidized is reduced; therefore, at such conditions, formation of multiple branches is hindered.

6. Morphological influence with voltage offset

Influence of voltage offset (V_{off}) was tested in the range from -1 V to +1 V while other parameters were kept as V_p = 5 V, *f* = 80 Hz, dc = 50%. It was discovered that by introducing a V_{off} in the waveform, a strong asymmetry in dendritic growth between pairs of wires can be induced. V_{off} modulation of bipolar pulses leads to modification of the waveform in the way so V^+ and V^- polarization will be defined as follow: $V^+ = V_{off} + V_p$, $V^- = V_{off} - V_p$.
It was observed that with increasing positive V_{off}, growth asymmetry is shifted towards signal wire at which larger arborescences take place while at the ground wire, less intense electropolymerization led to wire-like objects formation. On the contrary, with decreasing V_{off}, the asymmetry of growth is reversed and more polymer maturing prevails on the ground electrode rather than on signal one (**Figure 12**). This visual observation is supported by the results of projected area analysis, which show that the structure's projected area steadily grows as V_{off} increases (**Figure 13b**).

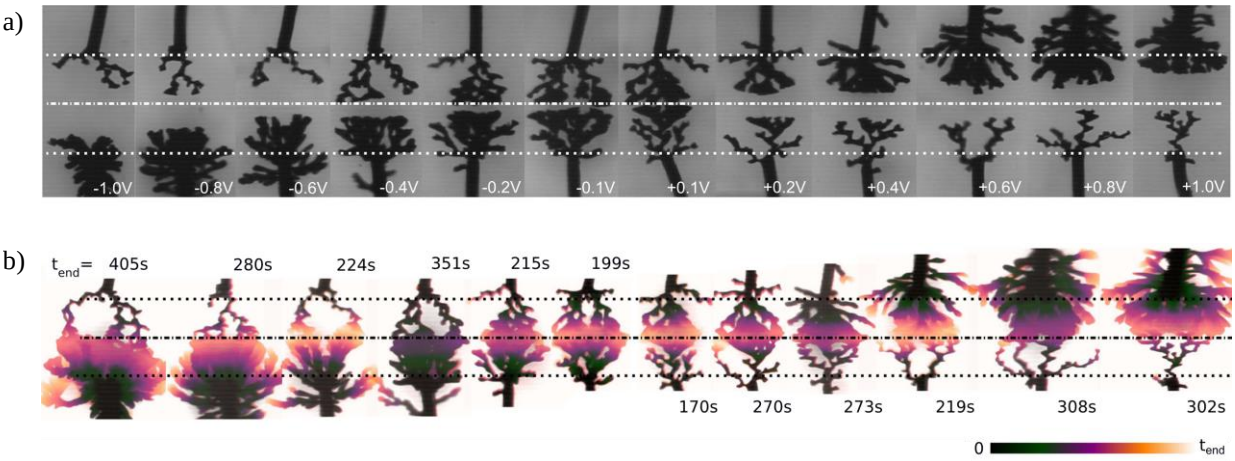

Figure 12. a) Microscope pictures of dendritic structures at t = 150 s of voltage polarization under different V_{off} (V_p = 5 V, *f* = 80 Hz, dc = 50%) (signal wire: top, ground wire: bottom). b) Color-encoded temporal images of the same dendrites grown from 0 to t_{end} (the color scale is presented as an inset in the form of a linear scale over time) [11].

Additionally, to estimate the asymmetry impact with V_{off}, the ratio between the projected area of signal's dendrite and ground's was calculated and shown as a function of time. So, a gradual and monotonic trend of asymmetry change with $|V_{off}|$ modification was obtained **(Figure 13a**). From video analysis, it turned out that with the raise of $|V_{off}|$, longer time is required to form completed dendritic interconnections (**Figure 12b**, **Figure 13 a, c**). Branching degree

examination was conducted separately for dendrites grown on signal and ground electrodes (**Figure 13d**). However, no significant changes in terms of branching sparsity for signal's dendrites were noticed at V_{off} variation from -0.1 V to 0.1 V. The same trend appeared for structures developed at ground wire. However, based on microscopic images, it can be seen that with increasing $|V_{off}|$, more branches with a thicker diameter occurred. However, due to their proximity, several of the same branches can be mistaken for one large branch. Therefore, such a trend (for both the signal and ground electrodes) shown in **Figure 13d** can be explained by the fact that on 2D image this above morphological feature was not taken into account during the elementary cylinder approximation analysis.

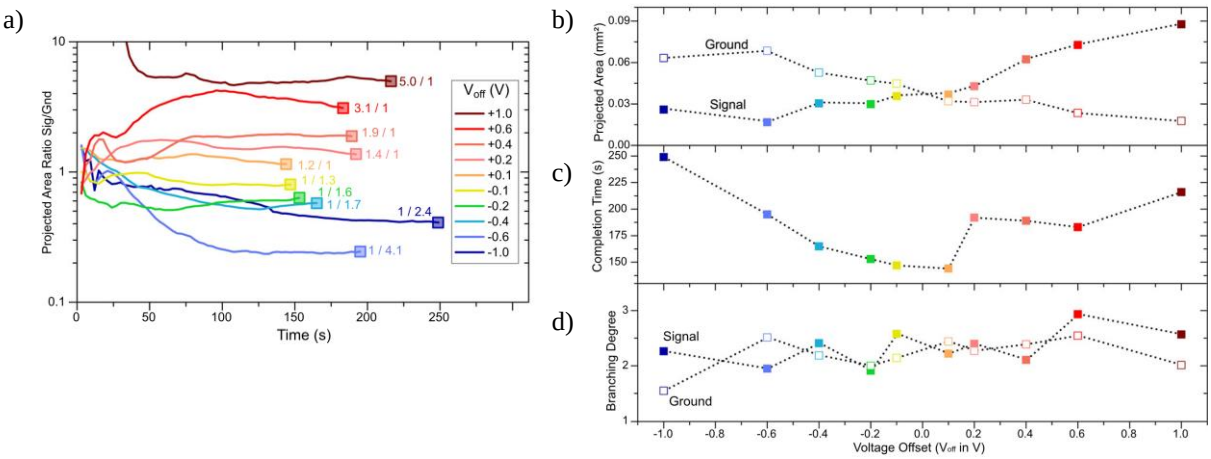

Figure 13. a) Ratio between the projected area of dendrites grown on signal and ground wires over time at different V_{off}. b) Projected area, c) completion time, and d) branching degree over V_{off} for dendrites grown up until contact. Scatters and curves' color encodings with various voltage offset in **a** and **b** are identical[11].

Such a change of morphology can be explained by the fact that V_{off} influences the system in two distinctive ways. It generates anodic and cathodic voltage-asymmetry between both wires, which in turn leads to different electropolymerization rates for both wires. Also, non-identical electric-field magnitudes are produced during both polarization within a period, with different field lines governing different growths orientation. Both of these effects are associated with the previously revealed morphological influence of V_{off} on the growth rate and its anisotropy.

Even though the changes in V_{off} result in an electric field of different magnitude on the dendrites forming at both wires, still both signal's and ground's dendrites are interconnecting in the middle of the gap. This indicates growth prevails more at one electrode than at the other due to V_{off}, the equatorial component for both growths (parallel to the electric field) remains comparable, with the same growth speed, which does not correlate with the dendrite morphology.

With changing V_{off}, dendritic morphologies from both electrodes mature in two distinctive regimes: the thinnest dendrite appears to be the most linear and longitudinal with the equatorial direction, while the densest one shows always radial growth.

This indicates that the thinnest dendrite (experiencing a lower applied oxidation voltage) is more affected by the electric field than the thickest dendrite (experiencing a higher applied oxidation voltage). Thus, dendritic growths are independently regulated by both the voltage amplitude at the electrode and their induced electric field.

As it was shown in **Figure 2**, during AC polarization wires behave both simultaneously as anode and cathode (as $V_p > V_{off}$ in each case) and growths are carrying out on both wires (as $V_p - V_{off} > \Delta V_{min}$ in each case). However, since the wire that experiences the highest oxidation stress must also be exposed to the highest field polarization, this demonstrates that field orientation controls growth only for low growth rates, since thin dendrites appear to be straighter along the field orientation than thicker ones.

The observed shift in growth direction evidences voltage non-linearity in the charge-transfer yielding non-similar anodic processes of electropolymerization on wires. This non-Ohmic behavior under quasi-steady conditions was confirmed by voltage-ramped impedance spectroscopy (**Figure 14a**), which was carried out on the two-gold-wire setup immersed in the same electro-active electrolyte (10 mM BQ, 10 mM EDOT, 1 mM NaPSS) with V_{DC} increasing from 0 to 1.3 V. Through fitting of obtained spectra, one can get a quantification of R_{CT} (charge-transfer resistance), C_{dl} (double layer capacitance created either by Na^+ or by PSS^-) and G (conductance of electrolyte) parameters and their possible modification with V_{DC} change. G value did not change significantly and was quantified as 8.5 ± 0.2 µS, while R_{CT} and C_{dl} were evolving with V_{DC}. **Figure 14b** shows that as the direct-current voltage bias (V_{DC}) gradually increased over time in the experiment, a sudden decrease in charge transfer resistance $R_{CT} = R_{ox} + R_{red}$ was observed with approaching $V_{DC} = \Delta V_{min}$. Such tendency for decreasing R_{CT} and C_{dl} values was expected, since no oxidation of EDOT takes place at low voltage. Nevertheless, after reaching its minimum value, R_{CT} value surprisingly exhibited an increase with a further raise in V_{DC}.

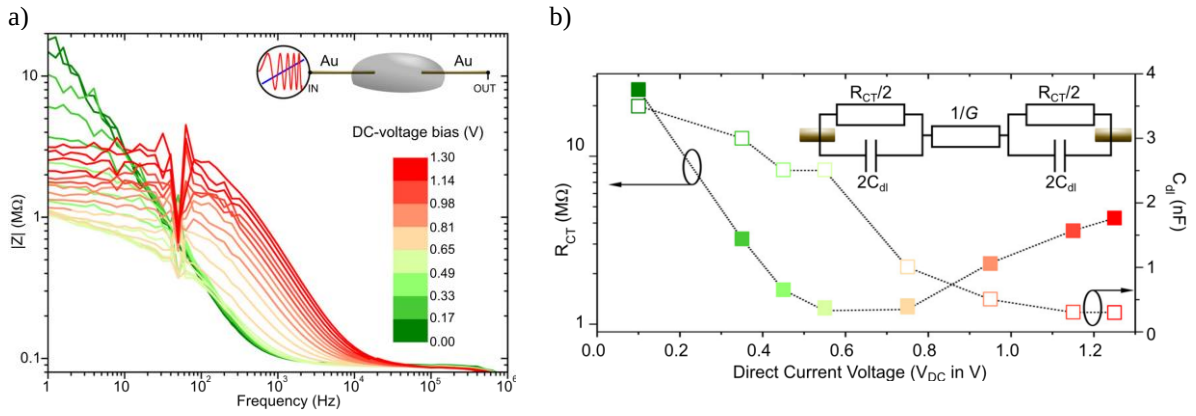

Figure 14. a) Voltage-ramped impedance spectroscopy between $V_{DC} = 0$ and 1.3 V of the two- gold- wire setup immersed in the same electro-active electrolyte (10 mM $BQ_{(aq)}$, 10 mM $EDOT_{(aq)}$, 1 mM $NaPSS_{(aq)}$). b) Evolution of extracted R_{CT} and C_{dl} parameters obtained by fitting of the spectrum according to the idealized equivalent circuit that depicted as an inset ($G = 8.5 \pm 0.2$ µS). Scatters and curves' color encodings with DC voltage evolution in **e** and **f** are identical[11].

It confirms the voltage activation of the growth and also invalidates the linearity of the applied electric field $E = (V'_{sig} - V'_{gnd})/d$ ($d < L$ as shortest distance between two dendrites), with V'_{sig} and V'_{gnd} being $R_{CT}(V_{DC})$ dependent, and hence dependent on V_{off}.

Furthermore, it was observed that after the completion of both parts (from signal and ground wires), maturation still continues in the form of additional radial branches emerging from the thickest dendritic structure for higher $|V_{off}|$ values. This evidenced in **Figure 12b** from color encoded time lapse images (recorded until the t_{end} longer than their respective completion time)

of dendrites generated at V_{off} = -0.4, +0.2, and +0.8 V. Such feature indicates good electrical conduction for these asymmetric objects after their merging. It means that after merging dendrites, when the signal continues, the electrical conduction is limited by the resistance of the fused dendrites, for which the higher value causes the voltage to drop all along the dendritic connection. Therefore, the highest point of the applied potential will be strictly on the gold surface of the anodic wire. As a result, electropolymerization continues further after merging by the creation/expansion of new branches on gold.

7. Morphological influence with the duty cycle

To discover duty cycle's (dc) influence, dc values were tested as 30%, 40%, 50%, and 60%, while V_p = 5 V, f = 80 Hz, and V_{off} = 0 V were kept unchanged. Experiments showed that introducing 30% and 70% dc caused water electrolysis. Shifts of dc to 40% and 60% led to morphological asymmetry on both wires as in cases with V_{off} with a predominance formation of a larger structure on one electrode and a smaller one on the other. At 60%, dendritic growths appeared denser on the signal wire than on the ground one, whereas at 40% polymer maturation appeared vice versa (**Figure 15a**). The growth was generally enhanced on the wire experiencing the longest anodic duration.

However, surprisingly in both aforementioned cases, an engulfing effect has been observed after a merging of dendritic fibers from both electrodes: dendrites growth from the bulkier part continued to propagate along the wires and densified the connection in polymer material (as it can be seen from color-encoded images in **Figure 15b**). In previous experiments with dc = 50% to study the influence of V_p, V_{off}, and f, such an effect was not observed: all dendrites converged to the middle of the gap without further PEDOT formation in the direction of the opposite electrode occurred. At dc = 50%, if a signal was given after the interconnection of the dendrites, further growth densified only in that interconnection area in the middle of the inter-electrode gap, leading to an increase in its diameter.

Therefore, duty cycle modulation allowed of forming more robust interconnections, with the two wires welded together by the thickest PEDOT dendrite engulfing the thinnest one after completion.

a)

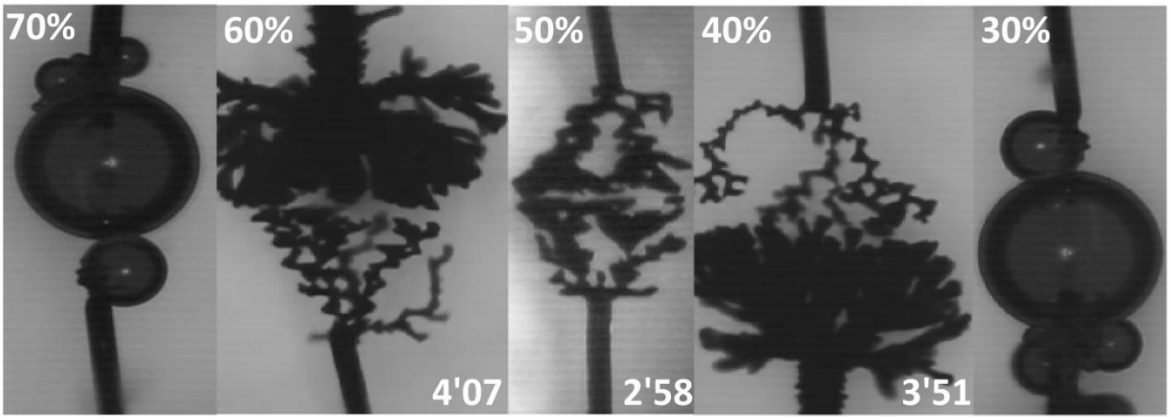

b)

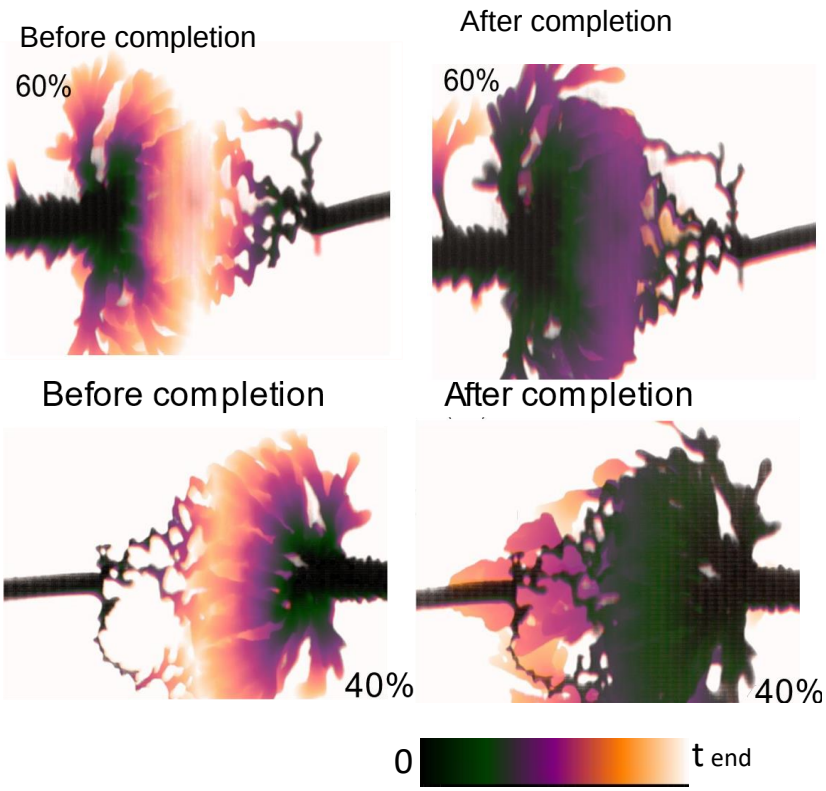

Figure 15. a) Microscope pictures of dendritic formations (signal wire: top, ground wire: bottom) at completion time generated at various dc values and V_p = 5 V, V_{off} = 0 V, f = 80 Hz. b) Color-encoded temporal images of the dendrites grown at 40% and 60% dc variations showing two specific dynamics before and after completion. Adapted from [11].

Duty cycle values variation leads to a comparable asymmetry effect that was previously observed for V_{off} modification. As an explanation, to verify a relationship between these parameters, the Fourier decomposition (Equations 1 and 2)[15] of the pulse waveform was considered:

$$V_{sig}(t) - V_{gnd} = V_{off} + (2dc - 1)V_p + \sum_{n=1}^{\infty} \frac{4V_p}{n\pi} sin(\pi ndc) * cos(2\pi nf * t) \quad (1)$$

$$V_{sig}(t) - V_{gnd} = dcV^+ + (1 - dc)V^- + \sum_{n=1}^{\infty} \frac{2(V^+ - V^-)}{n\pi} \sin(\pi ndc) * \cos(2\pi nf * t) \quad (2)$$

Equation (2) exhibit that introducing dc leads to an asymmetry of the temporal polarization densities (between V^+ and V^-) that consequently allows inserting a time-invariant term V_{DC} in the waveform without breaking the applied-voltage asymmetry of the V^+ and V^- around the zero baseline (Equation 3)

$$V_{DC} = V_{off} + (2dc - 1)V_P = dcV^+ + (1 - dc)V^- \quad (3)$$

From the Fourier expression of the pulse wave, V_{DC} equals a sum of V_{off} and a fraction of V_p in accordance with dc. Therefore, for instance applied dc = 60% will generate V_{DC} = 1 V, dc of 70% will lead to V_{DC} = 2 V and dc of 40% to the V_{DC} = −1 V at constant V_p = 5 V, V_{off} = 0 V.

This relationship (of V_{DC} on V_{off} and dc) from Equation 3 in the experiments is evidenced through the modification of the projected area ratio signal/ground ρ(dc, V_{off}).

For instance, dependency of the projected area ratio signal/ground ρ(dc,V_{off}) with the duty cycle is following: at completion time ρ(40%, 0 V) = 0.18 and ρ(60%,0 V) = 3.11. Additionally, previous experiments at V_{off} variation exhibited that ρ(50%,−0.6 V) = 0.24 and ρ(50%,+0.6 V) = 3.1 (**Figure 13a**). Therefore, this ρ(dc,V_{off}) dependency suggests that the dc component in the waveforms rules the dendrites' asymmetry in both V_{off} and dc variation series. This indicates that the electropolymerization occurs at double-layer charging and not in the electrolytic conduction regime.

In terms of circuit-element analysis, the V_{DC} control by the dc and, therefore asymmetry of growth comes from the temporal asymmetry of the charge/discharge processes at both electrodes. In previous experiments at dc=50%, the durations for charging and discharging the wires were equal. However, once the duty cycle is modified, the duration for V^+ and V^- polarization is different and leads to non-equal time for the charging and discharging processes on both wires. As a result, it leads to partial accumulation (charging) of one particular type of ion at both electrodes, which is favored by the longer-lasting polarization. For example, at dc=60% the anodic polarization (V^+) is longer, so one will have more time to attract anions (PSS^-) at the signal wire, but once the polarization is switched to V^-, not all of the accumulated PSS^- ions will leave the electrode due to lack of time for it. Therefore, a part of the anion space- charge will still be present on the signal wire even after the change of polarization to V^-. After several cycles' iterations, much more PSS^- will be accumulated on a signal's dendrite (grown during these iterations), leading to a charge build-up. At the same time, the ground electrode will experience a similar partial charging but with Na^+ ions. Therefore, such charge build-up at the double-layer capacitors of both dendrites will generate dc-dependent potential pinning, which will cause asymmetry in dendritic growth. This effect is specific to dc and has not previously been associated with the dependence on V_p, V_{off}, and *f*.

Bubbling at dc=30% and dc=70% can also be explained on the base of this potential pining. As it was mentioned, such a charge build-up promotes a transient dc-dependent over-potential at both electrode interfaces, which can have a higher voltage in absolute value than the applied one $|V_p|$. It was shown by electric simulation (depicted in the work [13]) on the equivalent circuit of the system at various dc values.
This process in detail happens as follows. At the beginning of the experiment ($t = 0$), both double layers are unformed around the wires, so the initial state of their corresponding capacitor are fully discharged and induce exponential decays with V_{sig} and V_{gnd}, as starting values of their surface potentials. At the second polarization alteration ($t = T^+ = dc*T$), the electrostatic charge/discharge of the double-layer capacitors changes due to partial charge from past polarizations and it is already initiated from values other than initial V_{sig} and V_{gnd} (modified polarization values correspond to V'_{sig} and V'_{gnd}). Consequently, the generated transient electric fields across the electrolyte are much higher in magnitude than the voltage initially applied on the gold wires ($|V'_{sig}| > \max(|V^+|;|V^-|)$ and $V_{gnd} \neq 0$). This phenomenon is typical for each of the previously studied cases. However, duty cycle asymmetry allows extending the time windows for one preferential ionic charge/discharge over the other at each electrode, which in turn modifies the initial potential pinning of the initial state of the charge/discharge at each potential inversion. Thus, at 30% and 70% dc values, one may expect a longer influence of such overpotential, which inevitably leads to water electrolysis appearing in the form of bubbling.

Discovered here phenomenon of potential pining modification can be used for practical tasks. Additionally, this overpotential pining can be modified by a signal from another electrode (that previously served as a ground in the aforementioned experiments). For instance, small amplitude spikes with various frequencies can be used as such types of signal. Depending on the intensity and amount of the applied spikes, changes in potential pinning will occur, which consequently may trigger electropolymerization differently, and thus one may use it as a computation platform. In detail, such an application of potential pinning modification will be shown in Chapter 4.

Discussion

In this chapter, we discovered that AC electropolymerization process resulted in PEDOT:PSS fibers formation, which can mimic neural dendrite arbor morphogenesis. Moreover, by changing waveform parameters such as voltage offset, amplitude, frequency, and duty cycle, a large versatility of electrical interconnection can be introduced. Namely, by varying these parameters, the morphology of polymer bridges changes in terms of the number of branches, surface (projected area), volume, and asymmetry of the growth between two wires. It was also found that the dynamics of the electropolymerization, and therefore the speed of branches' interconnecting can be controlled by certain parameters like V_p or V_{off}. Furthermore, the engulfing effect of one polymer branch by another caused by DC modification was discovered as a method of connection densification.
In addition, we have also presented how changing the parameters can eventually affect the electric field of the system, for example, in terms of R_{CT} or different durations of charge/discharge processes on the wires, which ultimately change the electropolymerization dynamics and therefore lead to different morphologies.
Since the structure of the obtained dendrites is based on PEDOT:PSS, they are expected to act

as OMIEC and thus can be utilized for devices development. Therefore, since it is known how to grow and modify dendritic morphologies, it would be interesting to verify if the obtained dendrites are capable of acting as active devices, i.e., OECT. Moreover, due to the possibility of obtaining variable morphologies, it would be interesting to examine if these different dendritic interconnections exhibit non-similar properties and different efficiencies as active devices.

Literature

(1) Prigge, C. L.; Kay, J. N. Dendrite Morphogenesis from Birth to Adulthood. *Curr. Opin. Neurobiol.* **2018**, *53*, 139–145. https://doi.org/10.1016/j.conb.2018.07.007.

(2) Abdel-Maguid, T. E.; Bowsher, D. Classification of Neurons by Dendritic Branching Pattern. A Categorisation Based on Golgi Impregnation of Spinal and Cranial Somatic and Visceral Afferent and Efferent Cells in the Adult Human. *J. Anat.* **1984**, *138* (Pt 4), 689–702.

(3) Bicanic, I.; Hladnik, A.; Petanjek, Z. A Quantitative Golgi Study of Dendritic Morphology in the Mice Striatal Medium Spiny Neurons. *Front. Neuroanat.* **2017**, *11*.

(4) Grudt, T. J.; Perl, E. R. Correlations between Neuronal Morphology and Electrophysiological Features in the Rodent Superficial Dorsal Horn. *J. Physiol.* **2002**, *540* (Pt 1), 189–207. https://doi.org/10.1113/jphysiol.2001.012890.

(5) Watanabe, T.; Ohira, M.; Koizumi, Y.; Nishiyama, H.; Tomita, I.; Inagi, S. In-Plane Growth of Poly(3,4-Ethylenedioxythiophene) Films on a Substrate Surface by Bipolar Electropolymerization. *ACS Macro Lett.* **2018**, *7* (5), 551–555. https://doi.org/10.1021/acsmacrolett.8b00170.

(6) Ohira, M.; Koizumi, Y.; Nishiyama, H.; Tomita, I.; Inagi, S. Synthesis of Linear PEDOT Fibers by AC-Bipolar Electropolymerization in a Micro-Space. *Polym. J.* **2017**, *49* (1), 163–167. https://doi.org/10.1038/pj.2016.100.

(7) Koizumi, Y.; Ohira, M.; Watanabe, T.; Nishiyama, H.; Tomita, I.; Inagi, S. Synthesis of Poly(3,4-Ethylenedioxythiophene)–Platinum and Poly(3,4-Ethylenedioxythiophene)–Poly(Styrenesulfonate) Hybrid Fibers by Alternating Current Bipolar Electropolymerization. *Langmuir* **2018**, *34* (26), 7598–7603. https://doi.org/10.1021/acs.langmuir.8b00408.

(8) Inagi, S. Site-Selective Anisotropic Modification of Conductive Objects by Bipolar Electropolymerization. *Polym. J.* **2019**, *51* (10), 975–981. https://doi.org/10.1038/s41428-019-0223-2.

(9) Koizumi, Y.; Shida, N.; Ohira, M.; Nishiyama, H.; Tomita, I.; Inagi, S. Electropolymerization on Wireless Electrodes towards Conducting Polymer Microfibre Networks. *Nat. Commun.* **2016**, *7* (1), 10404. https://doi.org/10.1038/ncomms10404.

(10) Rivnay, J.; Inal, S.; Collins, B.; Sessolo, M.; Stavrinidou, E.; Strakosas, X.; Tassone, C.; Delongchamp, D.; Malliaras, G. Structural Control of Mixed Ionic and Electronic Transport in Conducting Polymers. *Nat. Commun.* **2016**, *7*, 11287. https://doi.org/10.1038/ncomms11287.

(11) Janzakova, K.; Kumar, A.; Ghazal, M.; Susloparova, A.; Coffinier, Y.; Alibart, F.; Pecqueur, S. Analog Programing of Conducting-Polymer Dendritic Interconnections and Control of Their Morphology. *Nat. Commun.* **2021**, *12* (1), 6898. https://doi.org/10.1038/s41467-021-27274-9.

(12) Hiesgen, R.; Haiber, J. MEASUREMENT METHODS | Structural Properties: Atomic Force Microscopy. In *Encyclopedia of Electrochemical Power Sources*; Garche, J., Ed.; Elsevier: Amsterdam, 2009; pp 696–717. https://doi.org/10.1016/B978-044452745-5.00073-3.

(13) Orazem, M. E.; Tribollet, B. *Electrochemical Impedance Spectroscopy*, 2nd edition.; John Wiley & Sons, Inc: Hoboken, New Jersey, 2017.

(14) *Dataset for: Analog Programing of Conducting Polymer Dendritic Interconnections and Control of their Morphology*. figshare. https://doi.org/10.6084/m9.figshare.16814710.v1.

(15) Smith, S. W. The Scientist and Engineer's Guide to Digital Signal Processing 2nd Edn (California Technical Publishing, San Diego, California, 1997).

Chapter 3. Investigation of PEDOT:PSS dendrites as Organic Electrochemical Transistors (OECT)

Introduction

Knowing that it is possible to tune the morphology of the dendritic fibers, this chapter will be focused on exploring dendrites as active devices, namely as OECT. It will be demonstrated how different dendritic morphology obtained at different electropolymerization conditions can exhibit various OECT behaviors. Additional 3D modeling of dendritic structures will be used to explain the evolution of OMIEC properties under electropolymerization conditions. Finally, it will be shown how dendritic devices can be used to mimic memory functions such as STP and LTP.

1. Investigation of polymer dendrites as OECT

Among the artificial synaptic devices based on organic materials, organic electrochemical transistors (OECTs) became an attractive alternatives to inorganic counterparts referring to their flexibility in conductance tuning[1], high transconductance[2], low driving voltage comparable to biological synapses, fast response speed[3]. To date, OECTs successfully mimicked certain synaptic functions like STP, LTP and STDP[4,5,6].

One of the next objective in this work was to verify an opportunity to use dendrites as active device, as OECT specifically. For this purpose , dendrites were synthesized at different frequency values (*f*) 40 Hz, 80 Hz, 160 Hz and 320 Hz while all other parameters were kept constant V_p = 5 V, dc = 50% and V_{off} = 0 V, using already established protocol and setup. Therefore, frequency served as the main parameter to modify dendrites' morphology. To control the electropolymerization process, application of AC voltage was maintained during 30 s after interconnexion of the first branches from both electrodes.

As mentioned previously, the main working principle of OECT is based on electrochemical doping or dedoping processes of conductive polymer caused by extracting or inserting ions from/into the bulk of material and leading to the modification of the conductance state of the channel[7,8].

Conventional OECT device has a source electrode, a drain electrode and a channel connecting both electrically, and a gate that is electrochemically connected to them via an electrolyte, controlling ionic flux from the electrolyte to the channel. In our case, to test the dendrites, the same setup previously used for electropolymerization was employed. Gold wires used for pulse voltage propagation were set as source (S) and drain (D) electrodes. Polymer branches served as conductive channel and a chlorinated silver wire immersed inside the drop was employed as the gate (G). All the electrical characterizations took place in the same electroactive environment, where growth of dendrites has been carried out without additives. After electropolymerization process, the aqueous media still contained NaPSS salt, which previously played the role of electrolyte salt for electropolymerization and will still play that

role for driving the dendrite as an OECT. The reason for such a choice of setup was the fact that free-standing synthetic polymer fibers are quite fragile and any mechanical impact (such as pulling them out of the media or introducing another drop of a solution) may cause damages to the polymer fibers or their total withdrawal from electrodes.

1.1 Resistance characterization

As a first step to check the conductance of dendrites, resistance values were examined for each structure.

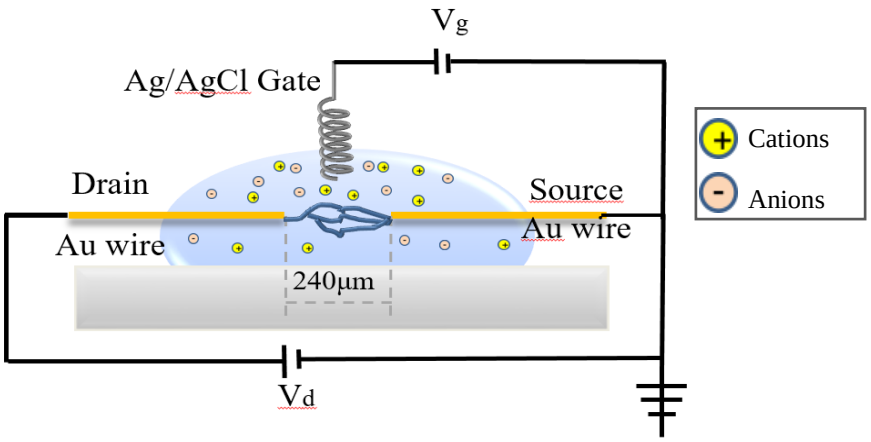

Figure 1. Experimental setup for examination of dendrites as OECT with an Ag/AgCl gate electrode[9].

Linear voltage sweep from 0 V until 0.5 V was applied in between both source and drain electrodes for all dendrites that resulted in linear and well distinguishable tendency of conductance dependency on the structure's morphology.
The linear current-voltage response directly evidenced an ohmic contact between the Au wires and the PEDOT:PSS 3D polymer (**Figure 2**).

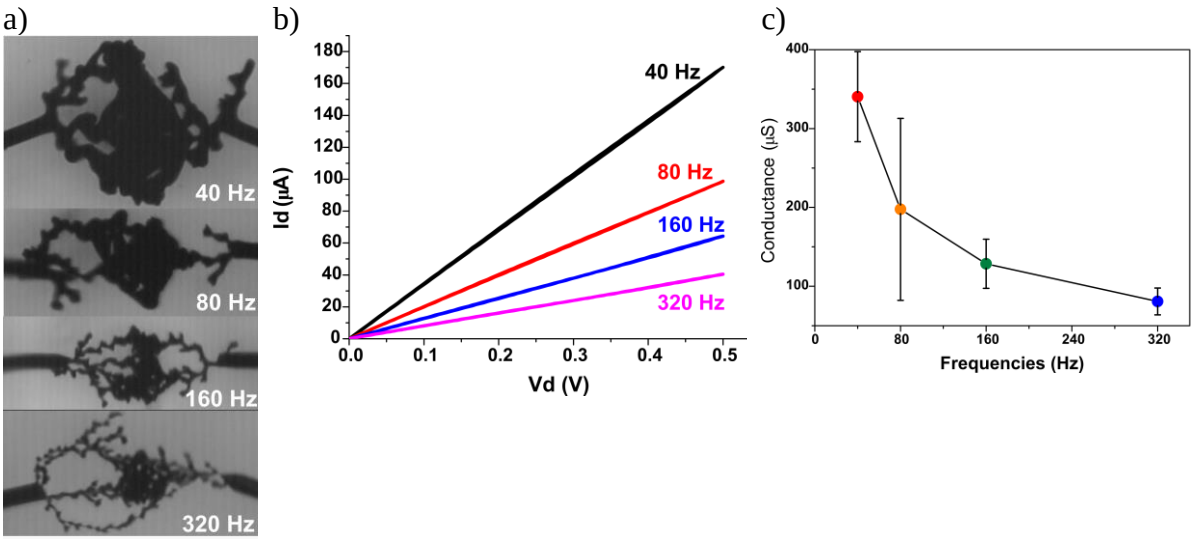

Figure 2. a) Microscopic images of examined dendritic morphologies obtained at various *f*. b) Resistance measurement: the drain-source current (I_{DS}) as a function of drain source voltage (V_{DS}) for different dendritic geometries. c) Conductance modification with respect to applied *f*. Error bars are calculated using three repetitions of the measurements[9].

As it was shown on current–voltage characteristics (**Figure 2b**), larger dendrites obtained at lower *f*, such as 40 Hz, showed higher conductance values. The conductance was progressively decreased with the decrease of *f* till 320 Hz, and consequently with the size of the structure. There is a direct relationship between conductance/resistance of the dendrite and its geometry that can explain such a trend. Overall, dendrites with a bulky shape synthesized at lower *f* because of their geometry contain more charge carriers responsible for higher conductance. On the contrary, structures obtained at 320 Hz possess comparably less quantity of charge carriers due to less amount of conductive material in total, and result in high resistance or small conductance among all tested topologies.

This possibility to control conductance states through different fabrication parameters is quite promising for further application of dendrites in analog programming and can be associated to a first definition of the synaptic weight between two neurons. In fact, this dendritic branching in between two terminals can be associated with connections between neural cells (i.e., equivalent to the pre- and post-neurons). Therefore, by means of such polymer dendrites, one can introduce a mechanism for structural plasticity at the hardware level and form necessary connections, or necessary computing units, upon controllable conditions, and program the conductance states that can resemble synaptic weight.
Moreover, unlike traditional top-down methods, such approach allows to build up only useful networks, which differs from standard top-down methods and could be beneficial in terms of functionality and production of devices.

1.2 Conductivity Evaluation

Additionally, based on image analysis and modeling carried out by Dr. A.Kumar, conductivity of each dendritic morphology was evaluated.
The optical images of dendritic OECTs are 2D projections of 3D morphology, where 2D rectangular wires can be represented as 3D cylindrical forms. Since wires width changes along

the dendrites' structure, the morphology was considered as a system of elementary cylinders, each having a diameter equal to the morphology's local width.
In the 2D reconstruction, the pixels composing the image were divided into dendritic and non- dendritic pixels, which were assigned conductance values of 1 and 0, respectively. The optical picture representation was then converted into a network representation (**Figure 3 a-b**), where each image pixel represented an individual network node.

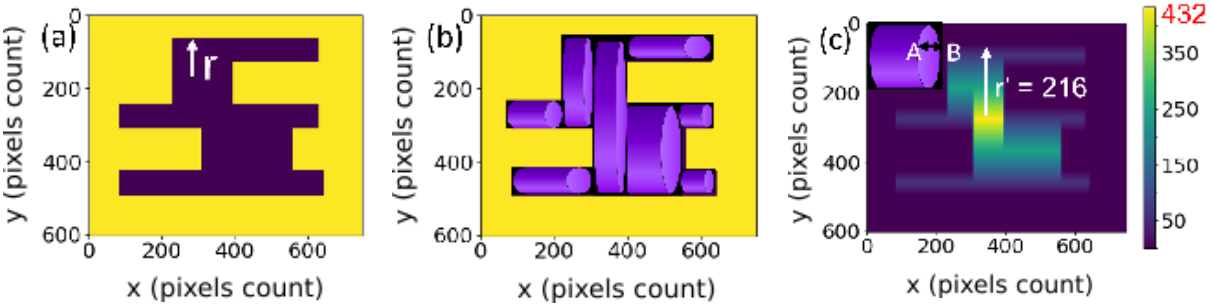

Figure 3: a) An example of a 2D image projection. b) Image 3D reconstruction based on cylindrical shapes. c) 3D profile of a dendrite local height[9].

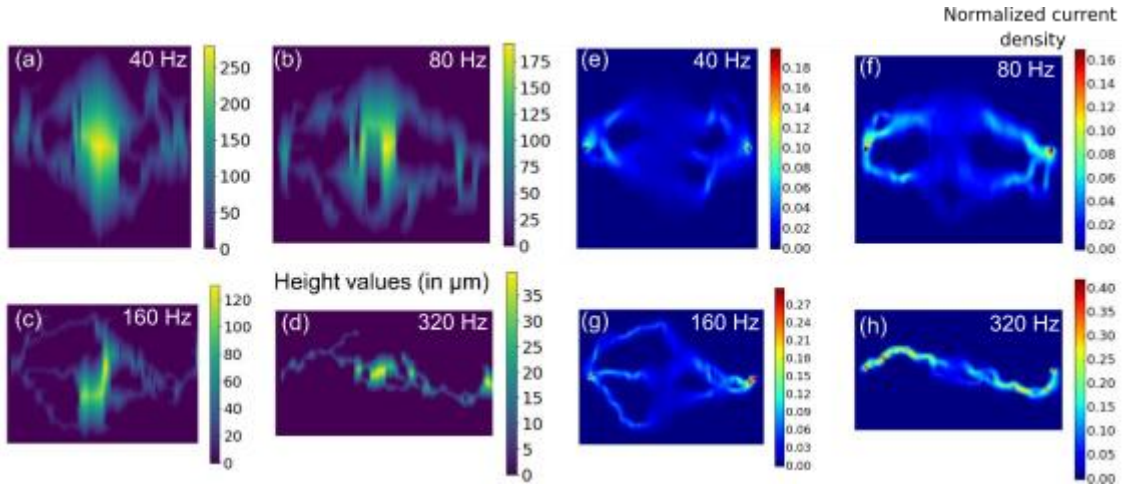

Figure 4: a-d) 3D profiles of dendrites based on multiple cylinder evaluation and corresponding e- h) normalized current density map for the dendrite obtained at *f* = from 40 Hz to 320 Hz based on image analysis and electrical simulations[9].

First, the theoretical resistance of the resultant network was computed with unit of 1/resistivity. Then, resistivity value for each dendritic morphology based on the ratio of experimental and theoretical resistance values was calculated (**Figure 5**).
Finally, from the 3D reconstructed dendrite images, the current density map was obtained (**Figure 4 e-h**).

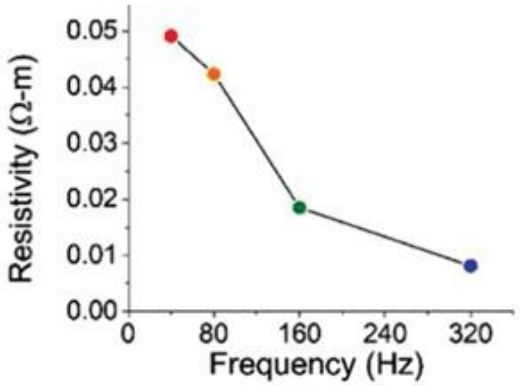

Figure 5. Calculated resistivity values derived from the ratio of experimental and image's computed resistance values for dendritic structures produced at different frequencies[9].

Resistivity calculation exhibited opposite trend to conductance (**Figure 2c**). Namely, as an intrinsic property, higher resistivity (lower conductivity) was shown by low *f* (40 Hz) dendrites, whereas high *f* dendrites (320 Hz) with lower volume and less branching degree demonstrated a drop in resistivity (high conductivity). Such tendency can be associated with an increase of the dendrites' effective section at the macroscale (that is directly related to number and width of branches) when *f* is diminished. Additionally, such behavior could be associated with different organizations and compositions of the PEDOT:PSS domains resulting from various electropolymerization conditions.
Therefore, through method of bipolar current electropolymerization, diversity of intrinsic electronic properties can be introduced on a material level that consequently allows enriching a field of device engineering.

1.3 Transfer characteristics

In order to test the ability of dendrites to act as OECT, transfer characteristics were studied. As previously mentioned, any mechanical handling such as removing dendrite from the drop, adding or sucking out electrolyte, or even evaporation of the drop can lead to collapsing of polymer structure. For this reason, all the measurements were implemented inside the former environment where BQ, HQ, EDOT electroactive species are still presented. Therefore, in order to avoid redox processes during characterization in the electrolyte and the presence of faradaic current, oxidation and reduction potentials of additional species were taken into account **(Figure 6).** For this purpose, Cyclic Voltammetry examination was made individually for every single component of the electrochemical system. EDOT oxidation reaction and BQ reduction reaction occurred at potentials of 0.816 and -0.105 V vs. Ag/AgCl respectively.

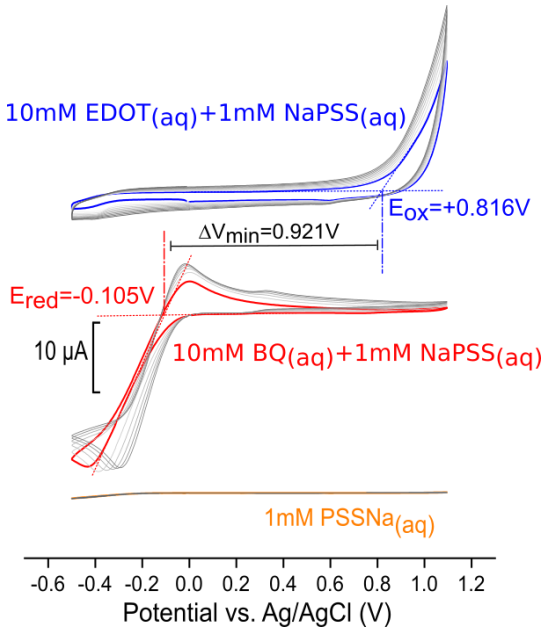

Figure 6. Cyclic Voltammetry curves made in two Au wire electrochemical system with PSSNa only (orange line) and individually in the presence electrochemically active species 10 mM EDOT (blue line), 10 mM BQ (red line).

Therefore according to the results of Cyclic Voltammetry, parameters of I_D-V_G measurements were adapted by applying a small voltage (V_{DS} = 10 mV) and suitable V_G dynamical range from -0.12 V till 0.12 V to avoid oxidation of EDOT and to measure ionic gating only of the PEDOT:PSS fibers.

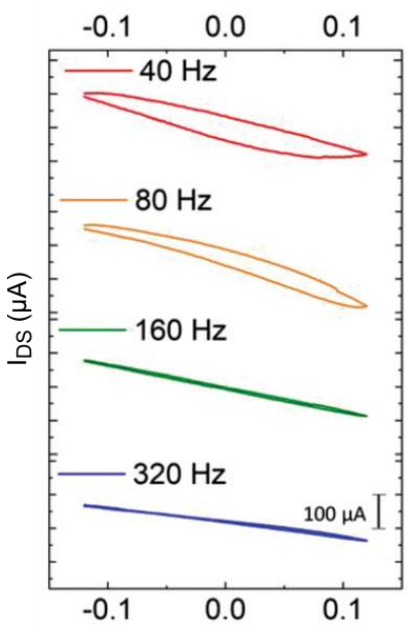

Figure 7. Transfer characteristic of the dendritic OECTs in accumulation and depletion mode at negative and positive V_G, respectively. V_G was cycling from -0.12 V to 0.12 V while maintaining V_{DS} at 10 mV [9].

In our system, to calculate the I_{DS} current modulation in dendritic channels and analyze only the electronic response of the device, a correction factor α was introduced to compensate for the nonequivalence of the voltage distribution between source and drain. SD current modulation in the dendritic channels was calculated by subtracting the measured gate current according to the formula

$$I_{DS}=I_D+ \alpha*I_G \quad (1)$$

where I_D and I_G are measured drain and gate current values, respectively, and the correction factor α equals 0.5, considering that I_G splits in half between comparable parts of the dendritic structures. Transfer curves **(Figure 7)** showed that all tested dendrites morphologies can exhibit effective OECT behavior. Source-Drain current characteristics of channel can be modulated upon influence of gate bias. Moreover, dendritic fibers are capable to operate in both depletion mode in the positive polarity and accumulation mode in the negative polarity.
Such behavior can be associated with partial doping level of PEDOT with PSS^-. Thus, one may assume that the applied frequency value affects not only the material geometry, the number of branches, and thickness, but also may cause changes on the microstructure level, leading to variations in conductivity at different *f*.

1.4 Transcoductance of dendritic OECT

As previously mentioned, OMIEC materials are capable to support electronic charge transport along polymer chains and at the same time perform ionic transport through the material bulk. Therefore, efficient performance of OECT is defined by these two main phenomena, namely efficient electronic transport and facile ion injection to maintain high capacity. Combination of these characteristics, the effective electronic mobility (μ) and volumetric charge storage capacity (C^*) that governs the transcoductance (μC^*), can be used as the materials/system figure-of-merit to evaluate the steady-state OECT performance.
C^* is a total electrical capacitance of the OMIEC material and is related to the ions penetration in the polymer structure, and the ability of the conjugated system to store and collect electronic charges. (i.e., a total capacitance that is proportional to the quantity of ions which are injected or repealed at a certain gate potential).
Thus, to verify performance of dendritic OECT, examination of transconductance was conducted.

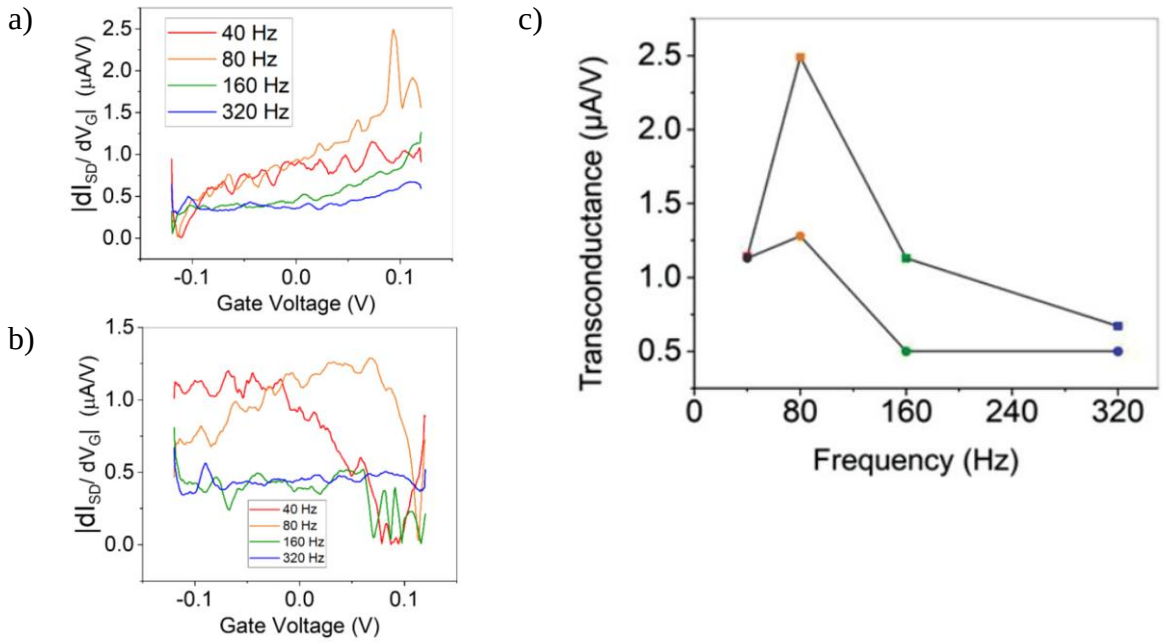

Figure 8. Variation in the derivative of source-drain current with the applied gate voltage during the (a) increasing and (b) decreasing values of the gate voltage. c) Maximum of transconductance values for the forward (square symbols) and backward (circle symbols) current sweeps at V_G = 0 V [9].

Through smoothing I_D–V_G curves with Savitzky-Golay filter and further applying first order of derivative, we build transconductance graphs (g_m) for both forward and backward current sweeps (**Figure 8 a-b**). For more precise comparison the transconductance values at V_G = 0 V were extracted. Non-monotonic behavior of these transconductance values for both current sweeps was observed (**Figure 8 c)**. Thus, it was figured out that tuning electropolymerization condition, namely frequency in this case, and topology along with it, one can modify the transconductance of the channel. Possible hint to understand it can be through decoupling g_m parameters and comparing them with geometry of dendrites and previous results on electrical characterizations and conductivity simulations.

In dendritic fibers, an increase of bulk capacitance C* would be directly related to lowering of *f* due to higher material amount. If capacitance only is considered, one should expect gradual raise of transconductance with reduction of *f* and concomitant dendritic morphology enlargment. Nevertheless, this trend was observed only for high-*f* grown dendrites from (80 Hz to 320 Hz). To the contrary, 3D electrical modeling exhibited opposite trend: a decrease in conductivity associated to a decrease in *f*. This can be interpreted as a decrease of mobility μ at aforementioned conditions, which consequently induce a drop of transconductance.

Ultimately, both *C** and μ were affecting transconductance but in opposite directions that lead to the nonmonotonic evolution. Therefore, as result of *C** and μ competition, at low *f* (more precisely at 40 Hz) transconductance was primarily defined by effective mobility and consequently restrained by low conductivity, while at higher *f* (from 80 Hz to 320 Hz), the transconductance was mainly governed by capacitance.

Overall, utilizing the bottom-up possibility to develop dendrites, one can induce a different contribution of volumetric capacitance and electronic mobility in different morphologies, therefore programming on a structural level a variety of transconductance (conductivity) values. On top of it, one should remember that conductivity is related to charge carriers' mobility. Therefore, by modifying the conductivity of a PEDOT:PSS channel under influence of various

gate voltages (that as well can be presented as a heterosynaptic plasticity mechanism), the transconductance of the channel will be tuned also as a result of purely electronic effect.

2. Introduction of neuromorphic properties with dendritic OECT

2.1 Short-Term Memory Effect

Based on the ability of OMIECs to accumulate ionic charges in their bulk, their volumetric capacitance has been used in OECTs to mimic different biological synaptic functions like short- term, long-term memory effects. Here, using the non-ideal capacitive response of dendritic OECT, replication of short-term plasticity with such architecture is proposed.
A synapse is the junction existing between two neurons that conditions the transmission of an incoming signal from one neuron to be sent to another one. Action potentials is one type of information features neurons carries through their signaling. Such action potential in presynaptic neuron cause the release of neurotransmitters from synaptic vesicles into the synaptic cleft. Neurotransmitters will then connect to receptors at the plasma membrane of the postsynaptic neuron and produce the postsynaptic current (**Figure 9 c**).
Similarly, in an OECT, monopolar spike voltages emitted at a gate electrode and received on an OECT channel can affect its conductance and thus fairly model action potentials and synapses. Analogously, the phenomenon of the electrochemical doping and dedoping inside the OECT channel presented by voltage-controlled injection and extraction of ions can be compared to the neurotransmitter release and uptake at the synaptic cleft[10,11].

For mimicking STP function, the same setup as for transfer characteristics measurement was utilized. In this case, analogously to biological synapse, an Ag/AgCl gate electrode was used as pre-synaptic input while a dendritic channel supported by their source and drain electrode wires emulated a postsynapse. Single gate pulses lasting for ten seconds in the range from - 0.4 V to 0.4 V were applied from the gate to mimic presynaptic signal. At the same time constant voltage of 0.1 V was applied from source-drain to record source–drain current (I_{DS}) that was interpreted as a postsynaptic output signal.

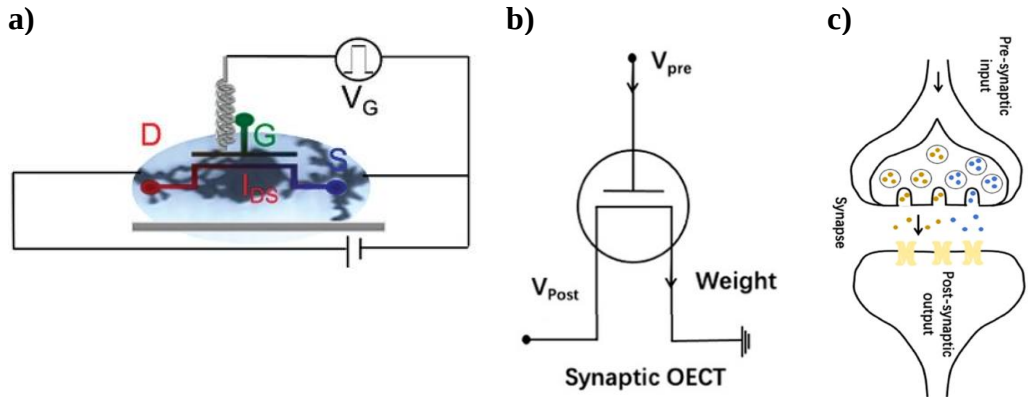

Figure 9. a) Setup for demonstration of short-term plasticity effect for different dendritic morphologies. Single square-shaped pulses with duration of ten seconds were applied from the gate while continuous recording of 0.1 V occurred in between source–drain[9]. b) Schematic electrical diagram of dendritic OECT in analogy to a c) biological synapse[6].

To extract the electronic current out of the current response of the device, gate current was subtracted from the SD recorded current in each experiment.

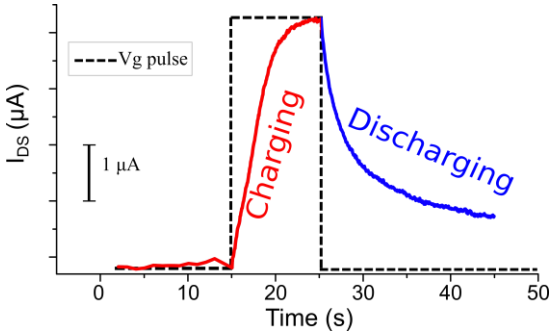

Figure 10. Typical SD current response to a square shape pulse with corresponding charging and discharging processes[9].

As a result, reversible current change appeared in response to applied variety of gate pulses (**Figure 10**). Every single dendrite exhibited specific temporality in charge/discharge magnitude and asymmetry related to doping/dedoping processes, as evidenced by different recorded SD current shapes.

Because dendritic OECT can be operated in both accumulation and depletion modes, it was possible to mimic both potentiation (at negative gate pulses) and depression (at positive gate pulses) regimes which were induced through doping and dedoping processes respectively.

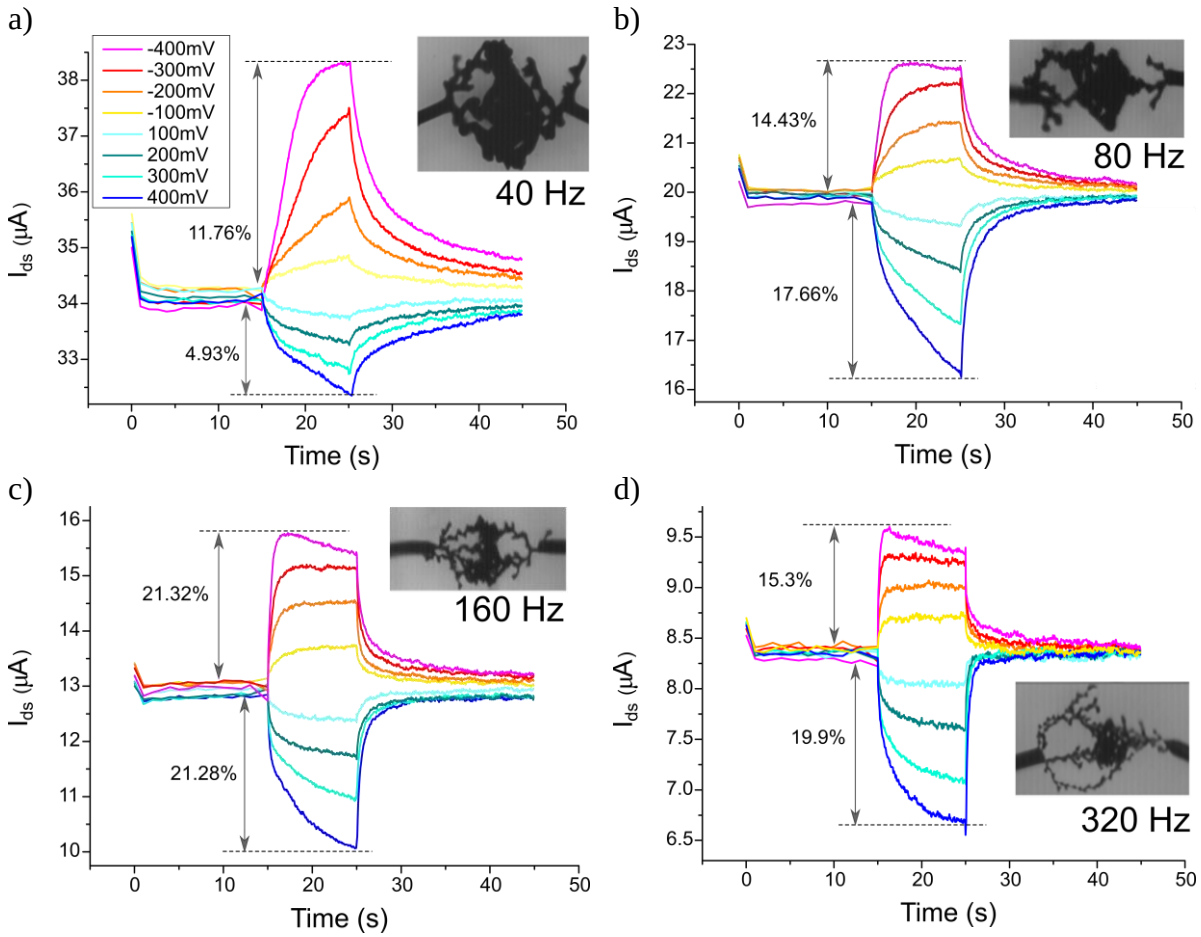

Figure 11. Short-term plasticity effect demonstrated by various dendritic topologies. Source–drain current responses of dendritic OECTs obtained at a) f = 40 Hz, b) f = 80 Hz, c) f = 160 Hz, d) f = 320 Hz to gate pulse stimulation applied from -0.4 V to 0.4 V with step of 0.1 V. Potentiation (depression) is observed at negative (positive) gate voltages. Conductance modulations were calculated with respect to their initial conductance level. Adapted from [9].

Figure 11 shows that every single dendrite differs in terms of STP response. Moreover, non- symmetrical current responses have been observed for low f dendritic OECTs for both positive and negative V_G pulses pointing to a non-equal conductance modulation (ΔG). ΔG induced by the highest $|V_G|$ pulse was calculated with respect to the baseline for every single STP response. For example, high f dendrites showed relatively symmetrical response like in case with 160 Hz, in which ΔG at potentiation and depression appeared as 21.32% and 21.28% respectively. In contrast, at low f (40 Hz) ΔG showed a change of 11.76% during potentiation induction, while the current modulation during depression induction was 4.93%. Such asymmetrical behavior can be related to partial doping of the PEDOT material and explained by the following hypothesis.

Conductance modulation depends on the number of ions that is drawn in and out of the material. Therefore, one can assume that each individual dendrite contains a certain amount of PSS^- that affects the level of doping. In other words, depending on the amount of PSS^- within the dendritic structure, a different number of ions can be inserted and taken out, which ultimately affects the STP response. Hence, considering ΔG, one can judge about the amount of PSS^- inside certain dendrites, level of material doping and how deep the electrochemical doping or dedoping of the channel can be carried out. Interestingly, the obtained patterns correlate to modeling results

according to which a lower conductivity and correspondingly lower doping level is more inherent in bulkier low-*f* dendrites (**Figure 11a**).
In contrast, high-*f* dendritic OECTs displayed comparable profile responses in magnitude at both positive and negative voltage ranges. These were matching with modeling statement as well: higher conductivity is more characteristic of high *f* and smaller in size dendritic structure. Therefore, taking into account all different current modulation, one may conclude that every single dendritic OECT contains different densities of PSS^- in the channel's bulk. Therefore, modifying initial conditions of electropolymerization is an versatile technique to achieve various chemical composition of PEDOT:PSS for such electrochemical devices.

Additionally, the nature of doping mechanism presumably can differ from its thin-film OECT analogs. In most PEDOT-based OECT devices, doping is quite often emerges from anions insertion into the active PEDOT material. In the case of dendritic PEDOT OECTs, doping mechanism is more likely to occur as a result of positive ions removal that are inherently present in the dendrites to balance electroneutrality with PSS^- that does not support fully the PEDOT doping. Injection of negative PSS^- ions in the bulk of dendrites is less likely to take place due to large molecular weight of PSS^- chain. However, it cannot be completely excluded without further analysis.
Another important feature is the non-monotonic charge/discharge temporality upon influence of high negative gate bias (at V_p = -0.4 V) that was observed for dendrites grown at 80 Hz, 160 Hz, 320 Hz (pink colored lines on **Figure 11 b, c, d**). I_{DS} curves obtained for aforementioned structures exhibited not only increase of current but as well its decrease after a certain time of V_G pulse stimulation. The reason for such behavior can be another competitive phenomenon beside the gating effect that occurs at $V_p < -0.3$ V and induces a current decrease at t_p (time of applied pulse) above one second. Possible explanation for such nonlinear pattern can be found at molecular level, the reason can be a Faradaic processes occurring due to the presence of benzoquinone (E_{red} = - 0.105 V vs Ag/AgCl) and hydroquinone (which was generated upon dendritic growth). On the other hand, it can be connected to phenomenon at the material level, namely to electroactivity of PEDOT:PSS and mechanical capabilities to stretch or shrink under the voltage polarity. Interestingly, same nonmonotonic behaviour was revealed for biological synapses during the short-term plasticity[12] and this phenomenon has not been observed in discrete electrostatic capacitor elements.

All these results showed that dendritic OECT, especially in combination with an electrolyte, can exhibit a diversity of complex electrochemical responses and so expand a range of possible tools and strategies for simulating complex biological synapses' dynamics.

2.1.1 Time constants

To assess the short-term memory impact for each dendritic OECTs, the temporal signature of both charging and discharging processes were examined. Taking the branch width variation into account, variable local capacitances can be expected from dendritic OECTs. Since the geometry of morphologies is not uniform, the whole structure, as noted in the modeling part, can be represented as multiple joined cylinders, or, in other words, as a distribution of elemental capacitors, implying that each elementary cylinder has its own elemental capacitance value.

This distribution of elemental capacitors influences the total capacitance and correspondingly affects the time scale of charging and discharging processes in dendritic OECTs.

To evaluate this effect connected to different capacitances of dendritic objects, the time responses of each dendritic OECT were examined through the fitting of the "charging" and "discharging" parts of the STP curves (**Figure 10**) by taking an exponential function. After the application of a gate pulse with negative voltage, the rise time of the recorded Source-Drain current pulse is identified as the charging time constant, and the decay time of the same recorded current pulse is defined as the discharging time constant. Under the influence of a gate pulse with positive voltage, this identification is reversed: the decaying part of the SD current defines the charging time constant, and the rising part of the current pulse identifies the discharging time constant.

For both charging and discharging time constants in the range of V_G pulses from -0.4 V to +0.4 V, decreasing *f* leads to an increase of time constant values throughout the whole range of applied V_G pulses (**Figure 13**). The bulkier and bigger are the dendrites, the longer it requires to fully dope or dedope the polymer, and the opposite for thinner structures. Such type of behavior is associated to a higher ionic capacity of voluminous and branchy morphologies and a lower ionic capacity of thinner and less arborized dendrites.

No other tendency was noticed except for the lowest *f* at 40 Hz one, which revealed distinct dynamics for charging at positive and negative voltages. For dendrites grown at low frequencies, non-symmetrical behaviour upon influence of positive and negative gate pulses was clearly seen.

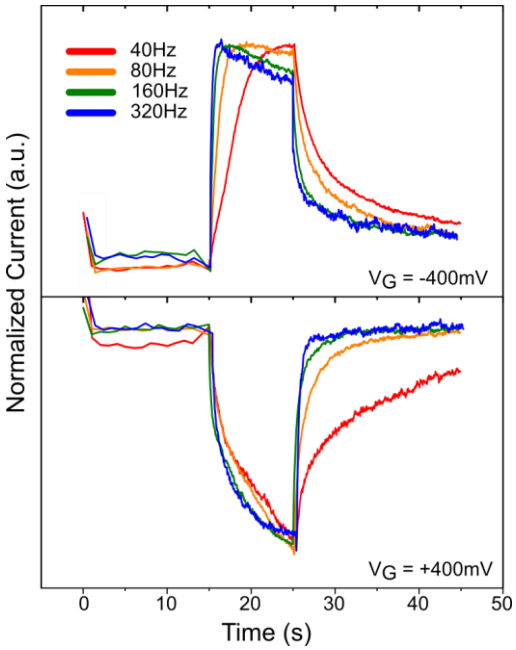

Figure 12. Comparison of normalized source–drain current responses of dendritic OECTs grown at 40 Hz, 80 Hz, 160 Hz, and 320 Hz at V_G = 0.4 and V_G =-0.4 V [9].

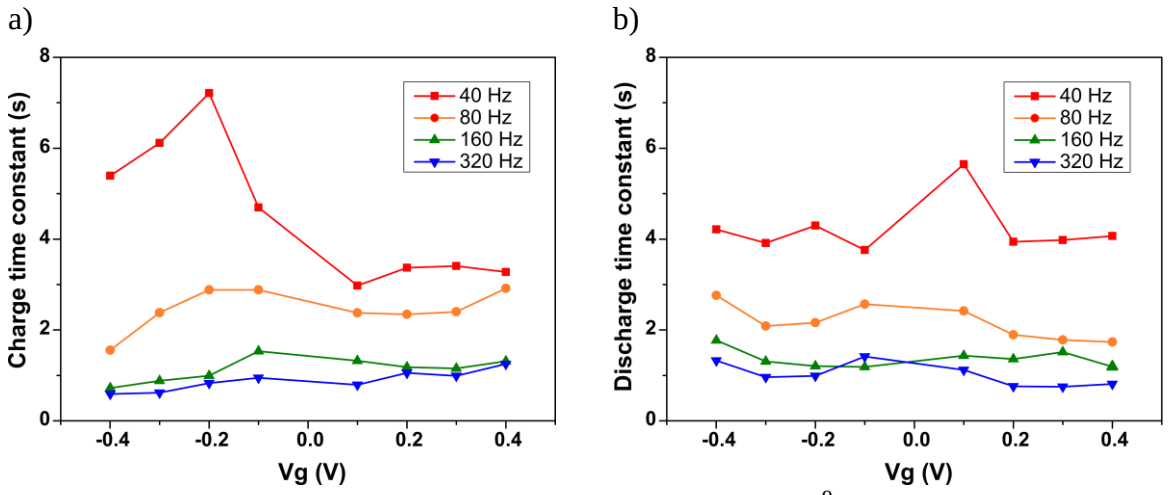

Figure 13. Variation in time constant of charging/discharging regions [9].

For time-constant evaluation, the capacitance of the dendrite, which considers the surface and volume of a structure, should also be taken into account. It is because the change in effective capacitance can impact the charging/discharging time constant. For example, in high *f* dendrites due to thin geometry doping is mostly carried out because of ions' interaction with available surface area and is less likely due to deep insertion of ions inside the structure of the dendrite. So, doping of thin high *f* dendrites will be less hindered and it will require less time for this process, implying lower charge time constant.

In contrast, for bulkier structures, apart from the area parameter, the volume of material plays a role as well. Once ions are on the surface, further insertion into the bulk of material occurs, and this process can be kinetically limited. So, it would require a longer time for ions to move in the polymer bulk, leading to a higher charge time constant. Similarly, once ions are stabilized within the material, it is harder for them to be removed and consequently would require a longer time for it, which is corresponding with higher discharge time constants for low *f*.

Thus, bearing aforementioned in mind, various dendrites' geometry can affect the charging or discharging dynamics. For low *f* (i.e. bulky dendrites), the whole doping/dedoping processes are more hindered to carry out than for high *f* (i.e. thinner branches). Therefore, the processes of doping/dedoping are better promoted for thinner structure, since ions are still interacting with the dendrite when accumulated at the polymer surface.

Thus, in the specific case of a dendritic OECT, shape and geometry of the dendrite yields the transistor electrical behavior by affecting the doping/dedoping kinetic in the material.

Overall, utilizing dendritic tuning, various short-term responses can be programmed and may serve as a promising tool for synaptic plasticity engineering. For example, in reservoir computing, different time scales of dendrites can be used to record the time history of temporal signals required for effective classification[13].

2.1.2 Power consumption

Since power consumption play a significant role in programing and developing neuromorphic devices, the recorded gate current served to evaluate energy consumption during STP programming.

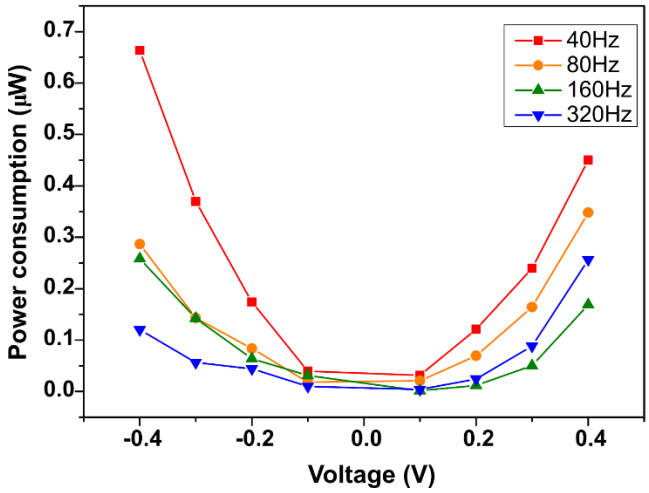

Figure 14. Power-consumption of dendritic OECTs grown at 40 Hz, 80 Hz, 160 Hz, 320 Hz at V_G pulses applied from -0.4 V to 0.4 V [9].

Energy consumption was evaluated through standard formula P=E/t, where t was taken as ten seconds during pulse facilitation and energy E was calculated according to E=V*Q (where V is voltage and Q is charge), by multiplying the applied gate voltage amplitude to the maximum charge value. The charge Q was estimated through applying integration function to recorded I_G current and further extraction of the charge value.

As it can be seen from **Figure 14,** energy consumption was directly correlated to the macroscale geometry of the dendrites. Bulkier and more voluminous dendritic structures (obtained at 40 Hz and 80 Hz) require more energy to operate than thinner ones (electropolymerized at 160 Hz and 320 Hz).

The energy consumption trend is not symmetrical with the applied voltage for any of the structures. For negative voltages, decrease or increase of power consumption tendency gradually follows the geometrical features of objects. For positive voltage, pattern is remained except the fact that dendrites obtained at 160 Hz demand less energy in comparison with all other structures.

Additionally, **Figure 14** shows that one can operate dendritic OECT at low voltages (0.1 V, - 0.1 V), which is promising for production of organic neuromorphic devices capable of functioning at relatively low energies. However, the change in conductance, and therefore synaptic weight, in these conditions is low too. On the other hand, by applying higher voltages, much more control over conductance (synaptic weight) can be achieved, but it will require more energy. Hence, the question of finding a proper dendritic morphology with proper efficiency and low energy consumption is still debatable. One of the possible strategies to overcome this challenge would be to consider the capacitance of a dendrites, according to Q=C*V, where C is the capacitance. Specifically, by reducing C, for example through scaling down the dendrite

geometry, less charge will be required for such device operation. It consequently will result in less energy consumption but allow at the same time to maintain the efficiency of the device.

2.2 Long-Term Memory Effect

Previous experiment showed that it is possible to mimic homosynaptic plasticity (precisely STP) with dendritic OECT. Nevertheless, as it was pointed in Chapter 1, the most attractive devices for neuromorphic engineering are those capable of mimicking heterosynaptic plasticity. Heterosynaptic plasticity involves an additional controlling condition in the form of a brain cell (like an astrocyte, for example) to supervise an already existing connection. On hardware level, it allows to program multi-level conductance states by utilizing a supplementary terminal.
One of the types of heterosynaptic structure in biological neural networks includes astrocytes. Astrocytes are cells that play an essential role in memory functioning and LTP processes[14].

2.2.1 Long-term plasticity in neuroscience

As mentioned above, long-term plasticity (LTP) is a specific form of activity-dependent synaptic plasticity showing how repeated stimulation contribute into long lasting enhancement in signal transmission between two neurons and form the cellular basis of memory formation[15].

LTP includes processes of long-term potentiation and long-term depression, which are based on the following mechanisms. Presynaptic cell is filled with glutamate neurotransmitter that can be released into the synaptic cleft after presynaptic stimulations (action potential)[16]. On the other side of a synapse, membrane of postsynaptic cell contains α- amino- 3- hydroxy- 5- methyl- 4-isoxazolepropionic acid (AMPA) and N- methyl- D- aspartate (NMDA) glutamate receptor channels. After stimuli application, neurotransmitters are released from the presynaptic neuron. Glutamate, by binding with APMA and NMDA receptors of a postsynaptic neuron, promotes permeability of these receptor channels for Na^+ ions presented in extracellular solution. In turn, NMDA receptor is permeable not only for Na^+ but also for Ca^{2+}. However, NMDA is blocked by Mg^{2+} ion that prevent penetration of Na^+ and Ca^{2+} ions through the receptor inside postsynaptic cell (**Figure 15a**).
When low frequency signals propagate to post cell, a small amount of neurotransmitters will be released and an accordingly small quantity of Na^+ will go through AMDA channel that will lead to slight depolarization (small increase of voltage) of postsynaptic cell. When a high-frequency action potential travels down the presynaptic cell a bigger quantity of neurotransmitters will be released. Consequently, AMDA receptors will be open longer and more Na^+ will move inside post cell. This increased amount of Na^+ causes an augmented depolarization effect in the postsynaptic membrane that repeals Mg^{2+} out of the NMDA receptor via electrostatic repulsion. This newly opened channel rises the flow of Na^+ and allows complementary Ca^{2+} ions to penetrate inside the post cell (**Figure 15b**). Presence of Ca^{2+} activates many secondary intracellular mechanisms.

For example, protein kinase in postsynaptic neuron interacting with Ca^{2+} provoke addition of phosphate group (phosphorylation) to AMPA channels and so contribute to their ability to uptake Na^{+}. Apart from this, phosphorylation process allows to insert additional AMPA channels on the post cell membrane (**Figure 15c**).
Therefore, as a result of high frequency stimulation, boosted efficiency of receptors to uptake ions and increased amount of AMPA receptors allows better ion penetration into the post cell.
Since every single action potential causes depolarization and consequently appearance of excitatory postsynaptic potential (EPSP), at high frequency stimulation summation of EPSP will result in signal with higher amplitude in comparison with initial ones, causing, therefore, long-term potentiation (LTP).

As counter-effect apart for protein kinase, postsynaptic cell contains protein phosphatases as well, which has higher affinity to Ca^{2+} than kinases. At lower Ca^{2+} concentration, the protein phosphatases binds with Ca^{2+} that in turn will lead to withdrawal of phosphate group from AMPA receptors and consequent reducing amount of Na^{+} flowing into the post cell. So, small amplitude or not frequent stimulation results in negligible amount of neurotransmitters released out of post cell and therefore minor influx of Ca^{2+} that hence will be tied with phosphatases rather than with kinesis. Decreased flux of ions eventually issues in long-term depression process that can be evidenced as decrease in amplitude of postsynaptic potential and diminishing in synapse strength.
Nevertheless, sufficient amount of Ca^{2+} allows overpowering in phosphatase and activates kinase protein leading to constant flow of ions and long-term potentiation[17,15].

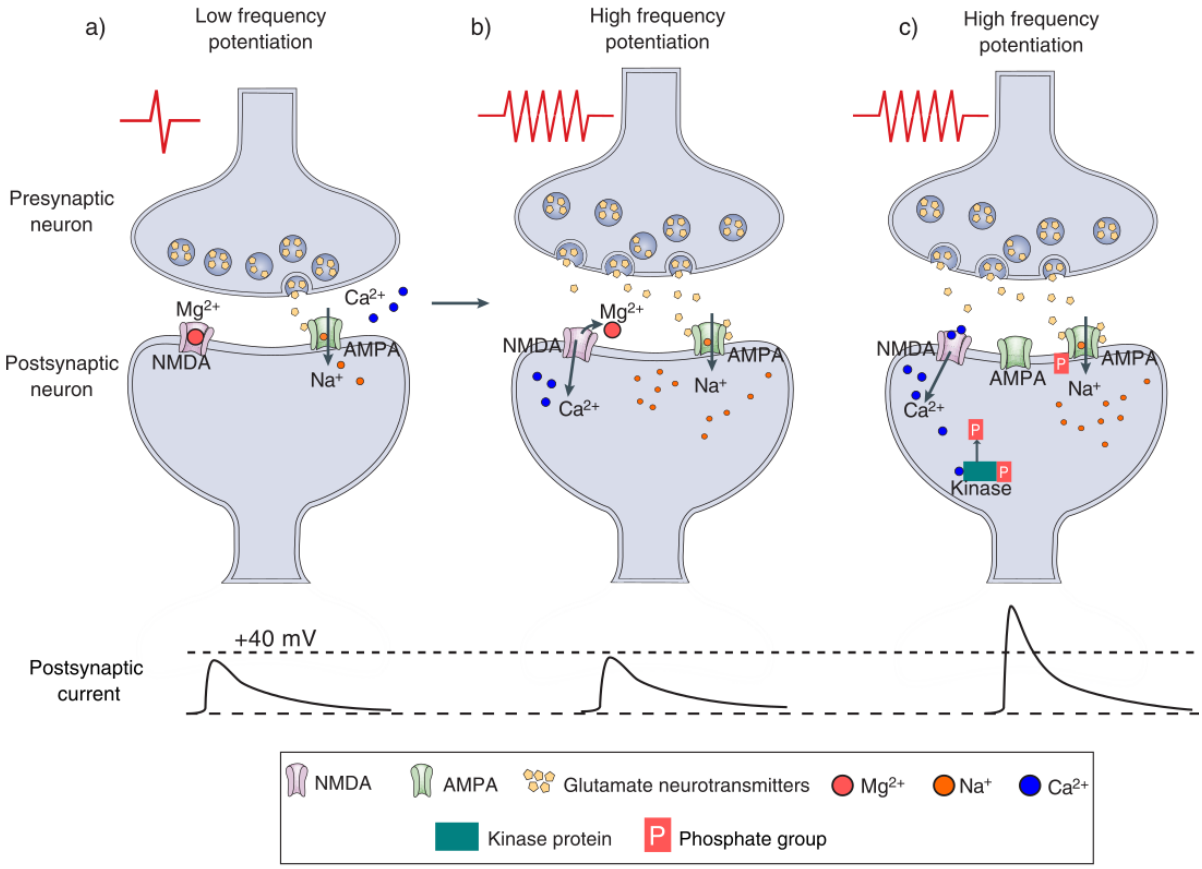

Figure 15. Molecular mechanisms of long-term synaptic potentiation between pre and post synaptic neurons. a) Released under influence of presynaptic potential neurotransmitters enhance permeability of AMPA receptors for Na^+. b) Caused by high frequency potentiation increased number of Na^+ ions inside the postsynaptic neuron provoke repulsion of Mg^{2+} out of NMDA receptors that allow Ca^{2+} ions to flow in the post cell membrane. c) Ca^{2+} ions interacting with protein kinase improve ions permeability through receptors and induce new AMPA receptors. d) Example of postsynaptic current evolution starting from low frequency to high frequency potentiation. Adapted from [18].

2.2.2 Astrocyte cells

Apart from neurons, mammalian brain consists also of glia cells. One of the glial cells subtypes are astrocytes that have been considered to maintain only supportive functions for neurons[19]. However, over past decades, it was disclosed that astrocytes play an essential role in synaptic plasticity regulation. Astrocytes control removal of dendritic spines, synapse formation, and regulate neurotransmission and plasticity[20].

Plasticity modification induced by astrocytes is achieved through the control of neurotransmitter concentration. During signal transmission between neurons, glutamate neurotransmitter released from presynaptic cell activates metabotropic glutamate receptors on astrocytes, leading to an increase of Ca^{2+} ions within this glial cell and a subsequent release of glutamate by astrocytes. This additional portion of released astrocytic glutamate (gliotransmitters) induce activation of presynaptic and postsynaptic glutamate receptors and as a result modify synaptic transmission **(Figure 16)** [21]**.**

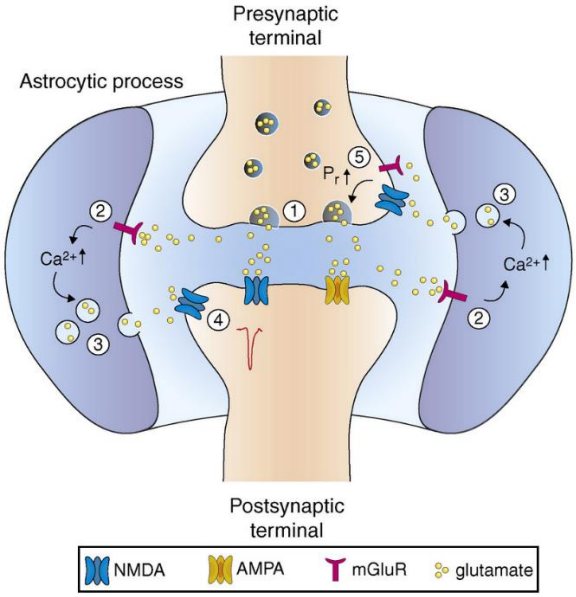

Figure 16. Representation of signal transmission between neurons, modulated by an astrocyte. Presynaptic potential provokes release of neurotransmitters from the presynaptic neuron (1). In turns, it activates astrocytic metabotropic glutamate receptors (mGluRs) leading to a rise in Ca^{2+} ions in the astrocyte (2) and following after the release of gliotransmitters. These gliotransmitters act back either on: postsynaptic neuron by empowering excitability of the terminal through NMDAR receptors and so synchronizing neuronal activity (4), or on receptors of presynaptic neuron thereby increasing transmitter release probability (Pr) (5) [21].

Bernardinelli and colleagues showed that the induction of synaptic plasticity at high frequency (during LTP) provokes astrocyte to extend towards and enwrap the active synapse, thus amplifying the induction of synaptic plasticity and long-term stability of the potentiated synapse (**Figure 17)**[22]**.**

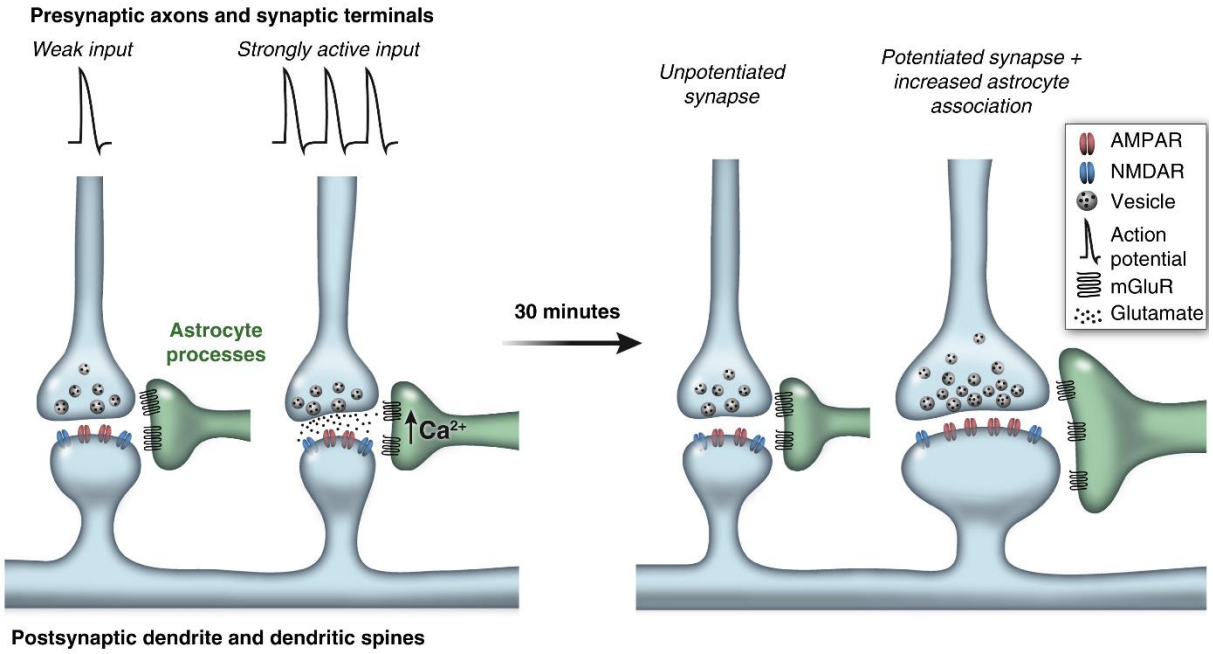

Figure 17. Astrocyte influence on active and weakly active synapses. Strong synaptic activity as for example in case with LTP (right) results in the release of many more neurotransmitters, which are detected by the neighboring astrocyte, leading to an increase in calcium concentration and subsequent release of gliotransmitters that strengthen the synapse and boost dendritic spine in terms of volume. An inactive synapse (left) paired with astrocyte will not exhibit any alteration due to low and not constant amount of neurotransmitters and so astrocyte–synapse interactions will be regulated only at the level of individual synapses[22].

2.2.3 Long-term plasticity induced by means of Ag/AgCl gate

In STP experiments, we considered our system to be only pre and post-terminals. However, for introducing heterosynaptic plasticity, a slight reconfiguration should be imposed. In LTP examination, dendritic junction was considered as a connection of two neurons (as pre and post terminals) and an external Ag/AgCl gate wire was emulating an astrocyte.

In most of conventional OECTs, mimicking LTP is reached through application of high frequency discrete pulses from a gate electrode and consequent accumulation of ions inside the bulk of OMIEC material that is leading to summation effect of signals and increase in amplitude identically to biological neurons. However, to emulate LTP for dendritic system, a different strategy was employed: “write” and “read” operations were decoupled following ENODe principle[23]. This principle is based on the capacity of the gate electrode and channel of the OECT to maintain charges when the electronic circuit (i.e., S, D, and G electrical connections) is in an open-circuit configuration, namely when the gate is open. In this case, electrolyte acts as a barrier for electronic charge transport, keeping the electrode conductance state after the presynaptic potential is applied.

As in the case with STP, the same setup and doping/dedoping principle of the organic dendritic channel was utilized (**Figure 18**).

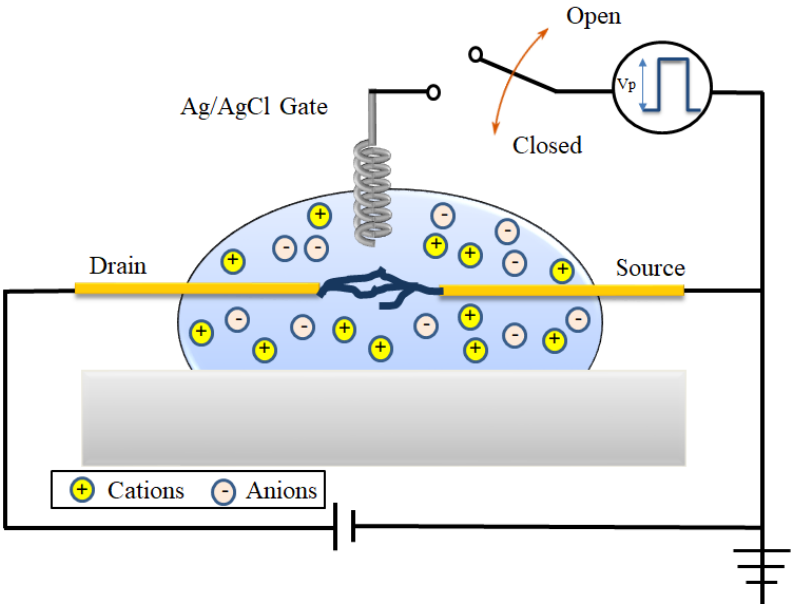

Figure 18. Schematic of dendritic OECT setup for LTP programming where the gate can be physically disconnected and thus "write" and "read" operations could be split.

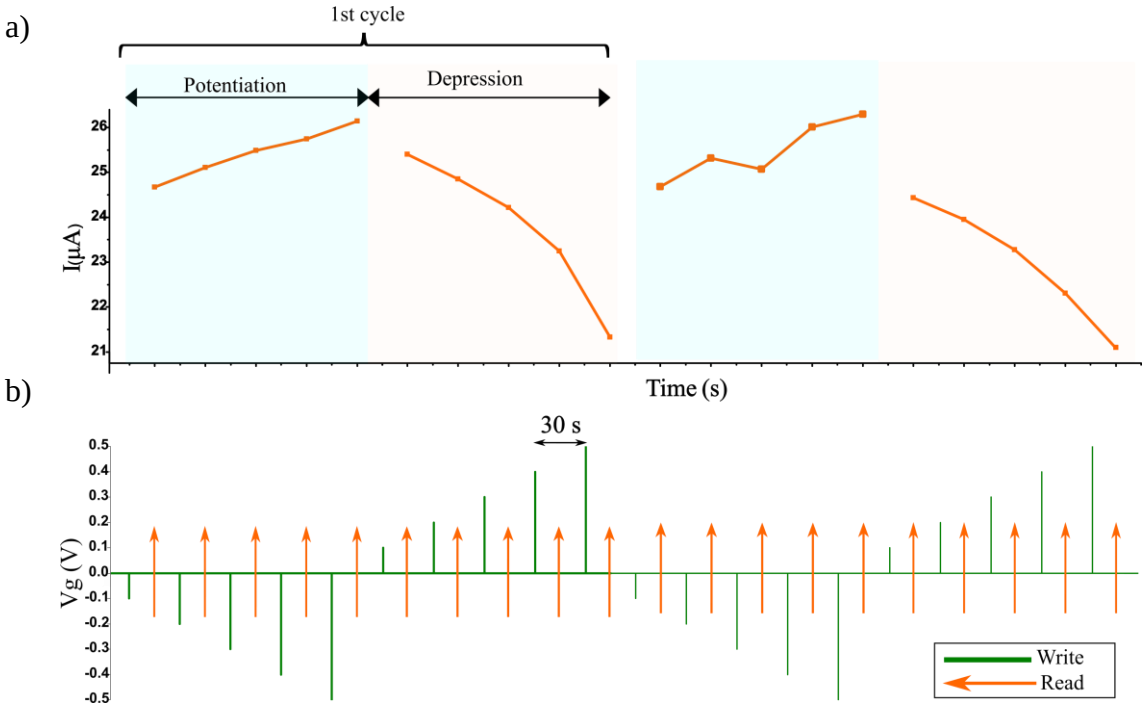

Figure 19. a) Long-term potentiation and depression behavior in dendritic synaptic post-terminal programmed under b) "write" pulses swept from ±0.1 V until ±0.5 V with step of 0.1 V in between.

To mimic astrocyte modulation a sequence of single square shape pulses was sent from the Ag/AgCl gate firstly with decreasing voltage amplitude from -0.1V to -0.5V and after with reversed trend from 0.1V to 0.5V in order to mimic potentiation/depression, respectively.

30s- time interval was hold in between write signals to perform “read” operations and evaluate “synaptic changes”. During this idle time, the gate electrode was physically disconnected from Source-Drain terminals through high impedance switching matrix to avoid electronic charges exchange. Using ability of dendritic channel to store charges, various induced conductance states were recorded. For examination conductance modulation (carrying out read operations) of the dendritic OECT, a constant potential of 0.1 V was applied in between Source and Drain. At such write voltage range (with respect to CV responses of system’s component) it was possible to avoid any oxidation reaction of EDOT (E_{ox} = 0.815 V vs Ag/AgCl) (**Figure 6**) and only reduction of BQ (E_{red} = -0.105 V vs Ag/AgCl) could occur.
As a result, long-term potentiation and depression behaviors were successfully reproduced in the form of conductance evolution shown on **Figure 19.** In this way, system was cycled four times to show reproducible response. A slight relaxation of current noticed in depression regime in between cycles can be caused by leakage in the electronic circuit or additional redox reaction leading to charge compensation.

2.2.4 Long-term plasticity induced by means of dendritic gate

One of the main features of our system is the ability to create bottom-up devices with controlled properties. Thus, it would be interesting to test if one could develop additional dendritic branches in the system with an already existing dendritic bridge. This would provide a new possibility to operate an already existing connection and to induce heterosynaptic plasticity through self-developed polymer branches that may act as gate (thus emulating an astrocyte cell).

Growth of Third Dendrite

For this dendritic channel, mimicking neurons connection was preliminary produced at 5 V_p, 80 Hz, 50% duty cycle and 0 V offset. After the channel formation, to create an “astrocyte” dendrite, the same bipolar signal was applied from the additionally inserted Au electrode while primary dendritic connection was set as a ground. The additional wire was placed at the same height as initial electrodes and set at 240 µm distance from primary dendritic junction (**Figure 20**).

Effective dendritic growth occurred from the Au gate terminal that assign this concept as a promising tool for the development of multiple nodes’ 3D devices. During electropolymerization on a third wire, no significant morphological modifications (increase in diameter, additional branches appearance) on already existing polymer connection was visually observed. Nonetheless, one cannot completely exclude effect of additional electropolymerization since a small outgrowth on SD connection occurred once dendrite gate was approaching it.

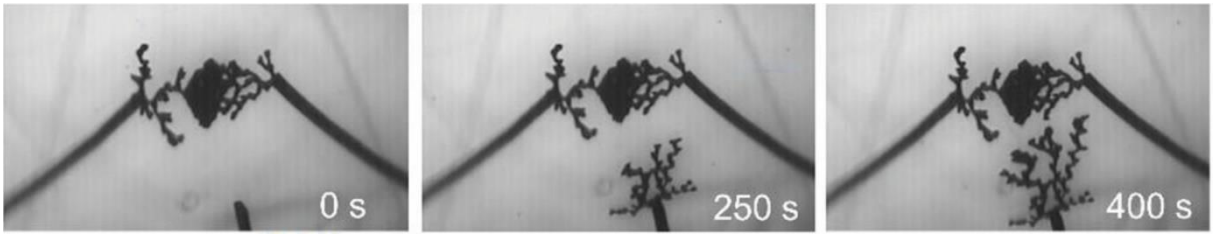

Figure 20. Time-lapse of a third dendrite formation using the AC electropolymerization process at 5 V_p, f = 80 Hz, 50% dc and 0 V_{off} while earliest dendrites are set as ground[9].

To induce long-term memory effect, the same strategy with decoupling "write" and "read" operations was applied. In a similar way, programming relied on applying series of discrete pulses from the new created dendritic gate with voltage sweeping from 0 V to (±) V_G in order to emulate astrocyte potentiation. The "read" command was as well carried out through electrical opening of dendritic gate from the SD terminals and at constant V_{DS} = 0.1 V. It resulted in distinct conductance states referring to every single write event and imitating potentiation and depression (**Figure 21**).

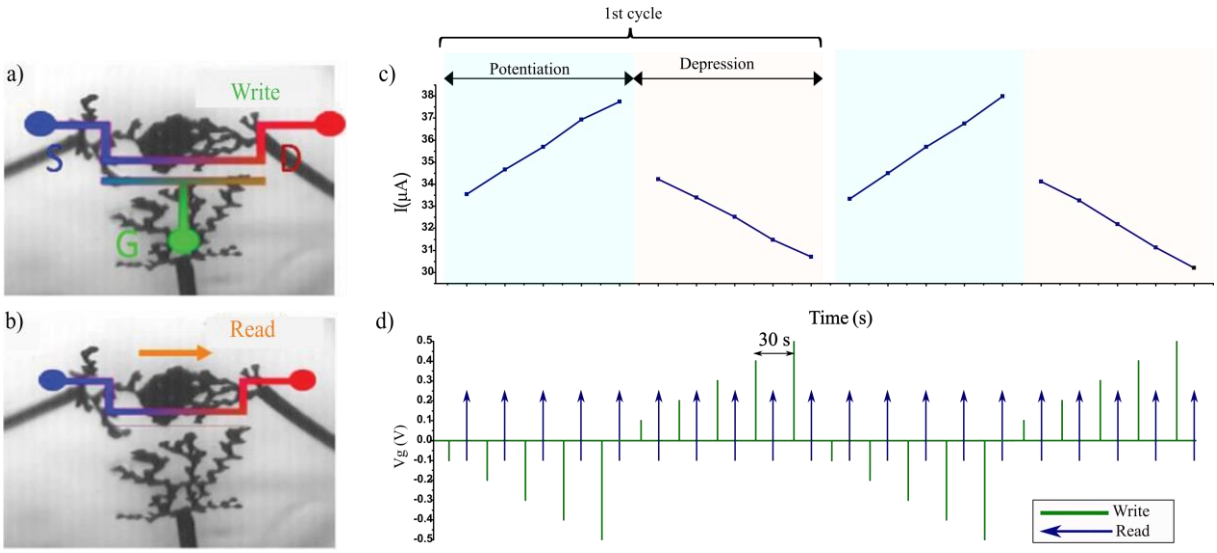

Figure 21. a) Schematic of dendritic OECT programming with positive/negative sweep applied on the gate and following after b) the read operation with disconnected gate terminal.
c) Evolution of the conductance simulating long term potentiation and depression behavior after successive programming induced by d) "write" pulses varying from ±0.1 V to ±0.5 V with step of 0.1 V between them. Adapted from [9].

Therefore, with such ability to create dendritic gates and mimic heterosynaptic plasticity, these bottom-up approach with polymer dendrites can give neuromorphic engineering much more flexibility when it comes to programming and developing new functional units. For example, the system is not limited only by one dendritic connection but another ones can be introduced and they as well can be programmed through the same dendritic gate or different ones.
As well, mean current modulation in potentiation and depression modes for both types of gates was not similar: 14 % for the dendritic gate vs. 5.85 % for the Ag/AgCl gate in potentiation mode;13.3 % for the dendritic gate vs. 16.8 % for the Ag/AgCl gate in depression mode (**Supplementary Figure 1**). Thus, by selecting different gates one can select the level of current

modulation, that would allow modifying conductance of the dendritic connection according to programming needs and consequently set certain synaptic weights.

Discussion

In this chapter, it was discovered that dendrites are conductive objects which conductance values are directly related to the morphology of the dendrite, controlled through AC-bipolar electropolymerization. The joined polymer branches can be presented as a connection between two neurons (synaptic cleft), implying that the various conductance rates can be introduced as synaptic weight.
Additionally, with the help of image analysis, we extracted information regarding conductivity that showed the opposite trend to conductance. It was assumed that such a tendency is related to the organizations and compositions of the PEDOT:PSS domains within every individual structure.
It was shown that all dendrites can act as OECT, in which the Source-Drain current of a PEDOT:PSS dendritic channel can be modulated upon the influence of gate bias. Moreover, dendritic fibers are capable to function in both depletion and accumulation modes, expanding various conditions in which dendritic OECT can be operated.
Through transconductance analysis, it was established that every single dendritic structure could have a different combination of volumetric capacitance and electronic mobility which ultimately results in a variety of dendritic OECT performances.
Finally, we discovered the capability of dendritic OECT to mimic STP. Dissimilar STP behaviors were demonstrated by every single structure obtained at different *f* at positive and negative gate polarization, with correspondingly various charging and discharging time constants. Moreover, non-symmetrical current responses within one single structure were revealed, pointing to partial doping of the PEDOT material and confirming the previous assumption.
Emulating LTP by means of not only the Ag/AgCl gate but as well through the bottom-up developed dendritic gate was successfully implemented. This may give an opportunity not only to use various types of gates but as well to develop local dendritic gate or several of them and carry out programming in a desirable way.
In general, it was shown that PEDOT:PSS dendrites can serve as a promising tool for neuromorphic engineering, which can be developed with respect to operating needs, thereby preventing the saturation of the system with unnecessary connections. It was also demonstrated that dendritic properties (structural and electrical) can be tuned through electropolymerization conditions, in this study through frequency parameter, thus providing a broad range of ways to program and work with these objects.
However, this chapter revealed the ability of dendrites to mimic only synaptic plasticity, which still leaves room to study the facility of dendritic devices to obey other plasticity mechanisms, such as structural one (STDP, SRDP), for instance.

Supplementary information

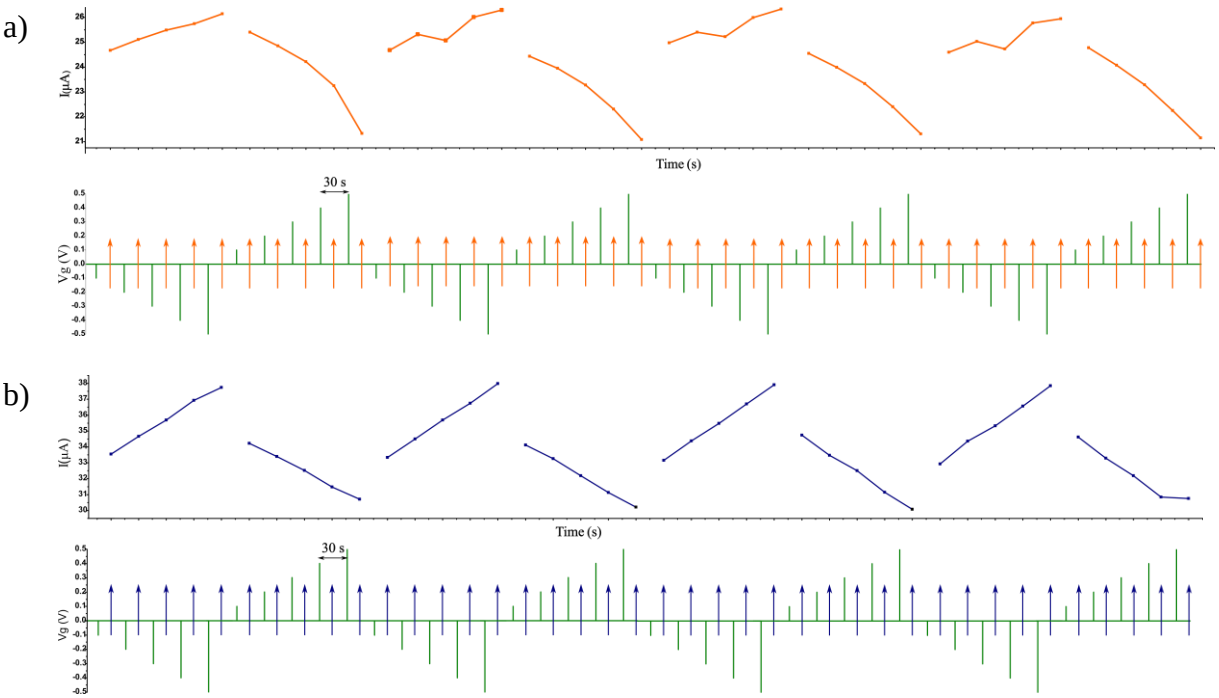

Supplementary Figure 1. Evolution of the conductance simulating long term potentiation and depression behavior under successive programming for a) Ag/AgCl gate and b) dendritic gate during four sequential cycles. The current modulation was calculated separately for the potentiation and depression modes of each cycle in relation to the base level of each individual regime. Then, from these values, the average current modulation occurring during the two aforementioned regimes was calculated separately for both the dendritic and Ag/AgCl gates.

Literature

(1) Rivnay, J.; Leleux, P.; Ferro, M.; Sessolo, M.; Williamson, A.; Koutsouras, D. A.; Khodagholy, D.; Ramuz, M.; Strakosas, X.; Owens, R. M.; Benar, C.; Badier, J.-M.; Bernard, C.; Malliaras, G. G. High-Performance Transistors for Bioelectronics through Tuning of Channel Thickness. *Sci. Adv.* **2015**, *1* (4), e1400251. https://doi.org/10.1126/sciadv.1400251.

(2) Khodagholy, D.; Rivnay, J.; Sessolo, M.; Gurfinkel, M.; Leleux, P.; Jimison, L. H.; Stavrinidou, E.; Herve, T.; Sanaur, S.; Owens, R. M.; Malliaras, G. G. High Transconductance Organic Electrochemical Transistors. *Nat. Commun.* **2013**, *4* (1), 2133. https://doi.org/10.1038/ncomms3133.

(3) Faria, G. C.; Duong, D. T.; Salleo, A. On the Transient Response of Organic Electrochemical Transistors. *Org. Electron.* **2017**, *45*, 215–221. https://doi.org/10.1016/j.orgel.2017.03.021.

(4) Gerasimov, J. Y.; Gabrielsson, R.; Forchheimer, R.; Stavrinidou, E.; Simon, D. T.; Berggren, M.; Fabiano, S. An Evolvable Organic Electrochemical Transistor for Neuromorphic Applications. *Adv. Sci.* **2019**, *6* (7), 1801339. https://doi.org/10.1002/advs.201801339.

(5) Gkoupidenis, P.; Koutsouras, D. A.; Malliaras, G. G. Neuromorphic Device Architectures with Global Connectivity through Electrolyte Gating. *Nat. Commun.* **2017**, *8*, 15448. https://doi.org/10.1038/ncomms15448.

(6) Shu, H.; Long, H.; Sun, H.; Li, B.; Zhang, H.; Wang, X. Dynamic Model of the Short-Term Synaptic Behaviors of PEDOT-Based Organic Electrochemical Transistors with Modified Shockley Equations. *ACS Omega* **2022**, *7* (17), 14622–14629. https://doi.org/10.1021/acsomega.1c06864.

(7) Bernards, D. A.; Malliaras, G. G. Steady-State and Transient Behavior of Organic Electrochemical Transistors. *Adv. Funct. Mater.* **2007**, *17* (17), 3538–3544. https://doi.org/10.1002/adfm.200601239.

(8) Rivnay, J.; Inal, S.; Salleo, A.; Owens, R. M.; Berggren, M.; Malliaras, G. G. Organic Electrochemical Transistors. *Nat. Rev. Mater.* **2018**, *3* (2), 1–14. https://doi.org/10.1038/natrevmats.2017.86.

(9) Janzakova, K.; Ghazal, M.; Kumar, A.; Coffinier, Y.; Pecqueur, S.; Alibart, F. Dendritic Organic Electrochemical Transistors Grown by Electropolymerization for 3D Neuromorphic Engineering. *Adv. Sci.* **2021**, *8* (24), 2102973. https://doi.org/10.1002/advs.202102973.

(10) Ji, X.; Paulsen, B. D.; Chik, G. K. K.; Wu, R.; Yin, Y.; Chan, P. K. L.; Rivnay, J. Mimicking Associative Learning Using an Ion-Trapping Non-Volatile Synaptic Organic Electrochemical Transistor. *Nat. Commun.* **2021**, *12* (1), 2480. https://doi.org/10.1038/s41467-021-22680-5.

(11) Pecqueur, S.; Vuillaume, D.; Alibart, F. Perspective: Organic Electronic Materials and Devices for Neuromorphic Engineering. *J. Appl. Phys.* **2018**, *124* (15), 151902. https://doi.org/10.1063/1.5042419.

(12) Markram, H.; Pikus, D.; Gupta, A.; Tsodyks, M. Potential for Multiple Mechanisms, Phenomena and Algorithms for Synaptic Plasticity at Single Synapses. *Neuropharmacology* **1998**, *37* (4–5), 489–500. https://doi.org/10.1016/s0028-3908(98)00049-5.

(13) Pecqueur, S.; Mastropasqua Talamo, M.; Guérin, D.; Blanchard, P.; Roncali, J.; Vuillaume, D.; Alibart, F. Neuromorphic Time-Dependent Pattern Classification with Organic Electrochemical Transistor Arrays. *Adv. Electron. Mater.* **2018**, *4* (9), 1800166. https://doi.org/10.1002/aelm.201800166.

(14) Ben Menachem-Zidon, O.; Avital, A.; Ben-Menahem, Y.; Goshen, I.; Kreisel, T.; Shmueli, E. M.; Segal, M.; Ben Hur, T.; Yirmiya, R. Astrocytes Support Hippocampal-Dependent Memory and Long-Term Potentiation via Interleukin-1 Signaling. *Brain. Behav. Immun.* **2011**, *25* (5), 1008–1016. https://doi.org/10.1016/j.bbi.2010.11.007.
(15) Hao, L.; Yang, Z.; Lei, J. Underlying Mechanisms of Cooperativity, Input Specificity, and Associativity of Long-Term Potentiation Through a Positive Feedback of Local Protein Synthesis. *Front. Comput. Neurosci.* **2018**, *12*.
(16) Molnar, C.; Gair, J. *Concepts of Biology - 1st Canadian Edition*; BCcampus, 2015.
(17) Citri, A.; Malenka, R. C. Synaptic Plasticity: Multiple Forms, Functions, and Mechanisms. *Neuropsychopharmacology* **2008**, *33* (1), 18–41. https://doi.org/10.1038/sj.npp.1301559.
(18) Lamprecht, R.; LeDoux, J. Structural Plasticity and Memory. *Nat. Rev. Neurosci.* **2004**, *5* (1), 45–54. https://doi.org/10.1038/nrn1301.
(19) Haydon, P. G.; Carmignoto, G. Astrocyte Control of Synaptic Transmission and Neurovascular Coupling. *Physiol. Rev.* **2006**, *86* (3), 1009–1031. https://doi.org/10.1152/physrev.00049.2005.
(20) Blanco-Suárez, E.; Caldwell, A. L. M.; Allen, N. J. Role of Astrocyte–Synapse Interactions in CNS Disorders. *J. Physiol.* **2017**, *595* (6), 1903–1916. https://doi.org/10.1113/JP270988.
(21) Paixão, S.; Klein, R. Neuron–Astrocyte Communication and Synaptic Plasticity. *Curr. Opin. Neurobiol.* **2010**, *20* (4), 466–473. https://doi.org/10.1016/j.conb.2010.04.008.
(22) Allen, N. J. Synaptic Plasticity: Astrocytes Wrap It Up. *Curr. Biol.* **2014**, *24* (15), R697–R699. https://doi.org/10.1016/j.cub.2014.06.030.
(23) van de Burgt, Y.; Lubberman, E.; Fuller, E. J.; Keene, S. T.; Faria, G. C.; Agarwal, S.; Marinella, M. J.; Alec Talin, A.; Salleo, A. A Non-Volatile Organic Electrochemical Device as a Low-Voltage Artificial Synapse for Neuromorphic Computing. *Nat. Mater.* **2017**, *16* (4), 414–418. https://doi.org/10.1038/nmat4856.

Chapter 4. Introduction of Hebbian learning rules through dendrites maturing

Introduction

This chapter explores the possibility of dendritic electropolymerization to reveal structural plasticity. There were specifically carried out tests to conduct dendritic growths using Hebbian learning rules based on spike-timing and spike-rate dependent activity. As well, the effect of these different activities on dendritic growth and its properties was examined. In addition, we verified the possibility of inducing dendritic growth, relying on the structural plasticity process, with a dimensional modification of the system, namely, with a change in the distance between the electrodes.

Finally, using the same structural plasticity process, an attempt was made to mimic more complex brain features, such as Pavlovian conditioning and classification tasks, by means of two different approaches.

1. Hebbian learning rules in neuromorphic hardware

Apart from synaptic plasticity (that includes LTP and STP functions), another important mechanism in human brain responsible for learning and memory processes is structural plasticity that in turn refers to Hebbian learning rules. Hebbian learning specifies that correlated activation of pre- and postsynaptic neurons leads to the development of new neuronal paths or its strengthening[1]. This learning principle was first proposed by Hebb, who postulated "*When an axon of cell A is near enough to excite a cell B and repeatedly or persistently takes places in firing it, some growth process or metabolic change take place in one or both cell such that A's efficiency, as one of the cells firing B, is increased* " [2]. The synaptic weight within this concept updates on the base of two main paradigms: spike-timing-dependent plasticity (STDP) and spike-rate-dependent plasticity (SRDP)[3].

To date, utilization of Hebbian learning rules on the neuromorphic hardware has been successfully demonstrated as guiding algorithm during training. For instance, performing tasks in memristor Neural Network (memNN) shall be conducted with several procedures: 1) Connection of artificial synapses and neurons (i.e. definition of the network topology); 2) Information encoding; 3) Training and testing the neural network with the training/testing dataset.

For most tasks, depending on their type, an encoding step is necessary, since the information from the real world or the dataset cannot be directly transmitted to the input of memristive arrays. Therefore, if necessary, the dataset should first be converted into pulses with specific parameters (amplitude, width, number, timing, and frequency). In ANN, analog data will be encoded on the basis of the pulse amplitude or pulse width, while SNNs will rely on the timing and frequency of spikes.

After defining parameters, the training is realized, in which updating synaptic weight is carried out according to certain learning rules. In SNNs, Hebbian rules usually play this role. The choice of the training rule is linked to the encoding technic: a timing-encoding network

will rely on the STDP rule, whereas the SRDP rule will be suitable for a frequency-encoding network.

During training, the pre-neurons deliver the encoded information to the synaptic array. The weighted summation of input signals is received by the post-neurons and generate a corresponding activity (i.e. encoded in timing or frequency). The timing/frequency (i.e. activity) in the input and output layers can then be used to estimate the change in synaptic weight. By repeating this process several times, the recognition error after the training can be reduced remarkably. Afterward, the information in a testing set is fed into the SNN, and the testing results are obtained[4].

Currently, the application of Hebbian learning rules on neuromorphic hardware has been successfully addressed. For example, Wang *et al*. presented a fully memNN with integrated LIF neurons based on diffusive memristors with an 8 × 8 memristive array[5]. The chip demonstrated the pattern classification achieved through the STDP learning rule with the unsupervised weight update[4].

SRDP was as well recently addressed for pattern learning in several hardware implementations[6,7]. For instance, Milo *et al*. exhibited online unsupervised learning of patterns with 8 × 8 pixels on the 4T1R (using four transistors and one memristor) structure using SRDP[6]. Additionally, Huang *et al*. succeeded to classify 10 images on a single-layer fully-connected network by SRDP and presented a CNN-SRDP network to recognize the whole MNIST images with up to 92% accuracy, which expands the learning potential[8]. However, these works are still facing with certain challenges. In the 4T1R structure of Milo *et al*., network's learning capacity is constrained due to its small-scale, making it unable to classify for difficult tasks like for recognizing inputs of larger dimensions. In the work of Huang *et al*. only simulation results are demonstrated, and the device functioning was presented on discrete cells. Hence, demonstration at the network level should be proposed to be able to address more practical tasks improvement in SRDP[9].

Therefore, considering the abovementioned restraints for small-scale or large-scale networks, one may conclude that the size of a chip and, consequently, the number of devices on it, represents a significant challenge for the future operation of neuromorphic hardware. Mainly, this is decisive due to the necessity to address various neural network topologies, which is remaining a challenge for neuromorphic engineering at the moment. A significant factor in neural network (ANN, SNN) for learning is its topology, which is basically how neurons (nodes) are interconnected. It can involve either all nodes in the input, output, and hidden layers or only specific nodes from each layer[10]. Nevertheless, to fit any topologies, which are unknown prior to learning, the hardware substrates have to be oversized. However, nodes and connections of the network should be physically outlined in advance. As a result, this aspect leads to an ultra-high density of components (synaptic connections) and affects the power efficiency of the hardware and the time for training a given dataset, posing a significant barrier to the development of ultra-low power neuromorphic circuits for online inference.

On the contrary, on a biological level, as a part of phenotypic plasticity during neurogenesis, homogeneous cells differentiate into neurons and project their dendritic connections to achieve an optimal topology and to provide the organism with its specific abilities. This structural plasticity mechanism is one of the main tools of biological energy efficiency since resources for building new neural paths are involved by necessity upon certain conditions.

Hence, one can consider a new way of device fabrication based on self-developed connections, following biological approach to overcome the scale, power issues and the associated complexity of operation in neuromorphic engineering. This would eliminate the need for

pre- connecting or reconnecting a large number of nodes (devices) and allow computing units to be established directly during training or task implementation, like in biological neural networks.

Previously, Akai-Kasaya *et al*. already demonstrated the possibility of growing PEDOT:PSS wires on in-plane lithographically patterned electrodes to form an ANN with tunable synaptic weight, i.e., conductance. An update of conductance in this particular study was achieved by increasing the number of wires bridging two electrodes[11].
As for our work, in the previous chapter, we have already shown that polymer dendrites generated on free-standing electrodes are capable of emulating synaptic plasticity. Moreover, the synaptic strength of the already existing network can be adjusted. To contribute to the aforementioned challenge, we intend to implement structural plasticity, in which network topology and properties such as weight are directly determined by initial programming. Unlike the abovementioned work with 2D wires for ANN, topological plasticity here will be exhibited through electropolymerization driven by Hebbian learning rules. It implies that the conductance change will be controlled by different electropolymerization parameters and mechanisms.
Therefore, this method can expand the possibilities for developing evolvable neuromorphic devices and scalable networks.

2. Spike-timing-dependent plasticity

2.1 Spike-timing-dependent plasticity in neuroscience

One of the plasticity types in human brain is spike-timing-dependent plasticity (STDP). According to STDP, synaptic weight modulation is based on the activities between neurons, namely on the relative timing of pre- and post-synaptic spikes[12]. This relative neuron spike timing is defined as Δt ($\Delta t = t_{pre} - t_{post}$), where t_{pre} is the time of presynaptic neuron spike arrival and t_{post} is the time when the postsynaptic neuron spike arrives[13,14].
According to STDP the synaptic weight increases if postsynaptic spike occurs after presynaptic one ($\Delta t>0$) and at smaller Δt the synapse's strength becomes higher, therefore provoking long- term potentiation (LTP). Inversely, when postsynaptic spike precedes presynaptic one ($\Delta t<0$) the synaptic weight decreases and it reduces more at lower negative Δt, which is long- term depression (LTD) (**Figure 1**)[15].

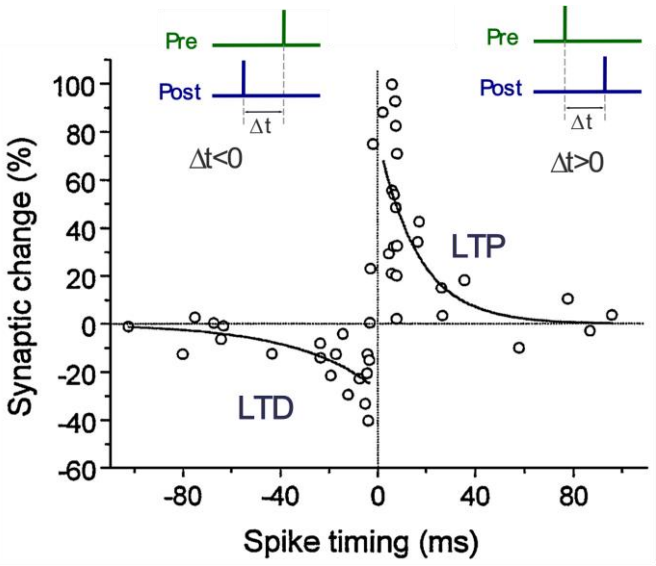

Figure 1. Asymmetric STDP learning window showing induction of long-term potentiation (LTP) and long-term depression (LTD) in neuronal hippocampal cultures. The figure is taken and modified from[16].

2.2 Spike-timing-dependent plasticity by means of polymer dendritic growth

Previously it was demonstrated that the growth of PEDOT dendritic branches occurs in between pair of Au electrodes immersed into electrolyte and it derives from EDOT oxidation under influence of electrical potential at the interface between the electrode and the electrolyte. AC electropolymerization process and consequent form of grown fibers have been shown to be linked to electrical parameters of applied input signal (peak-to-peak amplitude, frequency). Furthermore, synthesized topologies exhibited various conductance states that can be related to synaptic weight. Thus, since dendritic growth is reminiscent of neural genesis, this parameter dependency can be used to reproduce neural structural plasticity and show how bottom-up engineering can serve to find optimal topologies for computing.

Development of neural network is a complex process controlled by many aspects, nevertheless a simplified hardware adaptation will be considered in this study, with limited number of parameters. The main and initial factor influencing the likelihood of cells interconnection is their activity correlation that can be addressed in our system through dynamics and diffusion of chemical species in between electrodes (pre and post neurons). In a first approach, we propose to use spike-timing difference to evaluate correlation of activity in between two nodes.

Pre- and post- neuron activity in our system was emulated by bipolar pulses with constant width, V^+/V^- amplitude, and mean frequency $F=f_{pre}= f_{post}$. These pulses were applied with different polarity. Pulses interactions resulting from electrical potential difference between electrodes ($V_{pre} - V_{post}$) lead to their overlapping and corresponding overpotential causing electropolymerization. Correlated activity was represented as difference in timing between pre and post signals. Pulses were shifted from each other by a ΔT time difference. Therefore, short time difference in spike timing lead to an effective overlap with longer duration of the overpotential and consequently stronger correlation of activity. On the contrary large time distance resulted to a small area of overpotentiation duration and was associated to a low correlation (**Figure 2**).

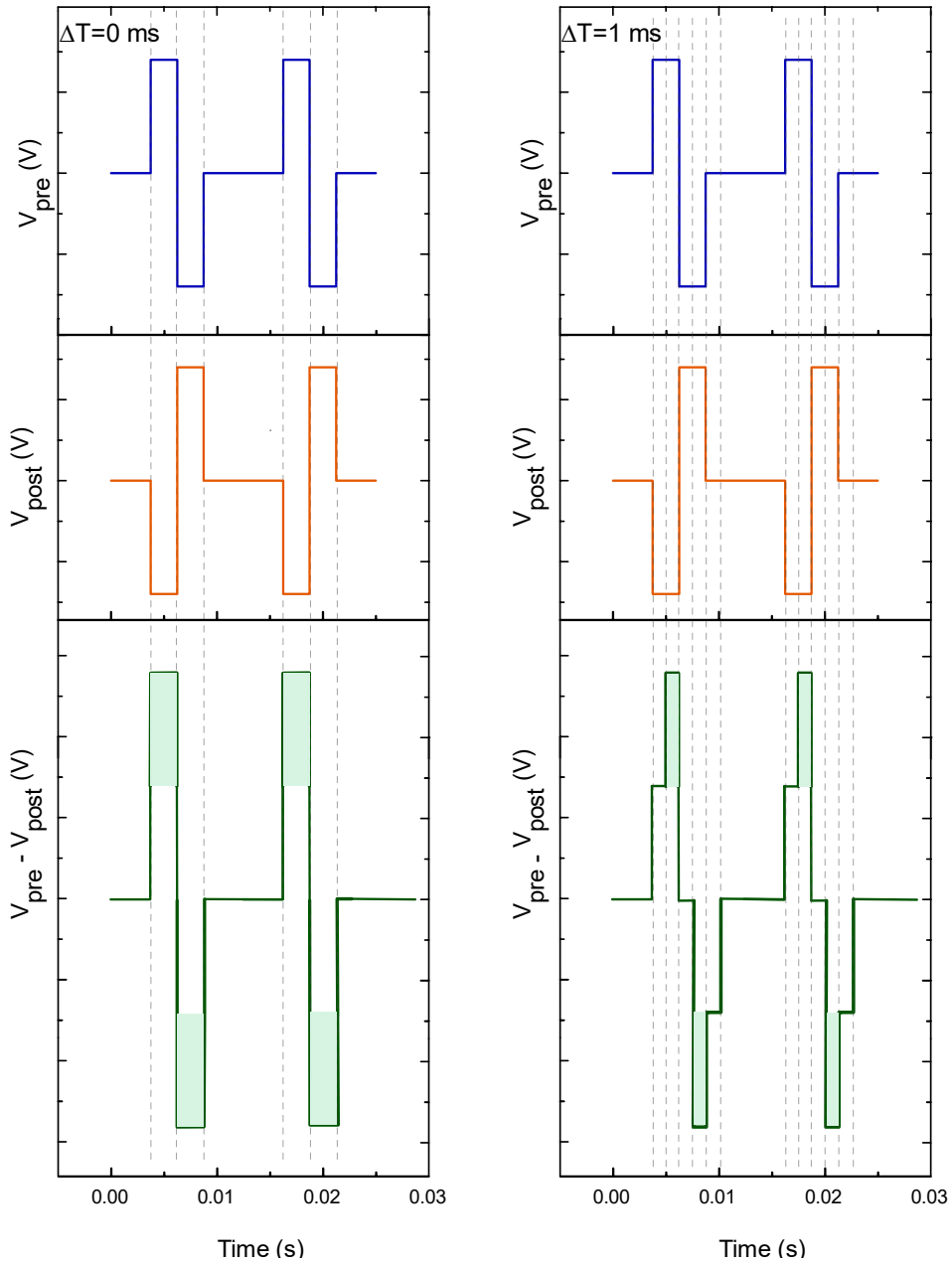

Figure 2. Interaction of V_{pre} and V_{post} bipolar pulses resulting in overpotential signals (green highlighted regions) with longer and reduced potential duration at ΔT=0ms and 1ms respectively.

For realizing structural plasticity, the same two-wire setup was utilized: electrodes were associated to the pre- and post-neuron, respectively. Pairs of Au wires were immersed into aqueous electrolyte containing 10 mM of EDOT, 10 mM of BQ and 1 mM of NaPSS and placed onto the same height and 240 µm distance from each other. The duration of upper and bottom parts of a pulse was 2.5 ms for each. The time shift (ΔT) between pulses was varied from 0 ms (strong correlation) to 2 ms (low correlation). The signal application was stopped 30 s after the first contact of polymer fibers with each other. Obtained structures are shown on **Figure 3**. The frequency of applied signals in between pre- and post- terminals were equal to each other and defined as mean frequency $F=f_{pre}=f_{post}=$ 80 Hz, while voltage was maintained as

V^+/V^- = 5 V/- 5V. Preliminary effect of amplitude at aforementioned conditions and ΔT= 0 ms was verified (**Supplementary Figure 1**). As a result of this examination, branchy and voluminous dendrites obtained at V_p = 5 V was chosen to study the effect of ΔT since one can expect more obvious and broad changes in morphology with reducing effective overlap.
It was noticed that longer overpotentiation at ΔT= 0 ms referring to stronger activity correlation lead to active dendritic growth with dense morphologies and formations of more junctions in between single fibers that can be compared to synaptic connections. With increasing time shift in between pulses (decreasing the correlation), the overpotentiation duration was reduced and consequently fewer dendritic branches and correspondingly fewer interconnections matured. We note that in the absence of overlap between pulses no dendritic growth was noticed within the experiment duration.
The same experiments were repeated for mean frequencies of 20 Hz and 130 Hz (to emulate high and low firing rate). It was noticed that in terms of morphology, decreasing frequency leads to topological change from more branchy dendrites to less sparse shapes. However, similarly to 80 Hz, with decreasing signal frequency, the same effect of time correlation on electropolymerization was observed for all experiments at various mean frequencies. Interestingly, at ΔT = 1.5 ms and 2 ms, for F = 20 Hz, no completed dendritic connections were formed due to low rate of applied pulses and high time shift in between them.

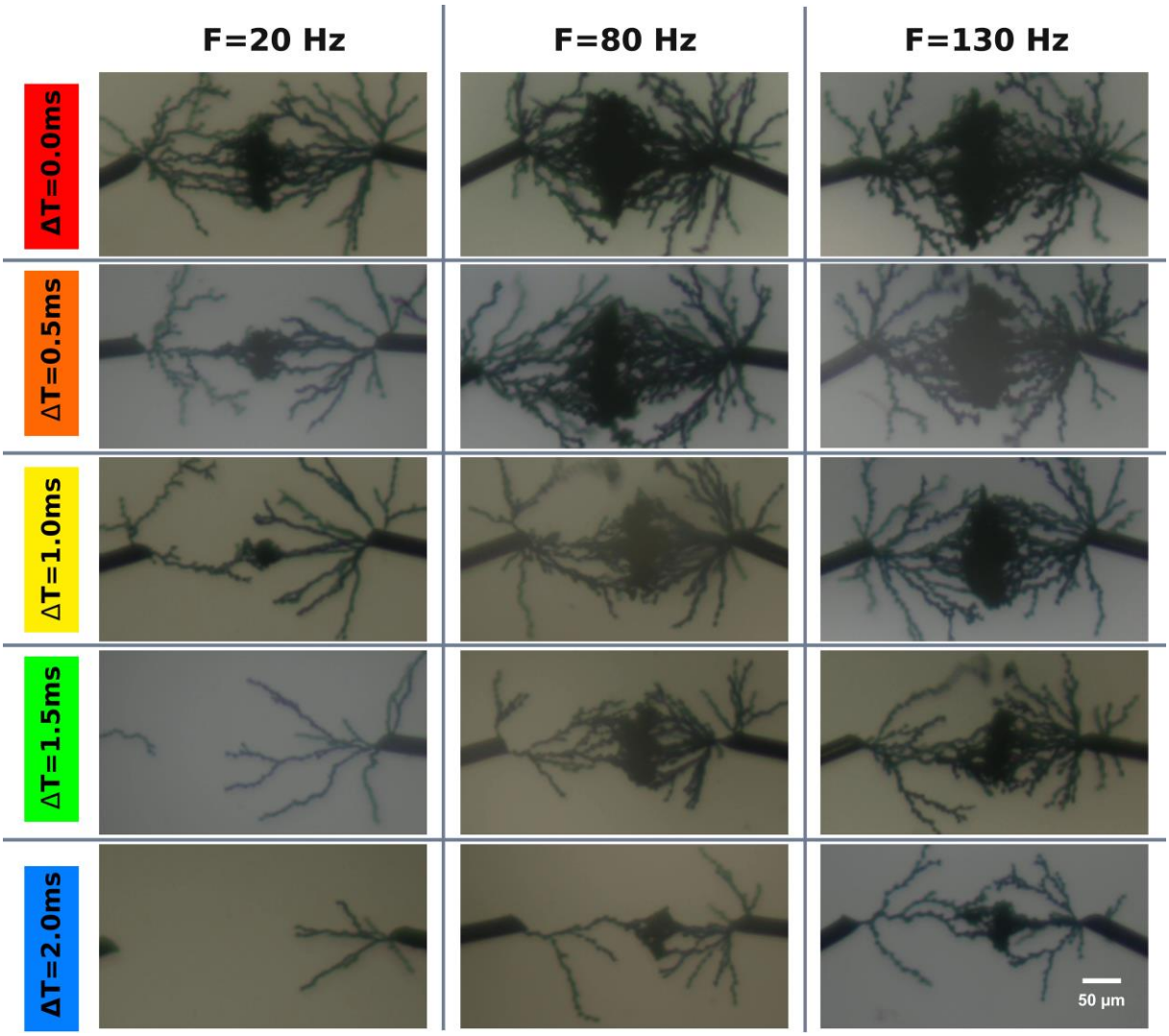

Figure 3. Spectroscopy images of accomplished dendritic branches obtained as a result of increasing ΔT time shift (diminishing effective overlap) in between electrical pulses at F = 20 Hz, 80 Hz and 130 Hz. No connections occurred at ΔT = 1.5 ms and 2 ms at F = 20 Hz.

For all types of established dendritic connections, the electrical conductance measurements were realized (**Figure 4a**). For all three mean frequency experiments, high activity correlation with denser dendritic interconnections exhibited higher conductance. Reciprocally, increasing ΔT (decreasing effective overlap) led to lower conductance.

Additionally, conductance adjustment can be achieved via modulation of the incoming signal frequency. No significant difference in conductance variation was noticed for structures obtained at 130 Hz and 80 Hz. However, connections formed at 20Hz appeared less conductive in comparison with higher aforementioned frequencies.

In addition, through image and video analysis, information about longitudinal growth rate of the dendritic branches was extracted. It turns out that the growth rate is not affected by time correlation between pre- and post- terminals but in direct relation with frequency signals according to which one may expect faster growth with increase of events periodicity (**Figure 4b**). This observation is consistent with the results described in Chapter 2, where higher frequency favors quicker dendrites' interconnection.

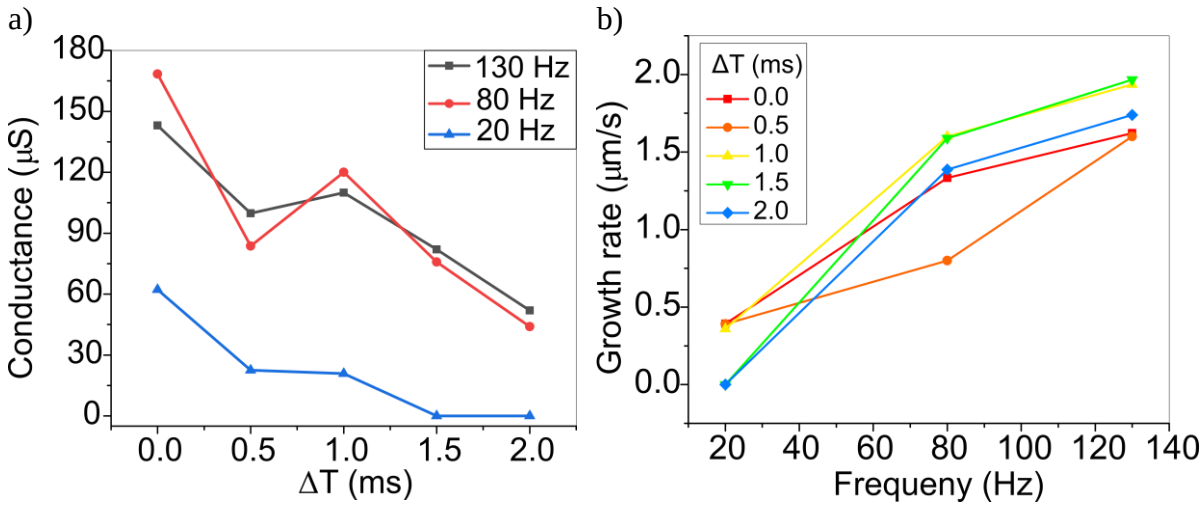

Figure 4. a) Conductance evolution and b) Longitudinal growth rate evaluation of dendritic connections synthesized at different ΔT values and at F= {20 Hz, 80 Hz and 130 Hz}.

Therefore, by means of AC electropolymerization and controlling effective voltage overlap of applied signals, one may reproduce spike-timing-dependent structural plasticity on artificial hardware. In other words, it is possible to develop in-situ working units, i.e dendritic connections with certain topology (amount of synaptic connection- i.e. junctions) and synaptic weight (conductance state) upon the specified programming and without saturation of the computing hardware environment. Additionally, application of dendritic interconnections based on STDP is not limited to one type of waveform. On memristors, it was already shown that by reshaping the spike waveform, one can adjust or completely change the STDP learning function[17]. Therefore, dendritic development on the basis of spike-timing activity can be as well tuned by employing various form of pulses. For example, with triangular-shaped pulses, it is possible to change not only the duration of overpotentiation but to modify as well voltage of the resulting signal and thus expect different growth behavior and final properties.

2.3 Effect of distance on dendritic structural plasticity.

Other major factor responsible for the probability of cells being interconnected is their geometrical arrangement in relation to each other, according to which closer cells' position will inevitably lead to stronger correlation and a higher interconnection probability while distant location will have reverse effect.

To examine the effect of the distance on the dendritic growth, the same setup was employed, with identical electrolyte content and gold wires serving as neurons. The electropolymerization was carried out with similar bipolar pulses with opposite polarity applied at ΔT = 0 ms, f_{mean} = 80 Hz and V_p = 5 V. Several distances were examined for which wires were shifted from each other: 240 µm, 420 µm, 540 µm.

Figure 5 exhibits dendrites obtained at aforementioned conditions and at increasing gap in between electrodes. Dendrites grown at smallest distance value 240 µm are presented by arborous and dense structure. With increasing the gap distance, one could still observe the polymer growth that occurred in more elongated and less dense and branchy forms.

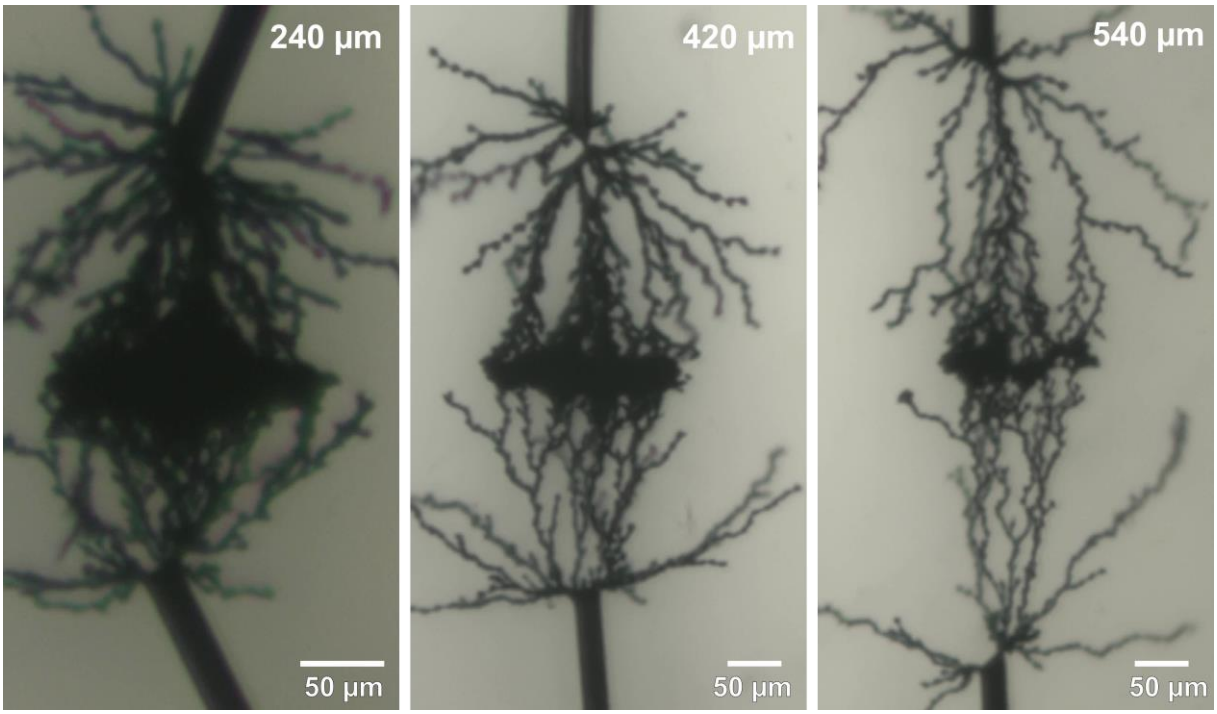

Figure 5. Microscopic images of dendritic morphologies synthesized at different distances.

30s after dendrites completion conductance values were measured. Similarly, to previous results, branchier and larger polymer objects synthesized at 240 µm possessed higher conductance (**Figure 6a**). Conversely, elongated and sparser forms showed drop in conductance with extending the gap between electrodes. It can refer to both the fact that the resistance in a wire-shaped conductor rises as its length increases and that morphological structures with fewer fibers' junctions have lower conductance.

Moreover, we noticed phenomenon of dendrites' shaking when approaching branches from both electrodes are close enough to each other. It can be related to an increase in the electric field in between them that eventually results in the shaking of polymer branches. Due to this shaking effect, completion does not happen right away, as it was shown before in Chapter 2 and latency in finishing a connection occurs. Nevertheless, with increasing interelectrode spacing, this effect of shaking is reduced, and the joining of the dendrites from both sides takes place faster. Therefore, since it is hard to distinguish the latency time, the growth rate was estimated before the moment of instability when dendrites are too close to each other. Thus, for all three cases, it was calculated at a certain time from the start of electropolymerization as a function of the distance over which dendrites grew to this certain growth time t = 135 s.
Longer time was required for branches to complete as the gap increased. Nevertheless, it was found that the growth rate showed completely opposite trend. Namely, the rate of polymer fiber electropolymerization per second is higher at the longest distance of 540 µm and it diminishes with reducing distance (**Figure 6b**).
Aforementioned tendencies can be derived from the voltage distribution in the electrolyte. As the distance between the electrodes changes, resistance of the electrolyte modifies as well that hence lead to different drop of voltage across the system electrode/electrolyte/electrode. When the electrodes are placed closer to each other, the electrolyte's resistance decreases and

the voltage drop at the wires' interface becomes higher. Higher surface potential at an electrode surface results in more intense redox processes, more electropolymerized PEDOT and, consequently, a higher conductance value of formed dendrites. As the interelectrode gap increases, the voltage drop at the wires' interface becomes lower, leading to less intense and slower electropolymerization.

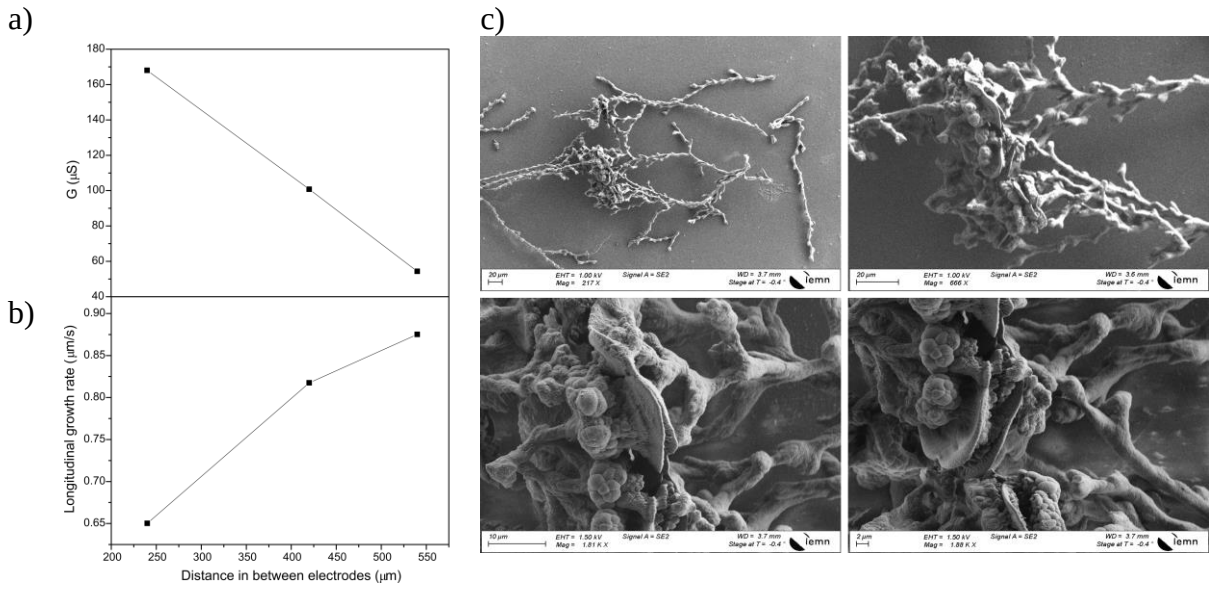

Figure 6. a) Conductance modulation and b) longitudinal growth rate of dendritic objects grown at different distances in between electrodes: 240µm, 420µm and 540µm distances. c) Scanning electron microscope images of polymer dendritic structure (grown at 540µm distance) after its extraction from the electrolyte.

Discovering this possibility to induce structural plasticity through dendritic growth at different distances gives an opportunity to create on hardware-level artificial neural connections when it is required. This examination is a significant contribution for future hardware realization in terms of geometry and integration strategies. Furthermore, by modifying the initial electropolymerization parameters (voltage, frequency, and ΔT), one can develop a wide range of connections with variable and adjustable synaptic weights, resulting in an evolvable and scalable neural network.

2.4 Associative learning demonstration

One of the important features that neuromorphic devices are implementing is the learning processes alike in human brain. One of the most famous examples of learning is associative learning. Apart from brain-like computing, introducing this feature is of great importance for bioelectronics. Associative learning is a fundamental learning principle that matters for an individual's adaptability[18]. The most-known associative learning demonstration is the Pavlov's dog experiment. This discovery claims that dogs, who naturally salivate (unconditioned response, or UR) in response to food (the unconditioned stimulus, or US), would come to salivate under influence of different stimulus, such as the ring of a bell (the conditioned

stimulus, or CS) after a certain number of experiments with the pairing of the CS and the US (after training).

To demonstrate associative learning, previously shown here the possibility to induce dendritic growth through STDP structural plasticity was employed to reproduce the Pavlov dog experiment. The objective of this demonstration is to show how selective neuron recruitment can be induced during correlated activity across many nodes. Two electrodes were associated as food and bell stimuli and placed at an equal 240 μm distance from "saliva" electrode. Previously discovered dependency of dendritic connection on pulses time correlation was utilized here. The same type of bipolar signals with pulse width 2.5 ms were employed in which "food" and "bell" stimuli had one type of polarity V^+/V^- and "saliva" pulses were applied with reversed polarity order V^-/V^+ . To induce overpotentiation but not cause intensive electropolymerization all the signals were applied with minimum voltage $V^+/V^- = 3.5$ V/-3.5 V. The experiment was divided into two phases (**Figure 7**). During the first phase all three signals were applied. Nevertheless, time correlation between pulses was programmed only in between food (pre-neuron) and saliva (post-neuron) that eventually resulted in dendrites development (denoting synaptic junction) while bell potentiation uncorrelated with Saliva signal did not lead to any completed connection (only a small outgrowth). In the second phase, the bell's signal was similar to food stimuli and appeared to be correlated with salivation. It resulted into overpotentiation and formation of new additional dendritic branches in between correlated nodes indicating a recruitment of the bell signal to salivation.

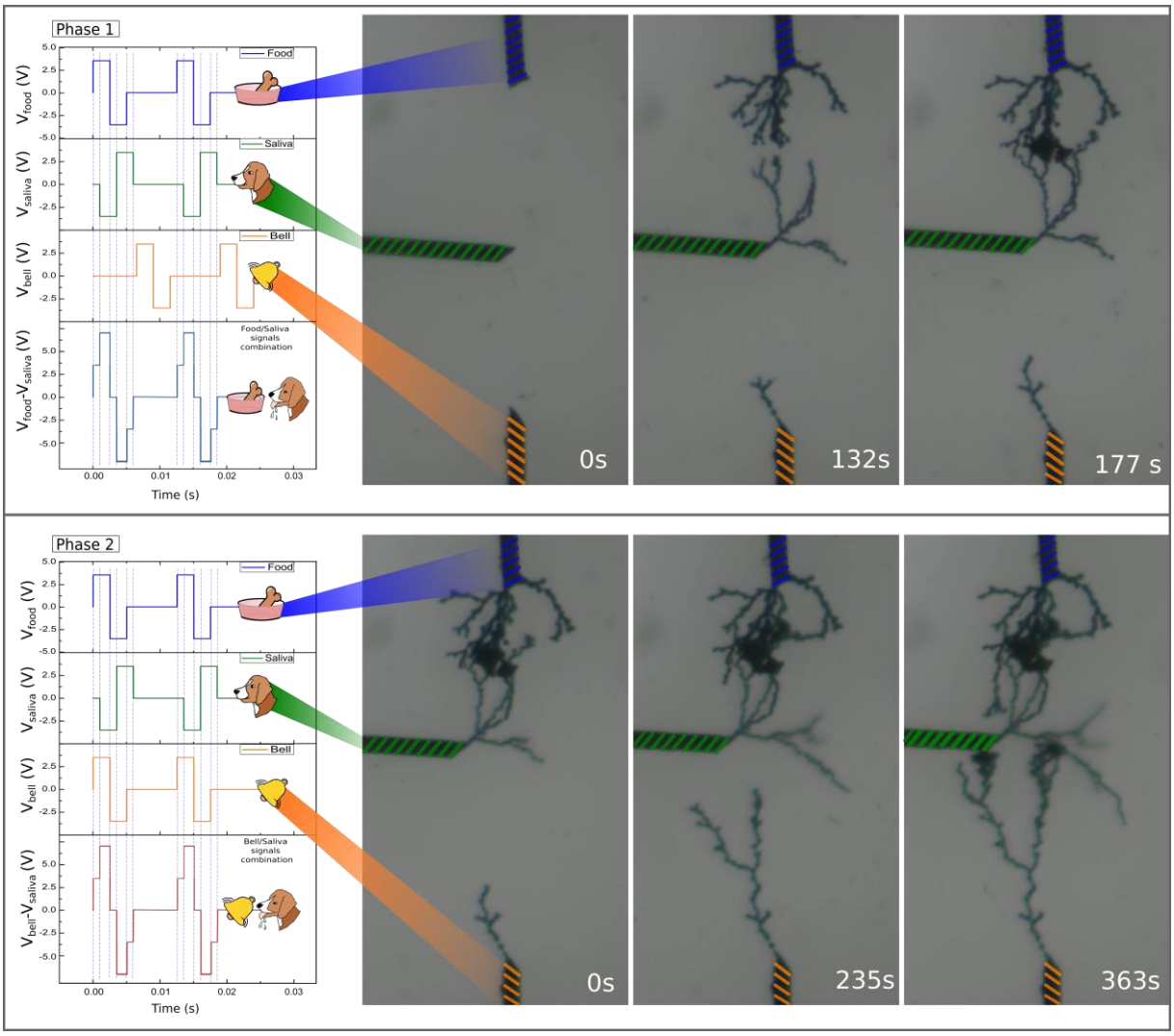

Figure 7. Pavlovian conditioning promoted by means of spike-timing dependent activity electropolymerization in two phases. **Phase 1:** Time-lapse of dendritic growth during which time correlation and corresponding overpotentiation took place only between "food" and "saliva" pulses (signifying that salivation naturally occurs only as response to the food stimuli). **Phase 2:** Dendritic evolution with time in which as a result of associative learning the correlated activity is as well introduced for "bell" and "saliva" signals leading to pairing of these nodes by polymer fibers.

At the moment, a couple of studies have already reported on this question and introduced associative learning on neuromorphic devices through electropolymerization[19]. One of them, employed dendrites as well, to demonstrate associative learning. Nevertheless, it is hard to differentiate which mechanism drives the correlation of activities in this work. The phenomenon can come either from the global effect of an electrolyte or from the local effect of a wire potential. Another approach similar to ours is based on the voltage difference between two inputs[20]. However, it was realized in a non-dynamic mode by means of DC electropolymerization. This approach eventually did not result into dendritic fibers but allowed to observe the growth of OECT thin film channel.

Therefore, with the help of AC-electropolymerization, one may mimic Pavlov's dog conditioning, thus implementing the learning process and the structural development of neural connections at the same time. Pavlovian conditioning is an important mechanism responsible for learning and memory capable to establish relationships between unrelated information[21].

Association based on correlated activities occurs when stimulated neurons recruits surrounding neurons to participate in the learning[22,23]. On hardware level, it means that through dendritic propagation during realization of associative training/learning operation one may attract nodes for developing neural network that were not initially correlated (potentiated) or weakly correlated (potentiated). Therefore, it allows building self-assembled functional neuronal circuits.

3. Spike-Rate-Dependent Plasticity

3.1 Spike-Rate-Dependent Plasticity in neuroscience

Another type of structural plasticity is spike-rate-dependent plasticity (SRDP) which is related to firing rate in between neurons. In biological neural networks, the firing rate of action potentials is directly influencing on information transfer mode[24]. Therefore, it makes SRDP one of the most significant synaptic learning mechanisms in brain cognitive functions[25].
According to SRDP, the synaptic weight between neurons can be tuned through the firing frequency. Precisely, pre-/post- synaptic spiking activity with high frequency will cause potentiation, whereas low frequency of pre-/post- synaptic spikes will lead to depression[26].

3.2 Spike-Rate-Dependent Plasticity by means of polymer dendritic growth

In contrast to dendritic timing-dependent plasticity at fixed frequency values, the emphasis in this part was put on investigating effect of signals' firing rate on resulting dendritic growth and their properties. To mimic neural activity, Poisson distributed spike trains based on bipolar pulses were applied with different mean frequencies. They were responsible for emulating activities between pre- (a_i) and post- synaptic neuron (a_j). The correlation of activity between two neurons i and j was represented as the product of two mean frequencies: $a_i \times a_j = f_i x f_j$.
Likewise, in biological neurons the $f_i \times f_j$ value will designate the probability of having higher or lower correlation in between the two neurons. In our more generalized situation, the principle of hardware correlation as described previously was based on the same pulse overlapping and overpotentiation mechanism (**Figure 8**).
Unlike in previous STDP dendritic realization, bipolar pulses in this case were programmed to have similar polarity order V^+/V^- = 5 V/-5 V, and upper and bottom pulses duration were set as 0.3 ms for each. In this case, it is not necessary to indicate the pre- and post- neurons since signal is the same on all terminals. Due to the small pulse width, the distance between the wires had to be reduced to 60 µm in order to perform dendritic growth. Conductance measurements were carried out 30 s after dendrites from both electrodes approached each other.

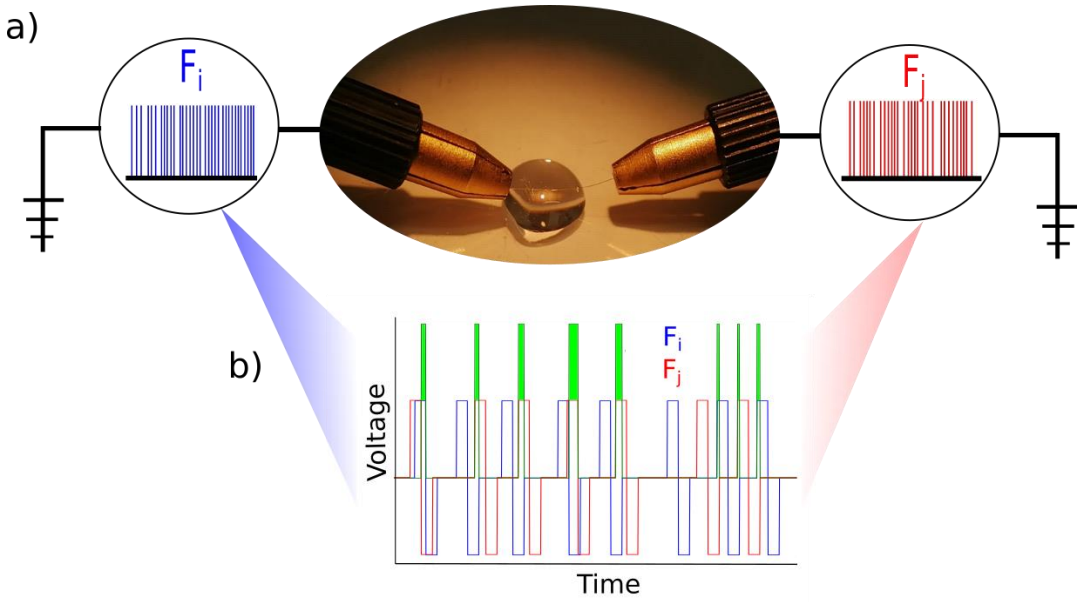

Figure 8. a) Experimental setup for addressing SRDP with the help of PEDOT dendritic growth. Two free-standing gold (Au) wires (with 25 μm diameter) separated by a gap of L = 60 μm were serving as pre and post- neurons with unlike firing activity rate. b) Interaction of Poisson distributed bipolar pulses with f_i and f_j frequencies results in overpotential pulses (green highlighted regions) triggering electropolymerization of EDOT. The procedure was carried out in the same aqueous electrolyte containing 10 mM of EDOT, 10 mM of BQ and 1 mM of NaPSS, as a V_{drop} = 20 μL drop.

A series of experiments with different f_i x f_j combinations were performed. Accordingly, the number of spikes per second resulted in different number of overlapped pulses and consequently in different number of correlated events (**Figure 9**).

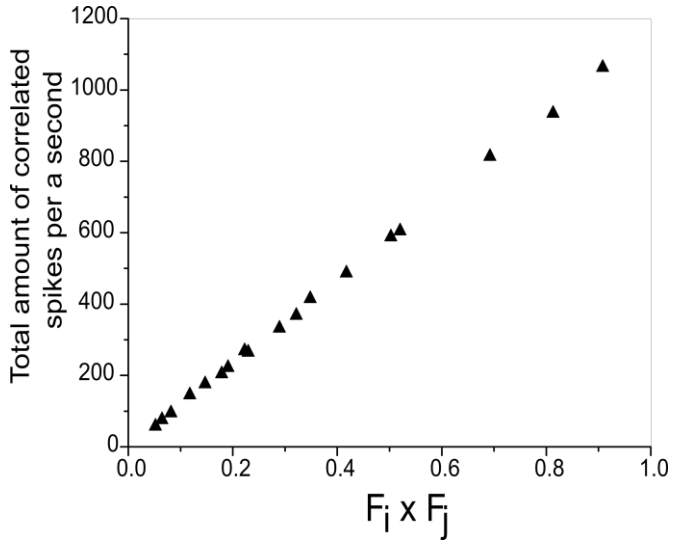

Figure 9. a) Total amount of correlated spikes per second resulting from pulses overlapping with respect to applied f_i x f_j combination values, which have been calculated numerically.

Consistently with the previous results, combination of high f_i and high f_j resulted in larger and more arborous dendritic morphologies with higher conductance (**Figure 10a, b)** due to prevailing number of overpotential pulses *(i.e.*, correlated events) during electropolymerization.

On the contrary, a decrease in the f_i x f_j value leads to less intensive wiring of branches and was associated with lower conductance.
Additionally, the higher amount of correlated spikes derived from pairing high f_i and high f_j showed faster speed of longitudinal growth and higher density of obtained structures. While with decreasing f_i x f_j more time for growth were required (**Figure 10c**) and less dense objects were more likely to appear (**Figure 10d**).

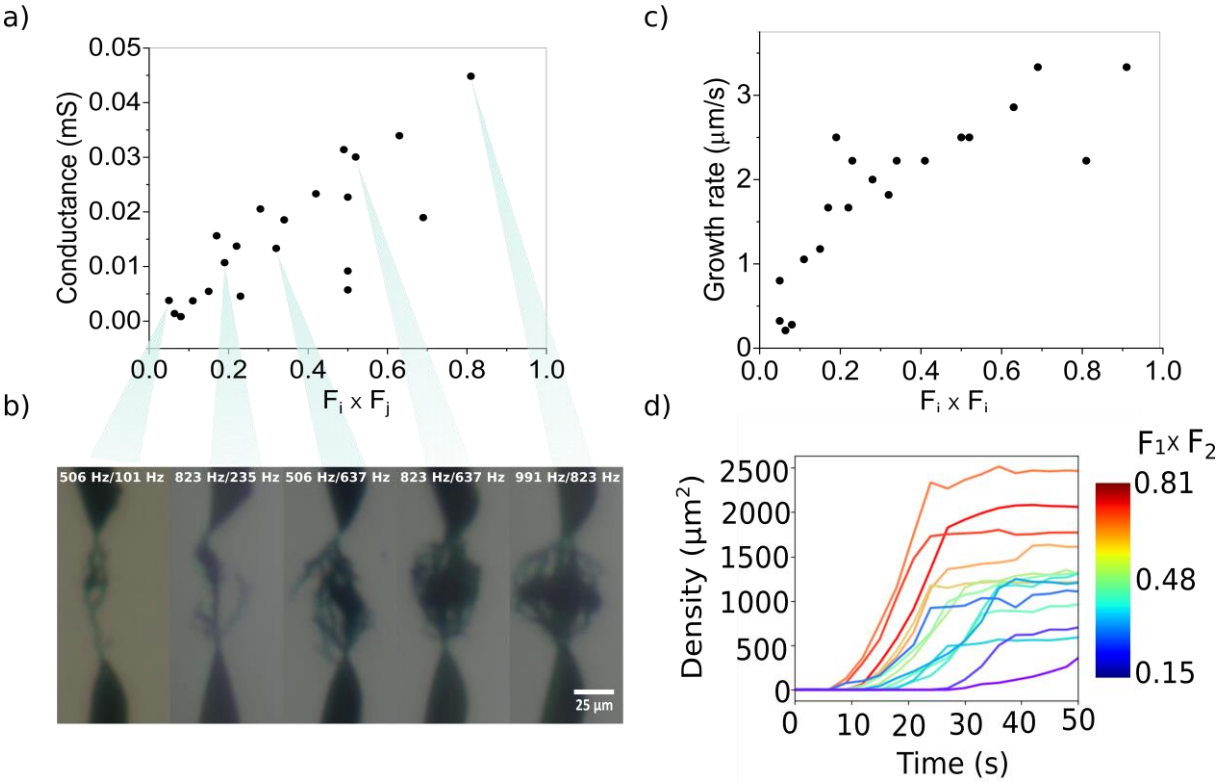

Figure 10. a) Dependency of dendritic connections' conductance with f_i*f_j. b) Microscopic images of samples of five different dendrites grown by pairing of signals with different frequency. Dependency of dendritic c) longitudinal growth rate and d) density evolution of formed structure over time for different morphologies developed at different f_i*f_j values.

On top of ability to activate dendritic wiring with respect to spike-timing frequency, we showed that equivalent mechanism can be addressed through SRDP-like programming, and therefore be able to mimic neuronal connection and their strength under various firing rate. Similarly, to STDP, such structural plasticity reflects on morphological features as well as on conductance states.

3.3 Classification tasks be means of polymer dendritic growth

This capability to create stronger or weaker dendritic wiring with different dynamics of dendritic development and synaptic weight was used to introduce classification task. Different Poisson-distributed bipolar signals with different frequencies were utilized here too.

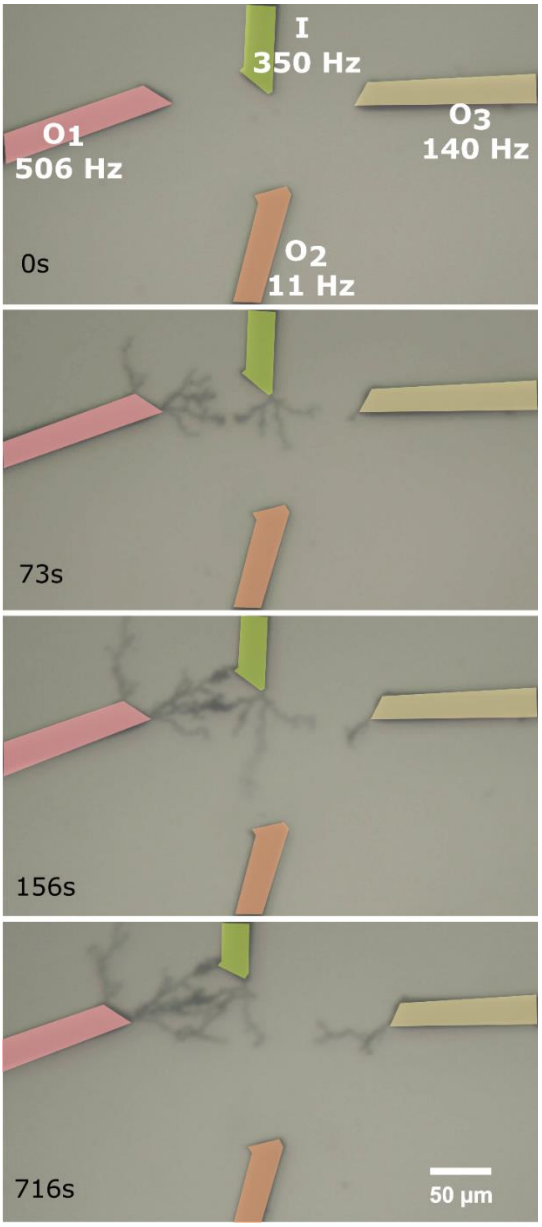

Figure 11. Time lapse of classification task induced by means of dendritic growth on Input and three different Output electrodes with various frequencies.

For this in a four-wires setup, electrodes served as one input neuron and three output neurons spiking with four different mean frequencies (f_I = 350 Hz, f_{O1} = 506 Hz; f_{O2} = 11 Hz; f_{O3} =140 Hz) (**Figure 11**). Every output wire's tip (O_i) was placed at the same 80 µm distance from the input ones (I).

The faster contact with much more junctions (synaptic connections) happened in pair I and O_1 due to high correlation activity in between them. Interaction of I and O_2 with lower activity led to a small branch formed from O_2 side without creating any connection. Finally, interaction with the lowest output neuron O_3 did not show any visible growth of polymer fibers during the experiment time frame.

Since STDP and SRDP learning rules have been mostly utilized for pattern recognition tasks, such type of classification demonstration through dendritic propagation pave the way for more flexible bottom-up differentiation in between different classes of signals or data.

3.4 Classification by means of dendrites for sensing purposes

In previously reported SRDP demonstration through dendritic growth, we utilized input and output signals with the similar data representation (with comparable pulse width, amplitude). However, in this part the SRDP demonstration is intended unconventionally with modified signals. In this case short-lasting small voltage pulses (defined here as spikes) at various frequency were employed as input (pre-synaptic signals), while high amplitude pulses at low frequency and longer duration served as output (post-synaptic signals).
Similar to the conventional SRDP implementation, electropolymerization here was as well relying on spike event activation reproducing Hebbian structural plasticity. However, electropolymerization was triggered through potential pining on the electrodes caused by duty cycle changes (previously mentioned in Section 7, Chapter 2). A sufficient voltage bias is not triggered here by similarly shaped pulses, as the approach is intended for generic cases for low voltage spike inputs that do not benefit from encoding (so the output has to compensate for the required applied voltage to trigger sufficient voltage bias for electropolymerization, only upon correlation with low analog signals). Interconnections occurred only under dynamical correlation conditions, which appeared as a result of the perturbation effect of input spikes on the output signal. Depending on perturbation induced by input spikes, one could promote different plasticity and favor selective interconnection, with various morphologies and completion time.
To demonstrate the unconventional encoding approach, a three gold-wire setup consisting of two inputs (IN) and a single output (OUT) was employed (**Figure 12**). Output was programmed as a square waveform (V_p = 2.9 V, V_{off} = 1.1 V, f = 80 Hz, dc = 40%) designed to be perturbed by inputs with low voltage spikes (V^+ = 0.2 V, t^+ = 500 μs, V^- = 0 V), which were firing at different spiking rates. Spiking rate was defined as the number of events per second (eps) and replicated using different frequency values. Individually, such input signals would not imply any dendritic propagation but in combination with larger output waveform due to perturbation phenomenon EDOT fibers can be formed.

a)

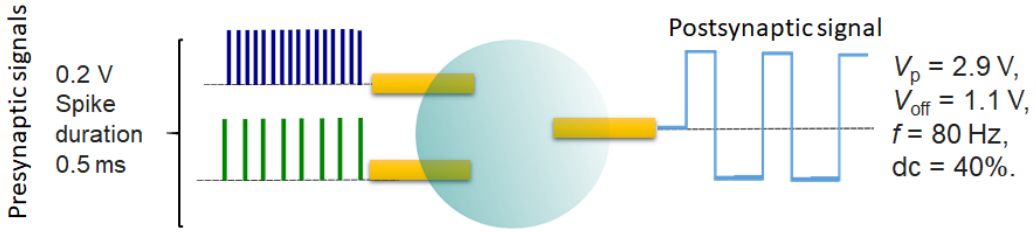

b)

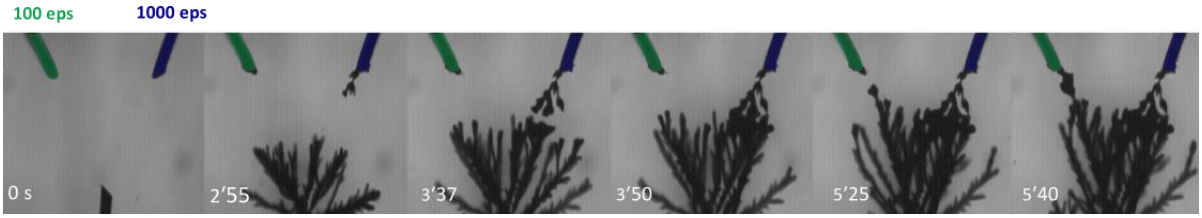

Figure 12. a) The setup representation for implementation of unconventional SRDP encoding through electropolymerization. Specific polarization of the output (postsynaptic signal) and particular input (presynaptic input) will form waveforms that promote either a characteristic morphology with faster interconnection and higher conduction or morphology with slower growth-rate and lower conductance value. b) Example of dendritic growth induced by different dynamics in which first connection occurred in between output and input with higher activity 1000 eps (higher frequency) and only after a connection with lower activity value 100 eps (low frequency).

To examine different morphological conditions and demonstrate classification, inputs with various activity were tested. For this high firing rate activity at 1000 eps (corresponding to 1000 Hz signal) was individually compared to 100, 10, 1 eps activity rates (corresponding to 100Hz, 10 Hz and 1 Hz signals). Under such polarization, EDOT fibers do not grow symmetrically. Instead, a large dendrite expands from the output electrode continuously towards both inputs. It was noticed that this output's fibers in all three cases firstly connect the input experiencing most of the electrical activity (1000 eps) prior to connecting the other one (100eps or 10eps or 1 eps). Moreover, after the completion of connections with both inputs, the current-voltage measurement was performed to evaluate the conductance. The conductance of the connections formed with low-rate inputs remained systematically lower than with the higher-rate input (**Figure 13a**).

As well, we tried to observe conductance evolution of connections formed by inequivalent input's activity for the pair 1000 eps vs 1 eps. Reading (conductance measurement under DC polarization) was performed independently from writing (electropolymerization) through systematical interruption of electropolymerziation. To avoid undesirable oxidation of the material, DC voltage bias utilized for reading was kept lower than the potential required for electropolymerization. Such manipulations did not alter the growth process. **Figure 13b** shows conductance modulation for both dendrites of different inputs from the moment of their completion with output. Being completed first, interconnectivity formed by 1000 eps showed further gradual maturation and corresponding strengthening of the conductance during

formation of a second connection with low rate input. Interestingly, conductance modifications of slower-formed interconnection quite quickly reached the plateau and did not rise further.

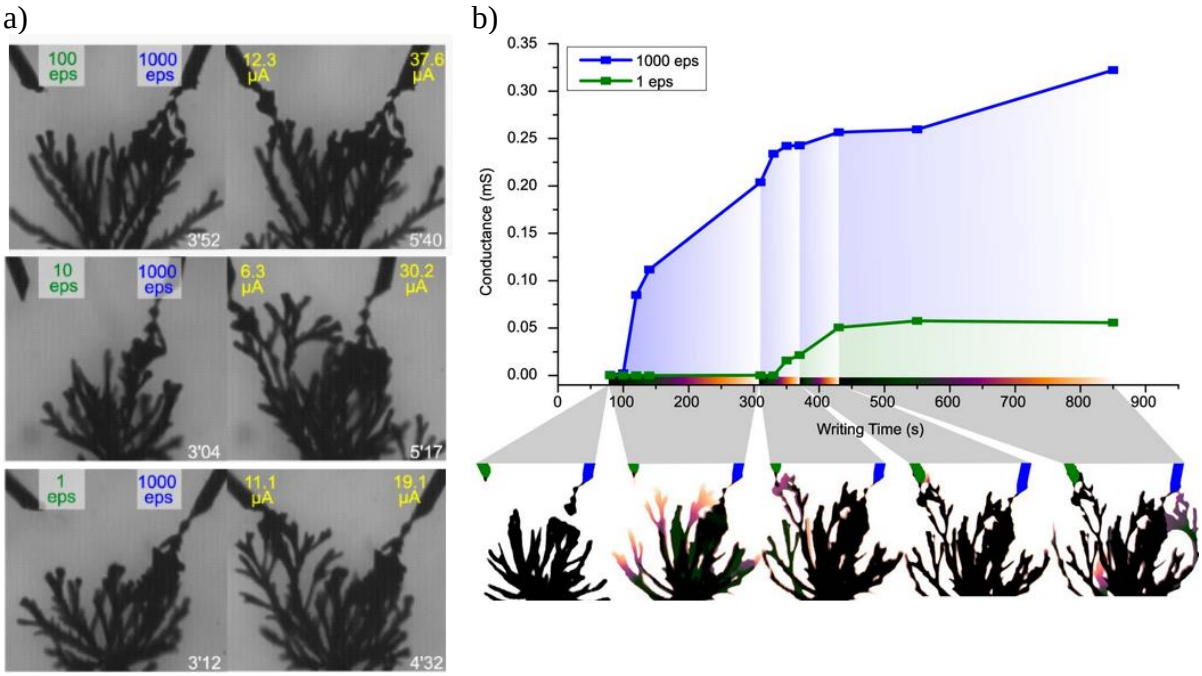

Figure 13. Temporal evolution of the conductance of three-wire connections (formed by 2 IN x 1 OUT) where both inputs fire at a different number of events per second (eps, one event being 200 mV vs. GND for 0.5 ms) and the output wire stimulated at V_p = 2.9 V, V_{off} = 1.1 V, f = 80 Hz, dc = 40%. And the bottom shows the corresponding color-encoded images of the growths displaying the different phases of dendrites completion responsible for the fastest-and-highest interconnectivity of the output to the input that experiences the highest number of events per second.

Due to utilization of small amplitude spikes that are only about twice higher than neuron's action potential (110 mV in amplitude and duration about 1 ms), this unconventional SRDP method can be especially applicable for neurosensing (diminishing the size amplitude of the sensed signal was not attempted). In neurosensing for data processing a layered architecture is used implying separation of recording and computing steps. However, with the help of dendritic SRDP approach it is possible to merge these steps. Specifically, in order to complete and simplify the neurosensing technique, one can propose to use recorded on MEA cells' action potential as input data in our system. The output signal will be supplied from a distinct electrode approaching MEAs. Depending on the recorded activity, i.e input, exclusive dendritic morphologies with specific dynamics can be generated on a distinct substrate, therefore imprinting the spike voltage history recorded within a cell culture and carrying out the classification. Therefore, dendritic growth addressed through SRDP method can be exploited as a tool to represent visually cells activity. In addition to neurosensing, this approach can also be used for other types of sensors that can be driven electronically and where data processing is layered.

Discussion

Therefore, in this chapter, we presented how one can address structural plasticity, specifically STDP and SRDP, through dendritic electropolymerization. We showed how spike- timing- dependency reproduced through various effective voltage overlap and spike- firing rate demonstrated through different frequency signals may induce variety of dendritic topologies with programmable conductance states (i.e synaptic weight) and various dynamics of growth.

The effect of distance on the growth was also examined. It was discovered that one can obtain and control dendritic spreading at different interelectrode intervals. By modifying distance, it is possible to expect not only different fibers' shape with unlike growth speed but as well one can observe changing of their intrinsic properties like conductance (i.e synaptic weight).

The revealed possibility of an AC-electropolymerization approach to induce neurogenesis according to Hebbian rules can be used to present an evolvable and scalable neural network in which programming and connection formation will take place simultaneously.

Moreover, by means of dendritic propagation, we were able to demonstrate associative learning on the base of voltage-effective overlap that further may allow involving additional not stimulated initial neurons (nodes) in the network and create supporting connections within the dendritic network. On top of it, we demonstrated the two different SRDP based approaches for conducting classification tasks referring to the competition between signals with variable firing rates. Moreover, one of these approaches, based on unconventional encoding can become a promising tool for its application in neurosensing for cellular activity differentiation.

Thus, this dendritic development methodology may help to find the right topology for the network relying on activity induced by the external environment and to combine resources utilization with performance.

Additionally, considering the fact that dendrites were synthesized on free-standing wires it may give an opportunity to go from 2D chips (prepaterned and self-developped) towards possible development of neural network in 3D manner that should significantly contribute into the parallelism need in neuromorphic engineering.

Supplementary information

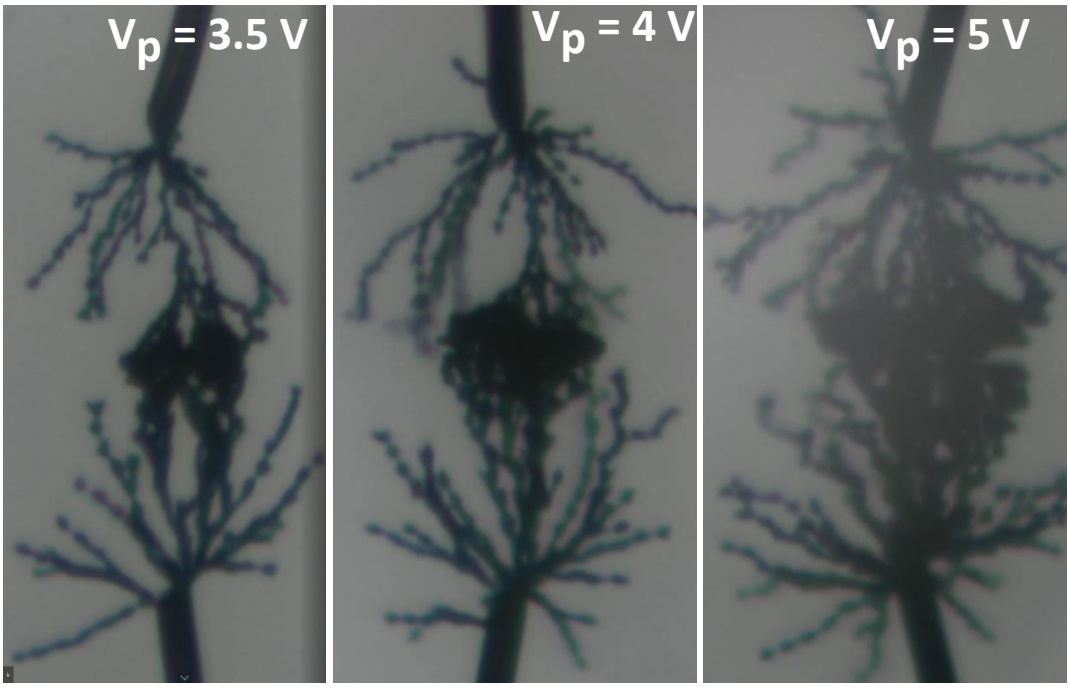

Supplementary Figure 1. Spectroscopy images of accomplished dendritic branches grown using the STDP mechanism at various voltages, fixed $f_{pre} = f_{post}$=80 Hz, and ΔT=0 ms.

Literature

(1) Choe, Y. Hebbian Learning. In *Encyclopedia of Computational Neuroscience*; Jaeger, D., Jung, R., Eds.; Springer: New York, NY, 2013; pp 1–5. https://doi.org/10.1007/978-1-4614-7320-6_672-1.

(2) Hebb D. 1949. The Organisation of Behaviour. New York, NY: John Wiley and Sons.

(3) Bear, M. F.; Cooper, L. N.; Ebner, F. F. A Physiological Basis for a Theory of Synapse Modification. *Science* **1987**, *237* (4810), 42–48. https://doi.org/10.1126/science.3037696.

(4) Huang, H.-M.; Wang, Z.; Wang, T.; Xiao, Y.; Guo, X. Artificial Neural Networks Based on Memristive Devices: From Device to System. *Adv. Intell. Syst.* **2020**, *2* (12), 2000149. https://doi.org/10.1002/aisy.202000149.

(5) Wang, Z.; Joshi, S.; Savel'ev, S.; Song, W.; Midya, R.; Li, Y.; Rao, M.; Yan, P.; Asapu, S.; Zhuo, Y.; Jiang, H.; Lin, P.; Li, C.; Yoon, J. H.; Upadhyay, N. K.; Zhang, J.; Hu, M.; Strachan, J. P.; Barnell, M.; Wu, Q.; Wu, H.; Williams, R. S.; Xia, Q.; Yang, J. J. Fully Memristive Neural Networks for Pattern Classification with Unsupervised Learning. *Nat. Electron.* **2018**, *1* (2), 137–145. https://doi.org/10.1038/s41928-018-0023-2.

(6) Milo, V.; Pedretti, G.; Carboni, R.; Calderoni, A.; Ramaswamy, N.; Ambrogio, S.; Ielmini, D. A 4-Transistors/1-Resistor Hybrid Synapse Based on Resistive Switching Memory (RRAM) Capable of Spike-Rate-Dependent Plasticity (SRDP). *IEEE Trans. Very Large Scale Integr. VLSI Syst.* **2018**, *26* (12), 2806–2815. https://doi.org/10.1109/TVLSI.2018.2818978.

(7) Milo, V.; Pedretti, G.; Carboni, R.; Calderoni, A.; Ramaswamy, N.; Ambrogio, S.; Ielmini, D. Demonstration of Hybrid CMOS/RRAM Neural Networks with Spike Time/Rate-Dependent Plasticity. In *2016 IEEE International Electron Devices Meeting (IEDM)*; 2016; p 16.8.1-16.8.4. https://doi.org/10.1109/IEDM.2016.7838435.

(8) Huang, P.; Li, Z.; Dong, Z.; Han, R.; Zhou, Z.; Zhu, D.; Liu, L.; Liu, X.; Kang, J. Binary Resistive-Switching-Device-Based Electronic Synapse with Spike-Rate-Dependent Plasticity for Online Learning. *ACS Appl. Electron. Mater.* **2019**, *1* (6), 845–853. https://doi.org/10.1021/acsaelm.9b00011.

(9) Li, R.; Huang, P.; Feng, Y.; Zhou, Z.; Zhang, Y.; Ding, X.; Liu, L.; Kang, J. Hardware Demonstration of SRDP Neuromorphic Computing with Online Unsupervised Learning Based on Memristor Synapses. *Micromachines* **2022**, *13* (3), 433. https://doi.org/10.3390/mi13030433.

(10) Miikkulainen, R. Topology of a Neural Network. In *Encyclopedia of Machine Learning*; Sammut, C., Webb, G. I., Eds.; Springer US: Boston, MA, 2010; pp 988–989. https://doi.org/10.1007/978-0-387-30164-8_837.

(11) Akai-Kasaya, M.; Hagiwara, N.; Hikita, W.; Okada, M.; Sugito, Y.; Kuwahara, Y.; Asai, T. Evolving Conductive Polymer Neural Networks on Wetware. *Jpn. J. Appl. Phys.* **2020**, *59* (6), 060601. https://doi.org/10.35848/1347-4065/ab8e06.

(12) Mostafa, H.; Khiat, A.; Serb, A.; Mayr, C. G.; Indiveri, G.; Prodromakis, T. Implementation of a Spike-Based Perceptron Learning Rule Using TiO2-x Memristors. *Front. Neurosci.* **2015**, *9*, 357. https://doi.org/10.3389/fnins.2015.00357.

(13) Jo, S. H.; Chang, T.; Ebong, I.; Bhadviya, B. B.; Mazumder, P.; Lu, W. Nanoscale Memristor Device as Synapse in Neuromorphic Systems. *Nano Lett.* **2010**, *10* (4), 1297–1301. https://doi.org/10.1021/nl904092h.

(14) Shuai, Y.; Pan, X.; Sun, X.; Shuai, Y.; Pan, X.; Sun, X. *Spike-Timing-Dependent Plasticity in Memristors*; IntechOpen, 2017. https://doi.org/10.5772/intechopen.69535.

(15) Kang, D.-H.; Jun, H.-G.; Ryoo, K.-C.; Jeong, H.; Sohn, H. Emulation of Spike-Timing Dependent Plasticity in Nano-Scale Phase Change Memory. *Neurocomputing* **2015**, *155*, 153–158. https://doi.org/10.1016/j.neucom.2014.12.036.

(16) Madadi Asl, M. Propagation Delays Determine the Effects of Synaptic Plasticity on the Structure and Dynamics of Neuronal Networks, 2018. https://doi.org/10.13140/RG.2.2.28601.88166.
(17) Serrano-Gotarredona, T.; Masquelier, T.; Prodromakis, T.; Indiveri, G.; Linares-Barranco, B. STDP and STDP Variations with Memristors for Spiking Neuromorphic Learning Systems. *Front. Neurosci.* **2013**, *7*.
(18) Behrens, T. E.; Hunt, L. T.; Woolrich, M. W.; Rushworth, M. F. Associative Learning of Social Value. *Nature* **2008**, *456* (7219), 245–249. https://doi.org/10.1038/nature07538.
(19) Cucchi, M.; Kleemann, H.; Tseng, H.; Lee, A.; Leo, K. Structural Evolution and On-Demand Growth of Artificial Synapses via Field-Directed Polymerization. arXiv June 11, 2021. https://doi.org/10.48550/arXiv.2106.06191.
(20) Gerasimov, J. Y.; Gabrielsson, R.; Forchheimer, R.; Stavrinidou, E.; Simon, D. T.; Berggren, M.; Fabiano, S. An Evolvable Organic Electrochemical Transistor for Neuromorphic Applications. *Adv. Sci.* **2019**, *6* (7), 1801339. https://doi.org/10.1002/advs.201801339.
(21) Tan, Z.-H.; Yin, X.-B.; Yang, R.; Mi, S.-B.; Jia, C.-L.; Guo, X. Pavlovian Conditioning Demonstrated with Neuromorphic Memristive Devices. *Sci. Rep.* **2017**, *7* (1), 713. https://doi.org/10.1038/s41598-017-00849-7.
(22) Greco, J. A.; Liberzon, I. Neuroimaging of Fear-Associated Learning. *Neuropsychopharmacology* **2016**, *41* (1), 320–334. https://doi.org/10.1038/npp.2015.255.
(23) Cucchi, M.; Dresden, T. U.; Elektrotechnik, F. Organic Electrochemical Networks for Biocompatible and Implantable Machine Learning.
(24) Rachmuth, G.; Shouval, H. Z.; Bear, M. F.; Poon, C.-S. A Biophysically-Based Neuromorphic Model of Spike Rate- and Timing-Dependent Plasticity. *Proc. Natl. Acad. Sci.* **2011**, *108* (49), E1266–E1274. https://doi.org/10.1073/pnas.1106161108.
(25) Bliss, T. V.; Collingridge, G. L. A Synaptic Model of Memory: Long-Term Potentiation in the Hippocampus. *Nature* **1993**, *361* (6407), 31–39. https://doi.org/10.1038/361031a0.
(26) Ren, Z. Y.; Zhu, L. Q.; Guo, Y. B.; Long, T. Y.; Yu, F.; Xiao, H.; Lu, H. L. Threshold-Tunable, Spike-Rate-Dependent Plasticity Originating from Interfacial Proton Gating for Pattern Learning and Memory. *ACS Appl. Mater. Interfaces* **2020**, *12* (6), 7833–7839. https://doi.org/10.1021/acsami.9b22369.

General conclusion and perspectives

As it was highlighted in the introduction, the main aim of this work was to develop a self- evolvable neuromorphic device that would be able to emulate not only brain functions but as well repeat capability of neural physical growth. Throughout this work, we discovered that by means of AC-bipolar electropolymerization, one can generate PEDOT:PSS fibers in an arborous form replicating neuron's morphogenesis. Moreover, by tuning parameters of the applied waveform (amplitude, frequency, voltage offset, and duty cycle) a large diversity of polymer dendrites with various morphologies can be generated. It was found out that through parameter variation, one can control the number of branches, surface (projected area), volume of dendritic structures and even asymmetry of the growth between two wires. Through waveform parameter modification, one also can affect the electropolymerization dynamics. Moreover, by changing the polarization duration through the duty cycle, the engulfing effect of one dendrite's part (from one wire) by another (from a contrary wire) has been observed.

We have shown that the formation of such devices is possible in an aqueous environment, which simplifies the setup and protocol of dendrite generation in general since water is a non-toxic, available universal solvent. Moreover, since dendrites were produced on free-standing wires, any interaction of monomer and electrolyte with the substrate is excluded. It also eliminates the uncertainty of whether dendrite growth occurs on the substrate or outside of the substrate in the electrolyte bulk. Hence, the case shown here can be considered the most generic one and can serve as a reference point for future exploration, including experiments on a 2D substrate.

During this study, only the effect of waveform parameters on the final dendritic morphology was tested, however different results can be expected in the case of a change in the electrolyte's chemical composition. For instance, a different monomer than EDOT and a different sacrificial reagent can be proposed. Additionally, other solvents can be used, such as an organic solvent, an ionic liquid, or a gel media that can be especially attractive for their application in the sensing of organoids, for instance. In addition, one can adjust the inter-electrodes' distance and change the shape of the electrode or its material.

Next, we discovered that various dendritic PEDOT:PSS forms are conductive and differ in terms of conductance values (synaptic weight) that can be programmed through the parameters of AC-bipolar electropolymerization. All dendritic structures were capable of acting as OECTs in both depletion and accumulation modes, implying the possibility of tuning dendritic channel conductivity under gate bias. This feature was used to mimic synaptic functions: STP (therefore emulating homosynaptic plasticity) and LTP with the Ag/AgCl wire and dendritic gates (emulating heterosynaptic plasticity, considering gates as astrocyte cells capable of guiding neural connections). It was found that with various dendritic morphologies, different STP responses can be produced. Moreover, it was observed that by changing the initial parameters of electropolymerization, it is possible to control dendritic objects' conductivity. High *f* dendrites exhibited higher conductivity, while low *f* structures exhibited low conductivity, which was due to the different organization and composition of PEDOT:PSS domains in the structure. This was later confirmed by the STP results, where, low *f* structures exhibited unequal levels of conductance modulation pointing at partial level of PEDOT doping with PSS^-.

To better understand how the structure and composition of PEDOT:PSS affect the dendritic OECT characteristics, a material investigation of dendrites can be carried out. As well, since all the experiments here were carried out in the electrolyte with electroactive species (like EDOT, BQ), one can propose to improve the system so it would be possible to remove all the

electroactive species and therefore will be able to change the electrolyte. Thus, one can increase the range of applied gate bias at which the dendritic OECT can function without faradaic processes related to the presence of EDOT, BQ or HQ. Hence, a broad range of conductance modulation, i.e synaptic weight modulation, of dendritic interconnection can be reached. As it was mentioned, dendritic OECT based on other monomers with different sacrificial reagents and type of electrolytes media can be tested.

Apart from synaptic plasticity, PEDOT:PSS dendrites also successfully emulated neural morphogenesis through AC- electropolymerization according to STDP and SRDP. It was shown that dendritic growth can be governed through two Hebbian learning rules where the synaptic weight of the formed interconnection will obey either spiking time difference (mimicked through effective voltage overlap) or spiking rate between pre- and post-neurons (emulated through various $f_i x f_j$ as signals' combination applied from both wires). The obtained results correlated with Hebb's rules, according to which synaptic weight of a dendritic interconnection increases with an increase in activity correlation between pre- and post- neurons. We disclosed that, depending on the correlation activity during examination of both rules, one could generate a wide range of dendritic morphologies with their individual conductance values (synaptic weights) and growth dynamics. It was also shown that one could obtain dendritic propagation at different interelectrode distances up to 540 μm, which as well resulted in modification of polymer fibers' shape, conductance, and growth dynamics.

Since the human brain is capable of learning processes, next associative memory example (Pavlov's dog experiment) was demonstrated by means of dendritic growth based on spike- timing-dependent plasticity. As a result of the training process, the CS (the conditioned stimulus, bell) triggered UR (unconditioned response, salivation of dog), which manifested as dendritic formation between "bell" and "saliva" correlated nodes.

On top of it, classification tasks were implemented based on the competition between variable firing rates of output signals. One classification approach was presented through different correlation activities between input and output signals based on Poisson distributed spikes. As a result, dendritic growth appeared at different speeds, therefore, performing a classification task. Another classification approach was addressed through unconventional encoding based on the perturbation effect of low-voltage input spikes with non-similar firing rates on a high-voltage output signal. Since low voltage spikes are similar to recorded cellular activity, this approach is promising for its differentiation application in neurosensing.

Consequently, with such bottom-up matured and programmable dendrites, finding the right topology for computing can be simplified. Additionally, by being able to induce structural plasticity according to Hebbian learning rules and to emulate processes such as learning or classification through dendrites' growth, one can develop an evolving neural network in which programming and links building between different nodes can take place simultaneously. In such self-assembled functional circuits, a compromise between appropriate performance and resources utilization can be reached.

As perspectives, structural plasticity governed by Hebbian learning rules can be introduced on a 2D substrate. Dendritic development on the basis of spike-timing activity can be tested with other types of pulses. For example, in triangular-shaped pulses, not only the duration of overpotentiation but also the voltage of the resulting signal can be tuned, resulting in different dendritic maturation and properties. More complex classification tasks with more nodes can be implemented. As well, for development of more advanced network a concept of bipolar electrodes (not connected to the voltage source) can be employed (on free-standing wires or on

2D substrate). Furthermore, one as well can develop polymer dendrites on 3D substrates (in a cube or spherical form, for example) with multiple fixed electrodes.
Several perspectives mentioned here were tested and described in the Appendix.

Appendix

Method and materials

Chapter 2

Materials and instrumentation.

Dendrites formation was implemented via bipolar alternating current (AC) electropolymerization technique in an aqueous electrolyte containing 1 mM of poly(sodium- 4- styrene sulfonate) (NaPSS), 10 mM of 3,4-ethylenedioxythiophene (EDOT) and 10 mM of 1,4- benzoquinone (BQ). All chemicals were purchased from Sigma Aldrich and used without any prior modification. Two 25 μm-diameter gold wires (purchased from GoodFellow, Cambridge, UK) were employed as working and grounded electrodes. Gold (Au) wires were attached to probes and immersed into 20μl volume drop of the electrolyte. The drop of electrolyte was placed onto a Parylene C-covered glass substrate. To keep this study as systematic as possible the wires were lifted up at one height from the substrate surface and wire ends were placed at a distance of L = 240 μm from each other. Square-wave signals were generated from a 50MS/s Dual-Channel Arbitrary Waveform Generator (Tabor Electronics), with a consistent study of electrical parameters' impact: peak amplitude voltage (V_p), frequency (f), duty cycle (dc) and offset voltage (V_{off}). Each dendrite growth was conducted with unused gold wires and daily prepared solutions.

Image processing

Growths were recorded with a VGA CCD color Camera (HITACHI Kokusai Electric Inc). Video preprocessing involves greyscale-256 at 1 fps data conversion (with the VirtualDub open-access software), prior single-frame image processing (with the ImageJ open-access software). Each frame during the dendritic growths was linearly transformed with the StackReg and TurboReg ImageJ addons, to compensate the time-dependent optical aberration that occurs over time as a result of the electrolyte drops' changing curvature due to partial evaporation. Furthermore, frames were cropped around the dendrites and binarized black/white with an appropriate user-defined contrast setting for the different videos generated for each growth. Time-lapses were color encoded with the corresponding ImageJ built-in tool to encode the dynamics of the growth on a scale from a dark purple (for the beginning of the growth), to light yellow (for the end of the growth).

Image feature extraction

The image feature extraction was carried out by Dr. A. Kumar. The image parameters were calculated in Python, involving binarization, pixel counting, fractal dimension determination, branch calculation, and volume determination for the different electrical conditions. Dendrite density was obtained based on the pixel counting from the binarized images without resolution reduction of the original video frames sampledovertime. Error bars on graphs are based on the statistics of four different regions along the dendrite from the electrode to center. The extrapolated three-dimensional volume was calculated by assuming projected branches to have cylindrical structures, with the cylindrical diameter being equal to the branch width and the cylindrical height being equal to the branch length. The fractal dimension was obtained by box-counting algorithm by counting number of boxes and it quantifies the rate at which an object's geometrical features develop at increasing resolution. For asymmetry determination,

the image analysis process was individually performed on each dendrite at both ground and signal electrodes to compare their corresponding density, branches and fractal dimension. Inter- dendrite spacing was determined over time considering their extreme points from both sides, and completion time was defined as the spacing becomes zero. The overall discussion on the two-dimensional image analysis for the three-dimensional dendritic growths acknowledges that the method does not extrapolate three-dimensional physical properties, but serves as a systematic technique to reliably quantify two-dimensional features of three-dimensional objects.

Cyclic voltammetry was conducted on a three electrodes setup, with the 25 μm-diameter gold wires as working and counter electrodes, and a macro Ag/AgCl reference electrode. Measurements were performed distinctively for the solutions containing: 1 mM NaPSS, 10 mM BQ and 1 mM NaPSS, 10 mM EDOT, and 1 mM NaPSS. For each experiment, a new pair of gold wires was used.

Electrochemical impedance spectroscopy (EIS) was carried out on two gold wires' systems with a Solartron Analytical (Ametek) impedance analyzer from 1 MHz to 1 Hz. System with two gold wires were characterized by voltage-ramped impedance spectroscopy (V_{DC} from 0 to 1.3 V at 1 mV/s, V_a =20 mV_{rms}) in the same electrochemical conditions as for the dendritic growths: 10 mM BQ,10 mM EDOT and 1 mM NaPSS.

Circuit impedance modeling was performed using an open-source EIS Spectrum Analyzer software. The fitting was implemented on the raw data spectra without digital-filter preprocessing. The RC parameter fitting was manually adjusted at the visual appreciation of the simultaneous comparison of the Nyquist plots, Bode's modulus, and Bode's phase plots.

Chapter 3

Materials and Instrumentation

Dendrites' growth was carried out as it was described in section 1.1 of experimental part for Chapter 2.

Electrical Characterization was performed through Agilent B1500A Semiconductor Device Analyzer coupled with B2201A Switching Matrix.

Statistical Analysis: Conductivity Evaluation

The optical images of various dendrites were considered to be 2D projections of 3D morphology, with the rectangular wire structure in 2D images corresponding to a cylindrical structure in 3D. Because the dendrite width varies across the morphology, the morphology was described as a collection of multiple cylinders, each having a diameter equal to the morphology's local width. Dendrite and nondendrite pixels were assigned conductance values of 1 and 0. The image representation was then transformed into a network representation, with each pixel of the image corresponding to the individual network node. The theoretical resistance of the resultant network was computed with unit of 1/resistivity. The value of resistivity was calculated based on the ratio of experimental and theoretical resistance values.

Data processing was implemented with Origin program. I_D–V_G curves were plotted taking into account gate current I_G. Source–drain potential was neglected and gate current was considered splitting equally in between source and drain. So, the total current was calculated as the summation of drain current and 50% of gate current.

The same protocol was applied to gate voltage pulses treatment with subsequent extraction of transient current.

Transconductance graphs were obtained by smoothing I_D–V_G curves with Savitzky-Golay filter and further applying first order of derivative. Exact transconductance values shown in **Figure 8** were substracted at V_G = 0 V.

Time constant values were extracted from responses of dendritic OECTs to gate pulses (applied from -0.4 to 0.4 V) by utilizing nonlinear fitting of charging and discharging regions with single exponential decay function and normalization of obtained numbers.

Growth of Third Dendrite

Preliminary in between two wires a structure of dendrites at 10 V_{pp}, 80 Hz, 50% duty cycle and 0 V offset was formed. After their interconnection, a third Au wire was immersed into the system, lifted up at the same height, and placed at 240 μm distance from a place of dendrites completion. Similar aforementioned signal was applied from the third Au wire electrode while one of the connected electrodes was grounded and another one left floating. For signal generation, 50 MS s^{-1} Dual-Channel Arbitrary Waveform Generator (Tabor Electronics) was employed.

Chapter 4

Signals for STDP implementation were designed as bipolar pulses, in which duration of upper and bottom parts of a pulse was 2.5 ms for each. For designing different frequency only time between pulses were varied while the duration of pulses was kept unchanged.

Signals for SRDP implementation were generated by Dr. Ankush Kumar in Python and based on Poisson rate distribution.

Signals were generated in Waveform Generator/Fast Measurement Units (WGFMU), which were attached to Agilent B1500A Semiconductor Device Analyzer coupled with B2201A Switching Matrix.

All the electrical characterizations were performed through as well Agilent B1500A Semiconductor Device Analyzer coupled with B2201A Switching Matrix.

SEM images were obtained using an electron microscope ULTRA 55 (Zeiss) equipped with two detectors for secondary electrons (InLens and Everhart Thornley), a low voltage/high voltage BSE detector and EDX analysis system.

Perspectives

Perspective: Electrolyte engineering. Replacement of sacrificial reagent.
As it was mentioned, BQ is sensitive to light and temperature exposure. Thus, in order to avoid its degradation, there is a constant need to prepare a new BQ solution. As an alternative to a more stable sacrificial reagent, one can propose sodium anthraquinone-2-sulfonate (AQ2S). As an attempt, I conducted the same type of experiment that was described in Chapter 1 but with AQ2S instead of BQ. The EDOT to AQ2S ratio was as well maintained equimolar in this attempt, and the distance between electrodes was set as 240 μm. As well, one Au wire was grounded while a bipolar pulsed waveform was applied from another one (f = 80 Hz, V_p = 5 V, V_{off} = 0 V, dc = 50%). Nevertheless, under these conditions, to observe the dendritic growth, the distance had to be adjusted. In one month, dendritic growth at the same conditions was repeated with the same AQ2S solution. The distance and V_p had to be adjusted this time. Furthermore, this connection obtained with one moth old AQ2S turned out to be conductive. This experiment demonstrated that AQ2S can be stable over time and may serve as an alternative to the BQ. Moreover, this experiment showed the possibility of using various sacrificial reagents for dendritic formation.

a)

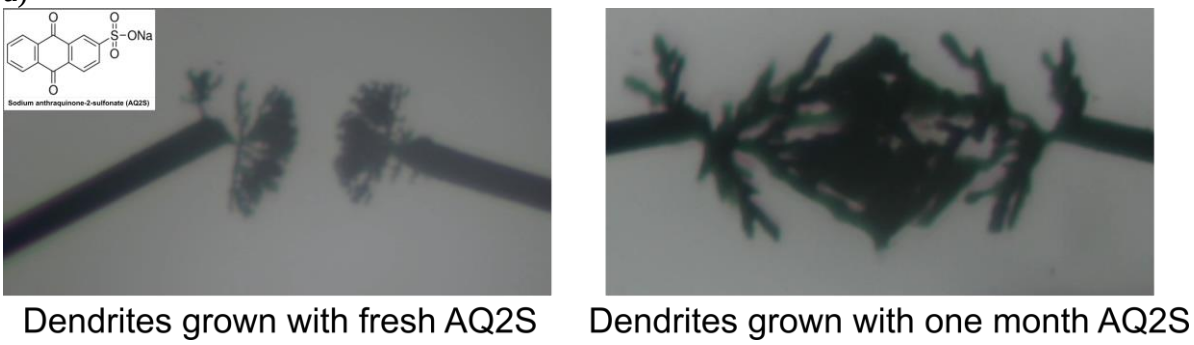

b)

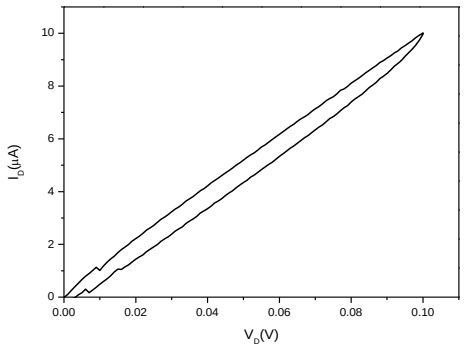

Figure A1. a) Dendritic growth with fresh AQ2S (on the left) and one-month-old AQ2S (on the right). b) Resistance measurement (the drain-source current (I_{DS}) as a function of drain source voltage (V_{DS})) of dendrites generated with one-month-old AQ2S.

Gel organoids

Additionally, I tried to utilize Matrigel as the electrolyte. Firstly, the gel was deposited (20 µl) on the substrate with the following addition of EDOT- and BQ-containing solutions. As a second attempt, a mix of Matrigel with EDOT and BQ solutions was prepared and deposited on a substrate. In both cases, no electropolymerization has been observed since the solidification of Matrigel happened too quickly at room temperature.

Figure A2. a) Experimental setup for generating polymer dendrites in Matrigel media. b) Microscopic image of Au wire inside the electrolyte media containing Matrigel.

Implementation of the bipolar electrode (BPE) concept on free-standing wires

As BPE in our system, one may propose to use a floating wire that is not connected to any voltage source. The bipolar pulses utilized in Section 2.2 of Chapter 4 were reused in this experiment. Bipolar pulses from one wire were applied with amplitude V^+/V^- = 5 V/-5V and with amplitude V^-/V^+ = -5 V/5 V from another wire. A floating wire was placed in the middle between signal's wires and placed at a distance of 240 µm from each of them. All wires were lifted up to the same height.

Firstly, dendrites from one signal wire connected with a floating one. When dendrites from the second wire approached the floating wire, a small outgrowth appeared from it. Further, all three wires were fully connected. As a result, non-active Au wires can be introduced into the dendritic connection. Such a possibility to utilize BPE would allow the building of a more complex network of dendrites and thus introduce a new way of computing or processing data.

Figure A3. Time-lapse of dendritic growth, where a floating wire (not connected to any voltage source) is involved in the formation of the final dendritic junction.

Publications & Oral communications

Publucations:

- Janzakova, K.; Kumar, A.; Ghazal, M.; Susloparova, A.; Coffinier, Y.; Alibart, F.; Pecqueur, S. Analog Programing of Conducting-Polymer Dendritic Interconnections and Control of Their Morphology. *Nat. Commun.* **2021**, *12* (1), 6898. https://doi.org/10.1038/s41467-021-27274-9 .

https://www.nature.com/articles/s41467-021-27274-9

- Janzakova, K.; Ghazal, M.; Kumar, A.; Coffinier, Y.; Pecqueur, S.; Alibart, F. Dendritic Organic Electrochemical Transistors Grown by Electropolymerization for 3D Neuromorphic Engineering. *Adv. Sci.* **2021**, *8* (24), 2102973. https://doi.org/10.1002/advs.202102973.

https://onlinelibrary.wiley.com/doi/full/10.1002/advs.202102973

- Janzakova K., Balafrej I., Kumar A., Garg N., Rouat J., Drouin D., Coffinier Y., Pecqueur S., Alibart F. Structural Plasticity for Neuromorphic Networks with Electropolymerized Dendritic PEDOT Connections. (in progress)

- Kumar, A.; Janzakova, K.; Coffinier, Y.; Pecqueur, S.; Alibart, F. Theoretical Modeling of Dendrite Growth from Conductive Wire Electro-Polymerization. *Sci. Rep.* **2022**, *12* (1), 6395. https://doi.org/10.1038/s41598-022-10082-6.

https://www.nature.com/articles/s41598-022-10082-6

- Scholaert, C.; Janzakova, K.; Coffinier, Y.; Alibart, F.; Pecqueur, S. Plasticity of Conducting Polymer Dendrites to Bursts of Voltage Spikes in Phosphate Buffered Saline. *Neuromorphic Comput. Eng.* **2022**, *2* (4), 044010. https://doi.org/10.1088/2634-4386/ac9b85

https://iopscience.iop.org/article/10.1088/2634-4386/ac9b85/meta

Oral communications:

- "*Electrochemical structuring of organic conducting polymers for its implementation and development as neuromorphic devices*"

Janzakova Kamila, Ghazal Mahdi, Kumar Ankush, Coffinier Yannick, Pecqueur Sébastien, Alibart Fabien.

2nd Workshop on Neuromorphic Organic Devices, Chania , Greece (2022).

- "*Development of 3D organic polymer dendrites as neuromorphic device*"

Janzakova Kamila, Ghazal Mahdi, Kumar Ankush, Coffinier Yannick, Pecqueur Sébastien, Alibart Fabien.

Nanotexnology conference, International symposium on Flexible Organic Electronics (ISFOE), Thessaloniki, Greece (2022).

- "*Electrochemical structuring of organic conducting polymers for its implementation and development as neuromorphic devices*"

  Janzakova Kamila, Ghazal Mahdi, Kumar Ankush, Coffinier Yannick, Pecqueur Sébastien, Alibart Fabien.

  GDR BioComp PhD Forum, Grenoble (virtual), France (2021).

- "*Organic Electrochemical Transistors Based on Electropolymerized Dendritic Structures*"

  Janzakova Kamila, Ghazal Mahdi, Kumar Ankush, Coffinier Yannick, Pecqueur Sébastien, Alibart Fabien.

  European Materials Research Society (MRS) Fall Meeting (virtual) (2020).